UNIVERSITY OF OSLO
Institute of Theoretical Astrophysics

Dynamic Loops in a Solar Active Region

Cand. Scientarum Thesis

Geir Emblemsvåg

5th February 2007

Contents

Acknowledgments

I wish to open this thesis with thanks to those who contributed invaluable assistance: my supervisor Viggo Hansteen for much–needed advise on scientific writing and great patience, Bart de Pontieu for his help and advise on data reductions and Marte Skogvoll for her corrections and suggestions.

I also want to thank my family and friends for their support during the project time — it is appreciated!

This document was typeset in LaTeX, with images produced in IDL. All data presented is either in the public domain or used with express permission.

Chapter 1

Introduction

Historical Development

Ever since the solar corona was deduced by Edlén (1943) to be of order $\sim 10^6$K hotter than allowed by heat transfer from the lower–lying strata, it has been a driving objective of physicists to describe the physical process at the heart of this "heating problem".

Several mechanisms have been proposed, of which the one currently deemed the most fruitful employs stress–induced reconnection of magnetic field lines in the highly structured atmosphere, the stress built up through movement of the flux lines towards and in the intergranular lanes (eg. Parker 1983).

Regardless of its physical nature, a functional parametrization of the heating mechanism can be derived to fit various observations. This has led to three broad categories of heating models; uniform heating per the RTV model of Rosner et al. (1978), the footpoint–focused models like Serio et al. (1981)'s refinement of RTV, here referred to as the SRTV model, and those that are apex–focused (eg. Priest et al. 2000).

While the models have primarily been derived for coronal loops in the hydrostatic case, they have found utility also in the description of transient events, such as the sporadic release of energy described by the stress–induced reconnection. Predictions made by these models have been tested through time–dependend numerical analysis (eg. Reale et al. 2000a and 2000b, Warren et al. 2003, Spadaro and Lanza 2003).

Current Focus

The concern of the present study is a 15 minute duration transient loop brightening captured by the TRACE EUV imager (Handy et al. 1999) and the SUMER spectrograph (Wilhelm et al. 1995) during a two–hour observation of the active region 8558, on June 4 1999.

The high cadence data from these two sources was analysed using a tunable genetic algorithm (Charbonneau 1995) and line moments. The results were then used together with the spatial information from the image data to design numerical experiments for the coronal loop advection engine TTRANZ (Hansteen 1991). This was done with the intention of discovering what, if any, parameters of the chosen heating model that can reproduce similar emission traits as seen in the telescope data. The computational results are not formally fitted to the data, but correlations in intensity trends are attempted mapped to physical plasma mechanisms observed in the numerical analysis.

The actual comparison is made with synthetic column–integrated spectra convolved with instrument response functions so as to mimic the peculiarities of the telescopes, and thus minimize the instrument bias.

Because any analysis is only as good as its input data, considerable time is also dedicated to a survey of the best known parametrizations and coefficients for calculation of atomic ionization and excitation processes, as well as element abundances and radiative energy loss rates. This assessment uses the CHIANTI (Landi et al. 2006, Dere et al. 1997) spectral diagnostic library and the NIST (Ralchenko et al. 2005) line database as starting points.

Thesis Layout

The thesis is built up from three parts: The first one is a brief introductory chapter intended to describe and define the variables and equations used in later chapters. A middle part of two chapters describe the SUMER and TRACE observations. The final chapters are devoted to the numerical analysis engine and the simulation results.

Chapter 2

Line and Plasma Fundamentals

This chapter introduces the physical processes shaping plasmas described by the coronal equilibrium, a low density approximation applicable to the transition region and corona. My primary intention is to define the parameters and equations used in later chapters in a systematic fashion, as a convenience to the reader. Therefore no results will be presented here.

I first cover the microscopical aspect of ionization and excitation balances, which are important factors in the second topic, the emission spectrum and diagnostics of it. Finally the macroscopic view of the plasma is covered in a section about the plasma governing equations relevant in the low β corona.

The methods defined here will be used in later chapters to interpret observational data and to set up proper numerical analysis schemes.

2.1 The Coronal Equilibrium Model

Electron densities in coronal plasmas are on the order of 10^{16} m^{-3} or less, the coronal temperature is of order $\sim$ 1MK while the radiation temperature is 5770K (0.5 eV). This is far from thermodynamic equilibria (TE), and because of the paucity of collisions potentially far even from the *local* thermodynamic equilibria (LTE) we are used to. This is important because several of the processes we usually require to explain the distributions of ionizations states and excited levels do no longer apply in such hot, low–density, plasmas. This plasma regime is referred to as the coronal equilibrium (CE). It allows for numerous simplifying approximations to the standard plasma–describing equations.

When the density is low and the temperature is high, the plasma is optically thin — practically all the photons emitted from the metals[1] will leave the cloud unhindered, and not participate in ionization or excitation processes, which means that ionization and excitation will be dominated by collisions with charged particles. On the other hand, radiative relaxation

---

[1] In the lower corona H and He are fully ionized, and the bremsstrahlung is weak.

rates are so much higher than the combined excitation rates that we can assume that every excited ion will have time to relax before any secondary excitations, so that the entire population will be in the ground (or a metastable) state.

Because the emitted energy leaves the plasma cloud entirely, there is a net loss of energy from the system. The CE therefore is not exactly an equilibrium state, it must be kept in a steady state by a heat source external to the system. The physical nature of this source is not treated in this thesis, but a parametrization of it is discussed in the last section of this chapter.

2.2 Atomic Interaction Processes

2.2.1 Excitation and Relaxation Processes

Electron Impact

In the low density coronal plasma, practically all excitations are caused by collisions between ions and electrons. There is a small chance that an electron upon impact will transfer some of its kinetic energy to a bound electron in the ion, and force it into a higher orbit. The energy then lost by the impactor is the difference in binding energies between the upper land lower states,

$$\Delta E_K = E_u - E_\ell = \Delta E_{u,\ell}. \tag{2.1}$$

The chance of this happening per ion in unit time is the inverse of the effective cross section $\sigma_{\ell,u}$ of the ion weighed by its *per electron* probable velocity v,

$$\langle \sigma_{\ell,u} v \rangle,$$

times the numerical density of electrons n_e:

$$P(\text{excitation}) \quad = \quad 1 - (n_\mathrm{e} \, \langle \sigma_{\ell,u} v \rangle)^{-1}. \tag{2.2}$$

Thus the mean number of excitations per volume per second is

$$n_\mathrm{e} \, N(X_i) \, C^{\mathrm{ex}}_{\ell,u}, \tag{2.3}$$

with the common symbol $C^{\mathrm{ex}}_{\ell,u}$, known as the rate coefficient, replacing $\langle \sigma_{\ell,u} v \rangle$, and where $N(X_i)$ is the number density of ionization stage i of atomic species X. The cross section is a function involving all the orbiting electrons, precluding a closed–form function for it, but very good parametrizations have been devised. Unfortunately they are all very computationally expensive, so in practical applications it is customary to use another parameter, known as the thermally averaged collisional cross sections $\Upsilon_{\ell,u}$, which are functions of the electron temperature and transition. From this $\Upsilon_{\ell,u}$ a simple parametrization follows,

$$C^{\mathrm{ex}}_{\ell,u} \quad = \quad 2\sqrt{\pi} a_0 \hbar m_e^{-1} \left(\frac{I_\infty}{k_B} \right)^{1/2} T_e^{-1/2} \, \frac{\Upsilon_{\ell,u}}{\omega_\ell} \, \mathrm{e}^{-\frac{\Delta E_{\ell,u}}{k_B T_e}}, \tag{2.4}$$

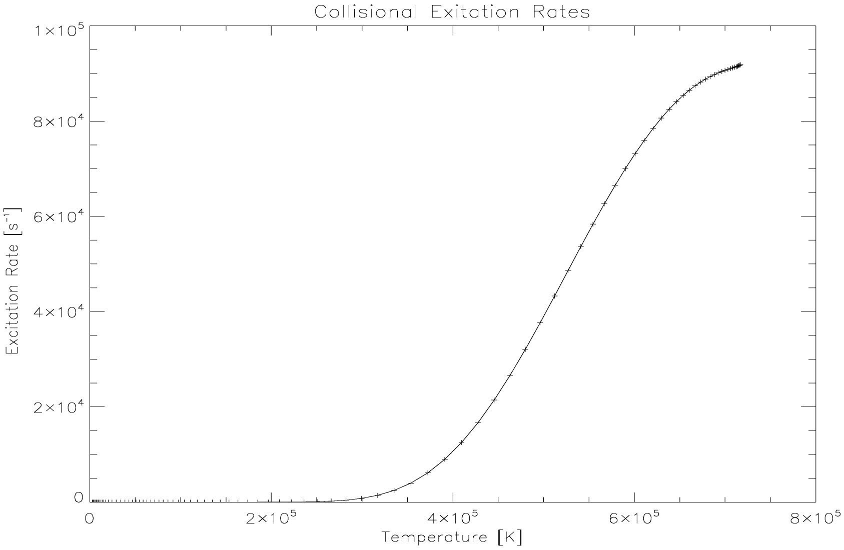

Figure 2.2.1: Rates of collisional excitation of Fe IX from the ground state to $3p^5 3d^1\,{}^1P^o_1$.

where the constant term has a numerical value of $8.63 \times 10^{-12} \mathrm{m}^3 \mathrm{s}^{-1} \mathrm{K}^{1/2}$.

The rate coefficient grows quite rapidly with temperature up to the point where $k_B T \approx \Delta E$, after which it varies very slowly with temperature, a trend demonstrated in figure 2.2.1. As the temperature grows beyond the binding of the impacted electron, this process will begin to cause ionizations rather than excitations.

Collisional excitation, as do all of the interaction processes, has an inverse called collisional relaxation, in which the impactor receives the excess energy of an electron in an upper level, allowing it to relax back to the ground state without emitting a photon. The rate coefficients are related through detailed balance,

$$\frac{C^{\mathrm{de}}_{u,\ell}}{C^{\mathrm{ex}}_{\ell,u}} = \frac{\omega_\ell}{\omega_u} \exp\left(-\frac{\Delta E_{u,\ell}}{k_B T_e}\right), \tag{2.5}$$

where ω_i is the statistical weights of level i. In most cases, the inverse process can be ignored in a CE plasma, with the exceptions being excited states without *allowed* paths of radiative relaxation. "Allowed" refers to electric dipole transitions, the other possibilities being electric multipole, magnetic transitions and intercombinations. All of these have significantly lower rate coefficients than the allowed transitions.

Radiative Rates

Resonant photoabsorption is another excitation process, where the necessary energy comes from photons. Since the source of the major component of the radiation field in the corona is the $\sim$ 6000K (0.5eV) photosphere, very few photons have sufficient energy to invoke the $\Delta E \gtrsim$ 50eV excitations necessary to produce coronal emission lines. But its inverse, radiative relaxation, is the dominant relaxation process in the corona.

The Einstein rate coefficient $A_{u,\ell}$ for radiative relaxation is calculated from quantum–mechanical principles, which seek to determine a value known as the line strength $S_{u,\ell}$, from which another quantity $f_{u,\ell}$, called the oscillator strength, is calculated (the reason for this somewhat convoluted approach is that in many applications $f_{u,\ell}$ is a more practical quantity than the rate coefficient). Their relations are

$$f_{u,\ell} = \frac{2}{3}\frac{mc^2}{e^2(\hbar c)^2}\,\Delta E_{u,\ell}\,\frac{S_{u,\ell}}{\omega_u}. \tag{2.6}$$

Defined through the oscillator strength, the rate coefficient is

$$A_{u,\ell} = \frac{2ce^2}{(\hbar c)^2 mc^2}\,(\Delta E_{u,\ell})^2\, f_{u,\ell}. \tag{2.7}$$

An electric dipole (allowed) transition will have a rate coefficient on the order of $10^{10}\mathrm{s}^{-1}$, many orders of magnitude greater than the excitation rate $n_\mathrm{e}C^\mathrm{ex}_{\ell,u}$. This means that all excited electrons with an allowed transition to a lower level will immediately decay with the spontaneous emission of a photon, rather than being collisionally relaxed or excited to an even higher level.

Figure 2.2.1 exemplifies how the high relaxation rate keeps the levels above the ground state unpopulated. The graph plotted is the excitation rate for the Fe IX λ171 transition with $A_{u,\ell} = 2.09 \times 10^{11}\ \mathrm{s}^{-1}$. The excitation rate coefficient plateaus towards a constant of about 10^5 as the temperature reaches the energy of the transition (73eV), a mere 5×10^{-6} of the relaxation rate. This ensures that the upper level is kept virtually empty.

Magnetic and electric multipole transitions can have sufficiently low rates for the two other paths out of the excitation level to play a minor role. This is a relatively rare condition in emission spectra, but one that opens up for the diagnostic tool of line ratio analysis.

2.2.2 Ionization and Recombination Processes

The ionization fraction of an atom in this plasma regime is determined mostly by collisional ionization and radiative recombination, but around the temperatures of maximum formation dielectric recombination also plays a large role. Minor adjustments from exitation–autoionization are necessary, while the remaining two processes, photoionization and three–body recombinations are negligible, due to the low radiation field intensity and low density, respectively.

Collisional Ionization

Collisional ionization is the continuation of collisional excitation beyond the ionization energy of the impacted ion. This makes the collisional ionization (also known as electron impact) process the most important one in a coronal plasma.

Like in the excitation case, the rate coefficient is based on the cross section and plasma temperature, and quite good parametrizations exist, cf. eg. Shull and van Steenberg (1982). Mihalas (1978) presents analytical approximations both for LTE and dynamic plasma states.

With the rate coefficient I_i^{col}, the rate of ionizations is

$$I_i^{\mathrm{col}}\, N(X_i)\, n_{\mathrm{e}}. \tag{2.8}$$

Excitation–Autoionization

The autoionization process involves two electrons, both excited so that their net excitation energy exceeds the energy required to ionize one of them. If this electron then absorb the other's excess energy, it becomes unbound.

Because a coronal plasma has most of its atoms in the ground state, this is not a process that occurs very frequently, especially not during equilibrium.

I denote the rate coefficient from stage i to $i+1$ by the symbol I_i^{ea}.

Radiative Recombination

This is a process in which an electron is captured by an atom, which then emits a photon. The analytic rate coefficient, as cited by Salzman (1998), is

$$R_i^{\mathrm{rad}} \quad = \quad 1.92\times 10^{-19}\, n_p \sqrt{|E_{i,n_p}|}\, y^{3/2}\, E_1(y) \qquad \mathrm{m^3 s^{-1}}. \tag{2.9}$$

Here n_p is the principal quantum number of the electron after capture, E_{i,n_p} the ionization energy of that state, $y = |E_{i,n_p}|/T_e$ and $E(y)$ is the exponential integral.

Radiative recombinations happen at a rate

$$R_i^{\mathrm{rad}} N(X_i).$$

Dielectronic Recombination

The dielectronic recombination is the inverse process of excitation–autoionization. Unfortunately there are no simple analytic formula for its rate coefficient $R_i^{(2\mathrm{e})}$, but Salzman cites some numerical methods, like Burgess and Tully (1992).

Even though this rate is dependent on the density of electrons, and thus intuitively of little importance in coronal plasma, he makes the case that it is actually relevant, and can even be dominant, near the temperatures of maximum formation for the ions. The somewhat counter–intuitive physics behind this is described by Reisenfeld et al. (1992).

2.2.3 Ionization Balance

The fraction of atoms kept in each ionization stage, the ionization balance, is given by the sum of ionizations, recombinations and flux through the region:

$$\frac{\partial N(X_i)}{\partial t} + \nabla \cdot [\mathbf{u} N(X_i)]$$
$$= n_\mathrm{e}[N(X_{i-1})I_{i-1} - N(X_i)(I_i + R_i) + N(X_{i+1})R_{i+1}], \qquad (2.10)$$

a continuity equation for the ions, but one with sinks and sources.

$$I_i \approx I_i^{\mathrm{col}} + I_i^{\mathrm{ea}} \qquad (2.11)$$

is the total ionization rate from ionization stage i, and

$$R_i \approx R_i^{\mathrm{rad}} + n_\mathrm{e} R_i^{(2\mathrm{e})} \qquad (2.12)$$

the recombination rate from that stage.

2.3 The Spectrum

In the coronal equilibrium model the line spectrum is a simple function of the numerical density of the emitting ion. The low density makes the optical depths of the lines negligible. This allows us to ignore extinction and scattering effects, in turn making the equations of transfer trivial.

2.3.1 Emission Intensity

Contribution Function

The strength of the line created by transitions from upper level u down to level ℓ in a unit volume defines the *contribution function*

$$G_{u,\ell}(T_e) = \left(\frac{hc}{\lambda}\right)\left(\frac{N(X^{+m})}{N(X)}\right)\left(\frac{N(X)}{n_\mathrm{H}}\right) n_\mathrm{H}\, n_\mathrm{e}\, C_{g,u}^{\mathrm{ex}}\, B_{u,\ell}. \qquad (2.13)$$

The first ratio is the energy of a photon with wavelength λ. The following two are the number density of emitting ions, on its common form using the ionization equilibrium, and the atomic abundance relative to hydrogen, multiplied with the hydrogen density to get the density of the atomic species:

$$\left(\frac{N(X^{+m})}{N(X)}\right)\left(\frac{N(X)}{n_{\mathrm{H}}}\right)n_{\mathrm{H}}. \tag{2.14}$$

The ionization is dependent on temperature and density, but the abundance is usually considered constant for a coronal plasma.

The average number of ions available in the upper level u is now found by factoring in the transition rate

$$n_{\mathrm{e}}\, C^{\mathrm{ex}}_{g,u} \qquad [\mathrm{s}^{-1}] \tag{2.15}$$

from the ground state and up to u. In CE it is usually safe to say that all the ions in level u are populated from the ground state g.

The excited electron often has several alternative lower levels which it can decay into, requiring us to apply a correction known as the *branching fraction* $B_{u,\ell}$, the fraction of the ions in level u that decays with the desired wavelength. Its definition is

$$B_{u,\ell} \quad = \quad \frac{A_{u,\ell}}{\sum_{k<u} A_{u,k}}, \tag{2.16}$$

where the $A_{u,k}$ are the Einstein coefficients of each of the possible transitions.

I wrote "usually safe", which implies that there are other possibilities: When the density is "just right", some levels with low radiative relaxation rates can be excited further up, or even collisionally relaxed, at significant rates. In the cases where we are able to quantify "just right", the lines can be used as excellent probes into the density of the emitting plasma.

A different case occurs when the upper level is populated at significant rates from higher levels, as part of a cascade. Usually the excitation rates from the ground state do dwarf this relaxation from higher states, but that cannot be taken for granted.

Intensity

The intensity I_λ of a spectral line from an optically thin plasma is then found by integrating through the column,

$$I_{u,\ell} \quad = \quad \frac{1}{4\pi}\int G_{u,\ell}(T_e)\;\mathrm{d}z. \tag{2.17}$$

The factor 4π is added because we assume that the radiation is isotropic.

2.3.2 Line Profile

Their name nothwithstanding, emission lines do not really appear as infinitely thin columns in the spectrum. They are actually smeared out, according to a *line function* $L(\lambda)$, which is defined and positive for all $\lambda > 0$ and integrates to 1. The emission rate in the interval $(\lambda, \lambda + \mathrm{d}\lambda)$ around an arbitrary wavelength λ is therefore given by

$$I_{u,\ell}(\lambda)\,\mathrm{d}\lambda \quad = \quad I_{u,\ell}L(\lambda)\,\mathrm{d}\lambda. \tag{2.18}$$

The form of $L(\lambda)$ depends on the plasma model, for a small volume of coronal plasma it is exclusively determined by Doppler shift of the emitted radiation, but not in a simple manner. The different layers of the column we integrate the intensity through will contribute different intensities, shifts and widths, making the column–integrated line profile quite complex.

Doppler Shift

The Doppler shift affects the emitted spectrum of a plasma volume in two ways: through broadening of the lines, and by shifting them away from their theoretical central wavelengths.

A line emitted from a source moving relative to us will be observed with a shift in wavelength dependent on its velocity. Quantitatively, for a point source moving with velocity $u_\phi = u\cos(\phi)$, in the direction ϕ ($\phi = 0$ is directly away from us), this effect has a magnitude

$$\frac{\lambda_\mathrm{o}}{\lambda_\mathrm{e}} \quad = \quad \left(\frac{1 + (u_\phi/c)}{\sqrt{1 - (u_\phi/c)^2}}\right), \tag{2.19}$$

where λ_o is the observed wavelength, and the emitted wavelength is

$$\lambda_\mathrm{e} \quad = \quad \frac{hc}{E_{u,\ell}}. \tag{2.20}$$

A common approximation, valid in the non–relativistic limit, is

$$\frac{\lambda_\mathrm{o}}{\lambda_\mathrm{e}} \quad = \quad \left(1 + \frac{u}{c}\right), \tag{2.21}$$

where we for simplicity drop the directional dependence too.

The bulk motion of the plasma volume will thus shift the emitted radiation by the fraction given in equation 2.21.

Each single ionic population follows a Maxwellian velocity distribution[2], and therefore the doppler shifts from each ion will also follow a Gaussian distribution:

$$I_{u,\ell}L(\lambda) \quad = \quad \frac{1}{\sqrt{2\pi\sigma}}\exp\left(-\frac{(\lambda - \lambda_\mathrm{e})^2}{2\sigma^2}\right), \tag{2.22}$$

---

[2] The soundness of this claim is discussed in appendix A.

The variance of this function depends on the temperature;

$$\sigma^2 = \frac{\lambda^2}{2c^2}\left(\frac{2k_BT_e}{M_i} + (\delta u)^2\right). \tag{2.23}$$

Here M_i is the ion mass, and $(\delta u)^2$ is the variance in the bulk plasma velocity (the presence of δu in the variance means that a relatively cold turbulent plasma will look like a laminar plasma with just a much higher temperature).

The common measure of line width is the "Full Width at Half Maximum" (FWHM), defined as the difference in wavelength between the two points at which the line is at half its maximum intensity. It is linear in the standard deviation,

$$\text{FWHM} = 2\sqrt{2\log 2}\sigma, \tag{2.24}$$

eg. about 17mÅ for an O VI λ173 line at $T_e = 3 \times 10^5$K.

2.3.3 Line Moment Analysis

The line profile is defined as a probability density function, and this suggests a practical way of describing the complex column–integrated line profile; by its moments. This a powerful method for interpretation of spectroscopic observations.

Intensity

We start with the zeroth moment of the distribution, which is simply its total:

$$I_{u,\ell} = \int_0^\infty I(\lambda)L(\lambda)\,\mathrm{d}\lambda. \tag{2.25}$$

We need to find this intensity total before we can compute any further moments of the distribution.

In the case of N bins, let λ_i be the wavelength represented by bin $i \in \mathbb{Z}_N$, $I(\lambda_i)$ the intensity measured by that bin. Then equation 2.25 can be discretized as

$$I_{u,\ell} = \sum_{i=1}^{N} I(\lambda_i). \tag{2.26}$$

Line Center Shift

The line center, $\langle\lambda\rangle$, is defined by the first moment of the distribution:

$$\langle\lambda\rangle = \int_0^\infty \lambda\, L(\lambda)\,\mathrm{d}\lambda. \tag{2.27}$$

Any shift in wavelength away from λ_{e} is caused by bulk motion of the plasma, and because the wavelength is connected to the velocity through equation 2.21,

$$\langle u\rangle = \frac{c(\langle\lambda\rangle - \lambda_{\mathrm{e}})}{\lambda_{\mathrm{e}}}, \tag{2.28}$$

this gives us a powerful diagnostic tool, valid regardless of the form of $L(\lambda)$.

Equation 2.27 translates readily into a discrete version we can apply to the binned data from a spectrograph,

$$u(\lambda_i) = \frac{c\,(\lambda_i - \lambda_{\mathrm{e}})}{\lambda_{\mathrm{e}}}. \tag{2.29}$$

Then the expected velocity of the radiating plasma is

$$\langle u\rangle = \frac{\sum_{i=1}^{N} u(\lambda_i)\, I(\lambda_i)}{\sum_{i=1}^{N} I(\lambda_i)}. \tag{2.30}$$

Line Broadening

Similarly, the width σ of the profile is defined by the second moment,

$$\sigma^2 = \int_0^\infty (\langle\lambda\rangle - \lambda)^2 L(\lambda)\,\mathrm{d}\lambda. \tag{2.31}$$

Equation 2.31 is discretized the same way as the line shift moment, eg. as

$$\sigma^2 = I_\lambda^{-1}\Big[\Big(\sum I(\lambda)\Delta\lambda\Big)^2 - \sum I(\lambda)\,(\Delta\lambda)^2\Big]. \tag{2.32}$$

2.4 Plasma Governing Equations

Large scale plasma behaviour is governed by the conservation equations. The continuity, momentum and energy equations, on the form we will later analyze numerically, are defined in this section. In the low–β case the plasma is contained by the magnetic field, with only one dimension in which to move. The equations can therefore be written on scalar form instead of vectorially. The spatial coordinate z is used to measure distance along the loop. The symbols u, ρ and p represent bulk velocity along z, density and static pressure, respectively.

2.4.1 The Conservation Equations

Continuity

This equation states that there are no sources nor sinks for matter,

$$\frac{\partial\rho}{\partial t} + \frac{\partial}{\partial z}(u\rho) = 0. \tag{2.33}$$

An obvious consequence of the continuity equation is that when the velocity of a plasma changes in a section of a flux tube, its local density must change in accord.

Momentum

The momentum equation is Newton's second law for gases. It takes into consideration the viscous pressure and a gravitational potential; a Lorentz force is not included, as it is zero along the field.

$$\frac{\partial}{\partial t}(\rho u) + \frac{1}{2}\frac{\partial}{\partial z}(\rho u^2) \quad = \quad \frac{\partial}{\partial z}(p + Q) - \rho g_{\shortparallel} \tag{2.34}$$

$g_{\shortparallel}$ is the component of gravitational acceleration parallell to the loop, giving the plasma an "effective weight". The viscous pressure, normally a tensor quantity, can be defined as

$$Q \quad = \quad 4/3 \rho l_g^2 \frac{\partial u}{\partial z} \times \min\left(\frac{\partial u}{\partial z},\ 0\right), \tag{2.35}$$

with l_g a chosen constant comparable to a shock width in length. In the numerical analysis the viscosity will ensure that all parameters change in appropriate amounts across the shock front, and that it travels at correct speed.

Energy

The equation of energy advection contains the terms for loop heating and heat dispersal, on which much attention is fixed in this paper. These terms are defined in a separate section below (2.4.4), with a discussion of how the energy distribution in the loop is affected by variations in them.

$$\frac{1}{2}\frac{\partial}{\partial t}[\rho(u^2 + 2\varepsilon)] + \frac{1}{2}\frac{\partial}{\partial z}[u\rho(\frac{1}{2}u^2 + 2\varepsilon)]$$
$$= -(p + Q)\frac{\partial u}{\partial z} - \frac{\partial}{\partial z}(F_c + F_r + F_h). \tag{2.36}$$

The specific internal energy $\varepsilon = C_p T$, where the specific heat C_p is approximately $\frac{10}{3} k_B n_{\mathrm{e}}$ in a fully ionized hydrogen plasma.

The sources and sinks of energy are these three fluxes:

- The conductive flux F_c,
- the coronal heat source F_h and
- the radiative losses F_{r}.

The actual definitions and descriptions of these three terms are deferred to section 2.4.4, below.

2.4.2 Equation of State

We are now one equation short of a consistent system, and an appropriate closure relation is the equation of state for an ideal gas,

$$p = nk_BT_e = \frac{\rho k_B T_e}{\overline{m}}. \tag{2.37}$$

The mean mass $\overline{m}$ is about $0.6m_H$, corresponding to $n \approx 2n_\mathrm{e}$, in a fully ionized hydrogen plasma.

Scale Velocities

Two velocities are important in a plasma: the sound speed

$$u_S = \sqrt{\frac{\gamma p}{\rho}}, \tag{2.38}$$

and the Alvén speed

$$u_A = \sqrt{\frac{p_B}{\rho}}, \tag{2.39}$$

where

$$p_B = \frac{B^2}{2\mu_0}, \tag{2.40}$$

with B the strength of the magnetic field and $\mu_0 = 4\pi \times 10^{-7}$ H/m the permeability of empty space. p_B is thus the tension in the magnetic field, a magnetic analogue to pressure.

2.4.3 Magnetohydrodynamic Considerations

Any thesis discussing plasmas of the solar atmosphere must consider the local magnetic fields. In the case of magnetic flux tubes, like coronal loops, a key facet is the plasma β:

$$\beta \equiv \frac{p}{p_B} \approx \frac{4\mu_0 n_\mathrm{e} k_B T_e}{B^2}. \tag{2.41}$$

High–β plasmas will have their field topology determined by the thermal pressure, as opposed to the low β situation where the magnetic field is king, and the topology will only change when the field does. A typical coronal loop has a magnetic field of 10–100mT, making $\beta \ll 1$ in the low corona. This condition we call a "low–β plasma", it is one in which we can safely restrict our calculations to motions parallell to the magnetic field.

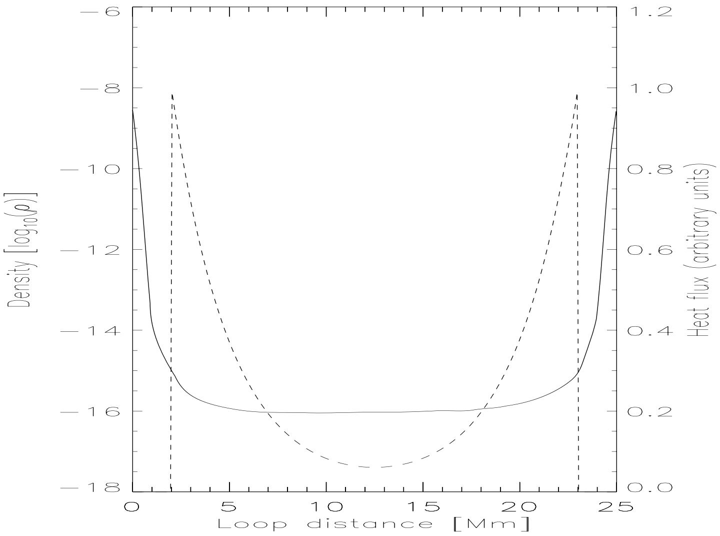

Figure 2.4.1: The gradient of the heating function overplotted with a typical loop density distribution. This particular $Q(h)$ (with arbitrary amplitude) is described by $z_0 = 2\text{Mm}$ and $z_H = 3\text{Mm}$.

2.4.4 Energy Sources and Sinks

The profile and magnitude of the loop temperature depends on the sources and sinks listed in equation 2.36. These can interact with external reservoirs, ie. the chromosphere, corona and space, and supply energy to or remove it from the system.

Thermal Conduction

A conductive flux $F_{\rm c}$, defined as per Spitzer (1962) as

$$F_{\rm c} \quad = \quad -\kappa T^{5/2}\,\frac{{\rm d}T}{{\rm d}z}, \tag{2.42}$$

with $\kappa = 7.8 \times 10^{-10}\text{J/m}^2/\text{K}^{7/2}$. The conductive flux is mainly carried by the electrons, with an efficiency strongly dependent on the temperature. It carries energy from hot to cooler strata, eg. from the hot corona and down to the chromosphere. It is thus an efficient heat sink for the loops, especially at $T \gtrsim 1\text{MK}$.

Radiative Losses

The form of the radiative losses $F_{\rm r}$ varies with plasma temperature in three "stages". In the chromosphere we have neutral hydrogen, and the plasma (although we approximate it as such) is not really optically thin.

In the transition region (TR) and most of the corona we are justified in treating all radiation as thin, and the plasma is too cool for free-free radiation to play a part. This it only does around $T \gtrsim 2-3\times10^6$K. So in the interval 2.5×10^4 – 2×10^6K we use

$$F_\mathrm{r} \;=\; n_e \sum \frac{hc}{\lambda_{u,\ell}}\, n_\ell C^\mathrm{ex}_{\ell,u} + L_\mathrm{rec}. \tag{2.43}$$

L_rec is energy lost in the radiative recombinations, n_ℓ the number of ions in stage ℓ and $C^\mathrm{ex}_{\ell,u}$ is the collisional excitation rate defined in section 2.2.1.

Above $2-3\times10^6$K the free–free loss due to bremsstrahlung is included.

The Heating Function

The heating function F_h is the primary heat source for the extremely hot corona. Although the physical nature[3] of this term is a very interesting subject in itself, we here contend ourselves with a parametrization of it. We call this parametrization of F_h our *heating model*. I divide the heating function into two parts, one responsible for the steady background heating, up to about 10^5K, and one for flare–like events that temporarily heat the loop to coronal temperatures.

The model for background heating consists of a section with exponentially decaying strength above a constant segment. Neither the scale height of the exponential z_H, the length of the constant z_0 nor the amplitude of the heating $F_{h,0}$ need to be the same for each side of the loop. Symbolically the function is

$$F_h(z) \;= F_{h,0}\, m(z_H, z_0) \;\begin{cases} 1 & \text{where} \quad z \le z_0 \\ \mathrm{e}^{-\frac{z-z_0}{z_H}} & \text{where} \quad z > z_0. \end{cases} \tag{2.44}$$

The scaling function $m(z_H, z_0)$ is included to ensure that the total heat input from energy source stays constant when we change the height parameters,

$$m(z_H, z_0) \;=\; \left(1 - \mathrm{e}^{-\frac{L-z_0}{z_H}}\right)^{-1}, \tag{2.45}$$

where L is the full loop length.

The actual energy deposition rate (volumetric heating rate) is the negative divergence of F_h;

$$Q_h(z) \;=\; -\frac{\mathrm{d}F_h}{\mathrm{d}z} \tag{2.46}$$

$$\;=\; \begin{cases} 0 & \text{where} \quad z \le z_0 \\ z_H^{-1} F_h(z) & \text{where} \quad z > z_0. \end{cases} \tag{2.47}$$

---

[3] See eg. Aschwanden (2004) (pp. 355–406).

We see that lowering the constant z_0 will shift the focus of the heating downwards into the TR and affect the loop temperature because of the relation between the specific heat (ie. internal energy), temperature and density of a gas,

$$\begin{aligned} \varepsilon &= C_p T && (2.48) \\ &= \frac{3}{2}\frac{\rho}{m} k_B T. && (2.49) \end{aligned}$$

Both the density in the transition region and our heating function F_h have strong height dependence, as illustrated in figure 2.4.1.

Qualitatively, a given total energy will produce higher temperatures when the heating is focused in the corona, since the supplied energy is shared between very few particles, than in the chromosphere, where on the order of 100 times as many particles are available to absorb the energy.

Common values for z_H are around $15 - 20$Mm, making it much longer will lead to a basically constant heating, as in Rosner et al. (1978)'s model. z_0 should place the heating near the TR, at ~ 1Mm. If both lengths are very short, a lot of energy is focused into a small region, and this should lead to interesting dynamics caused by evaporation of chromospheric plasma into the corona and strong conduction both downwards to the chromosphere and upwards into the corona[4].

Transient Heating

Flare–like[5] heating is modelled as a time-varying gaussian function centered at some height in the coronal part of the loop. It is used for simulation of transient events. Naming the center height $z_0^{\mathrm{flare}}(t)$, the width of heating $z_H^{\mathrm{flare}}(t)$ and its amplitude $F_{h,0}^{\mathrm{flare}}(t)$, the transient heating function can be written as

$$F_h^{\mathrm{flare}}(z,t) = F_{h,0}^{\mathrm{flare}}(t) \mathrm{e}^{\frac{-(z-z_0^{\mathrm{flare}}(t))^2}{z_H^{\mathrm{flare}}(t)^2}}. \qquad (2.50)$$

$F_{h,0}^{\mathrm{flare}}(t)$ will typically be non–zero only for short durations, eg. in response to magnetic reconnections and ohmic dissipation of the current sheet. For the loop studied in this thesis a rough figure is about ten minutes over a two–hour period. During this time, the locus of heating could move too, reflected in a potential time–dependence in the exponent.

---

[4] Dynamical plasma behaviour even with constant (time–independent) heating has been investigated by eg. Müller et al. (2003).

[5] The word "flare" in the name is chosen rather arbitrarily to denote transient events, no claims about the heating's physical nature are made.

2.4.5 Loop Heating

The heating function is one of the three major contributors to the plasma temperature, the other being thermal conduction and radiation. In a steady state the divergence of these have to sum to zero

$$\nabla[F_c(z) + F_r(z) + F_h(z)] \quad = \quad 0. \tag{2.51}$$

$F_h(z)$ and $F_r(h)$ represent energy gained from, and lost to, external reservoirs, thus they depend only on the local plasma state. Conduction of energy is from higher to lower temperature, and will cause sinks (or sources) at the boundaries, but only internal redistribution in the corona. Due to the high temperature above the TR, it will act as a heat sink in practical cases.

Plasma dynamics in the absence of impressed waves are created by the interplay of these three fluxes.

Chapter 3

Spectral Observations by SUMER

We have two hours of continous and high–cadence observations from the SUMER instrument flown on SoHO, in which a strong transient loop brightening event occurs. The observations were taken with the slit in a favourable position, intersecting the loop near a foot–point, and thus obtaining information about the transition region (TR) – corona interface, where the transient event is plainly visible in all five monitored bands, covering a temperature interval of $1.0 - 2.5 \times 10^5$K. I present these observations here, with an account of the methods for noise reduction used on them. I then describe the intensities, plasma velocities and line widths determined from the data. In closing, I summarize the results, but delay a full discussion to the end of the next chapter.

3.1 A Brief Presentation of the Instrument

Solar Ultraviolet Measurement of Emitted Radiation (SUMER) is a stigmatic spectrometer designed for high resolution observation of the chromosphere, transition region and lower corona.

Stigmatism allows for spatially extended observation through one of SUMERs four slits. The spectral resolution of the instrument is 43mÅ per pixel in the first band, and it has a full wavelength coverage of 780–1610Å in the first order for detector A and 660–1500Å for detector B. A window of roughly 40Å width in the first order and 20Å in the second is visible to the detector at any given time.

The diffracted light is recorded on one of the two detectors A and B, each a 1024 by 360 pixel microchannel plate (MCP). A potassium bromide (KBr) coating on the central parts of the MCPs (pixels 280 through 770 for detector B) increases the detector efficiency there, at the beginning of its operation the efficiency was about 20% at 1200Å (diminishing with increasing wavelength), about four times the efficiency of the bare MCP. The efficiencies of the detectors deteriorate with time, but updated radiometric calibrations are made by the SUMER group at regular intervals.

Due to the limited telemetry rate, only a few narrow windows of the spectrum can be transmitted to the earth. These windows, commonly 25–50 spectral pixels wide, have to be selected according to the scientific goals of the research programme.

The instrument and its operation is described in detail by Wilhelm et al. (1995).

3.2 The Observations

3.2.1 Instrument Settings

Our observations were made through the $1'' \times 120''$ slit[1], and recorded on detector B. The spatial sampling is at about $1''$ intervals, ie. a $2''$ spatial resolution.

Five windows, each 50 spectral pixels wide, were selected for this program. As the observational focus was on transition region (TR) moss, three of them were tuned to ions seen in the TR and lower corona, and the two remaining were tuned to a chromospheric line and a coronal line, respectively. With a normal telemetry rate of 10kbit/s and a compressed size of 8 bits per pixel, this allowed for a cadence of about 28 seconds (25 seconds of exposure, and 3 seconds added due to instrument overhead). The five windows are listed in table 3.1 by the main lines present in each. In addition to the chosen lines, we can see a faint Fe XII–line in the blue wing of the N V λ1242 window. The temperatures indicated are those of the peak ionization fraction for that element.

Line	Temperature	Resolution
N V λ1238	0.20 MK	43.0 mÅ/px
N V λ1242	0.20 MK	43.0 mÅ/px
Mg X λ624	1.3 MK	21.5 mÅ/px
Si II λ1251	13 kK	43.0 mÅ/px
O V λ629	0.25 MK	21.5 mÅ/px

Table 3.1: The main lines in the bands monitored by SUMER, with the temperature of maximum formation and spectral bin widths.

With the cadence of 28 seconds, we captured a total of 22 spectra in the time interval 10:03:56–10:13:45[2]. All in all, 240 images were taken from the

---

[1] At Lagrange point 1 (0.99AU from the sun), $1''$ covers about 715km on the photosphere.

[2] All the times given are in UTC.

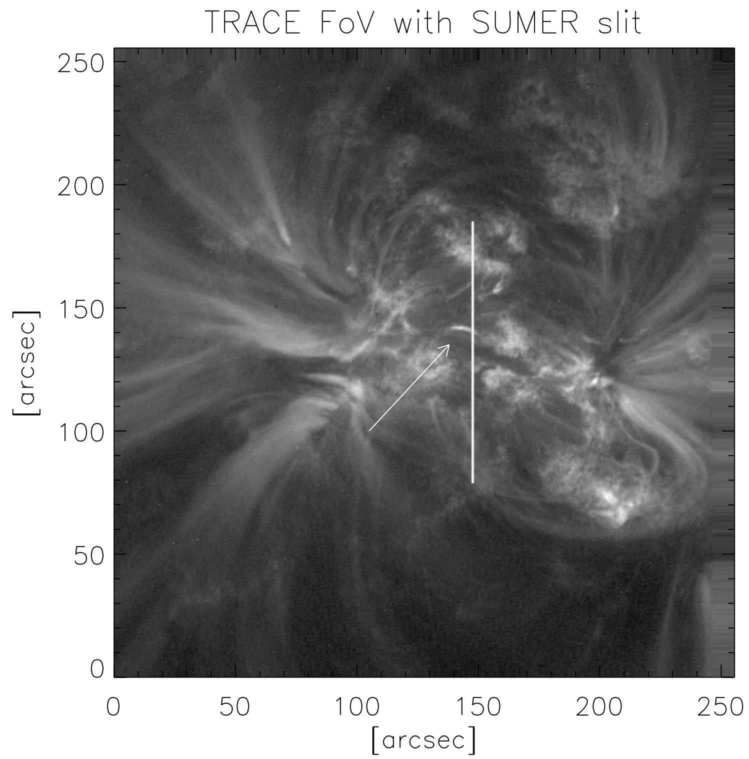

Figure 3.2.1: The full TRACE field of view with the SUMER slit interposed. The the loop at its most intense is indicated by the arrow.

start of the study at 09:17:05, June 4 1999.

It should be pointed out that coronal moss (see eg. De Pontieu et al. 2003) was the intended objective of the observation program, and not the loop in which the transient event occurs; it was rather a fortuitous bonus. The lines selected are therefore not well suited for the task of describing such an event. Nevertheless, there is much data here that can be utilized in an attempt to understand it.

3.2.2 Joint Observations with TRACE

The SUMER scans were made in concord with the EUV imager TRACE, as part of a joint observation program. In figure 3.2.1 we can see how the fields of view for the two telescopes overlap. This TRACE image shows the loop at its most intense, and the slit intersects it nicely. I discuss the TRACE data separately in chapter 4.

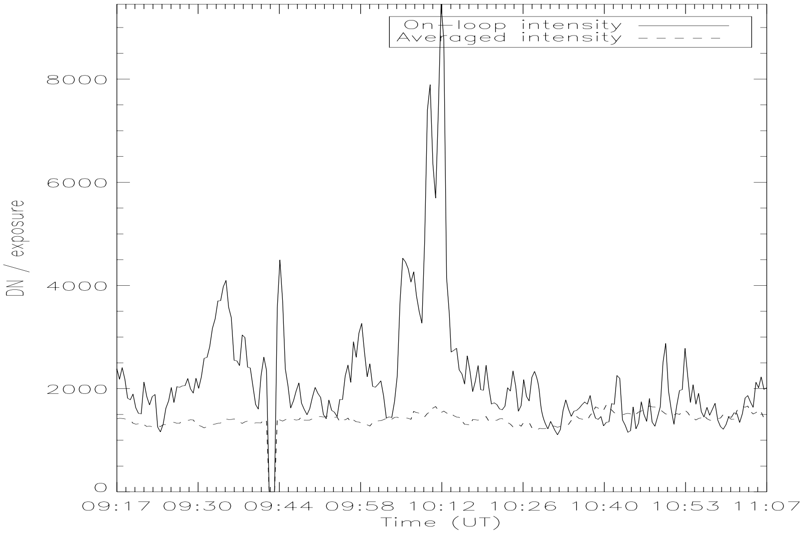

Figure 3.2.2: The amplitude of the event: the data numbers (DN) in N V λ1238 averaged over the whole slit compared with a point (spatial pixel #70 from the south) on the loop.

3.2.3 The Data Set

The data was provided by Bart De Pontieu of Lockheed Martin as a set of IDL `save`-files, featuring both the raw data and the results after correction for systematic errors and application of the genetic algorithm for line profiling described in section 3.3.2.

The data was not reversed, which means that the northmost pixel still had the highest pixel value (a peculiarity of the SUMER instrument: it is mounted "upside–down", making the pixel count increase from the north). I changed this, so that pixel numbers behave as we expect, with south at pixel #0, and use this reversed direction in the rest of this chapter.

In addition, the set includes the two FITS files (uncompressed but not reversed) which together comprises the first 120 exposures.

3.2.4 An Outline of the Data

Figure 3.2.2 illustrates how the radiation from the coronal loop around 10:15 stands out from that of the rest or the observed region. The plotted lines compare the mean count rate in the N V λ1238 window over the whole slit with that in a pixel (#70 from the south) on the loop indicated in figure 3.2.1. The emission suddenly rises to more than four times the background level. This peak is the main topic of this thesis.

Two frames (no. 55 and 56) are missing in the data set, probably due to telemetry loss. These are replaced by the mean of their neighbours in later plots. Since they occur at 09:40, they are of no concern in this study. The data from the northmost pixels are also missing, this is comfortably far away from the region of interest to us.

3.3 Systematic Errors

Like any other telescope, SUMER introduces some artifacts into the images that the we need to remove. The most important causes of systematic errors are the thermoelastic oscillations, instrument dead time, flat fielding, instrument broadening and other ions emitting in the same windows as the line of interest. While the first three of these effects can be treated separately, the latter two are entangled and must be tackled as two parts of the same problem, that of *line fitting*.

3.3.1 Image Artifacts

Dark Current and Flat Fielding

The level of dark current in the SUMER instrument is very low, and is easily subtracted.

A stronger effect is exhibited by the non–uniform sensivity of the detectors, which causes the Analog-Digital Converter (ADC) to modulate every second pixel by 19%, leaving a marked pattern in the output. As Teriaca et al. (2003) points out, this effect can be seen through its distinct “signature” peak in the spatial power spectrum, and a proper flat fielding is confirmed by the lack of this peak.

Geometric Correction

A geometric distortion resembling vignetting was corrected with the `SUMER_DESTRETCH` procedure written by Tom Moran as part of the SUMER Reduction Package (Carlsson 1996)[3].

Instrument Dead Time

Dead time in the instrument has to be taken into account when the count rate exceeds 50×10^3 counts/s. The count rate is reported in the `X/YEVENT` header tags, but as these are not included in the data set, I estimate the peak rate as simply the time average for the exposure with the highest data numbers — 19×10^3 counts/s. Even when allowing for large deviations from the mean, this is comfortably lower than the indicated treshold.

---

[3] Available online at http://www.astro.uio.no/ matsc/sumer/.

Thermoelastic Oscillations

The telescope employs heaters and radiators, in order to keep its temperature as close to the indicated (20 ± 1) Centigrades as possible. Unfortunately, the heaters do match the exact heating requirement, and thus the optical bench suffers from thermal expansion and contraction as they are turned on and off. The effect of these changes in path length is a periodic broadening and shift of the spectrum, dubbed Thermoelastic Oscillations (TEOs). They are discussed, among others, by Rybak et al. (1999).

The fix we employ is quite simple — we subtract the average of each parameter over the slit at each time step. More precisely: The mean value has a clear drift, and since the results in Rybak et al. (1999) indicate that the drift is linear, we do a least squares fit on the results, and remove the first degree term. Of course, this does leave us with the problem of determining the zero of the function, where the values measured by SUMER are free of this bias. This can be done by looking at the neutral chromospheric calibration lines, but since they are not in the data window, I arbitrarily select the value at the start of the observation.

This method reveals a drift of 2.0μÅ/s towards longer wavelenghts for the O V line, and 3.2μÅ/s and 3.9μÅ/s for the lines of N V. The Mg X line is barely shifted, 0.9μÅ/s in the *opposite* direction. The 3μÅ/s measured by Rybak for lines around 1000Å are in (weak) agreement with these values, except for Mg X.

The same heating is also responsible for a slight broadening of the profile. A casual fit to a constant background temperature indicate a linear growth of about 10^5K throughout the observation time (15K/s).

3.3.2 The Instrument Profile

Even after we have corrected for the effects mentioned above, the profiles of the measured spectra will deviate from that of the true emission line in each band. This is due to the finite widths of each spectral bin — we are essentially fitting a continous function to a histogram — and noise. The extraction of the individual parts contributing to the full SUMER spectrum in each window is done through line fitting algorithms, and we use the *genetic algorithm* (GA).

The Genetic Algorithm

The algorithm is described well by Charbonneau (1995), whom provides working examples and computer code.

The gist of the scheme is that we make a large set of different initial predictions which can be quite vague. In our case they contain our initial guesses for the line intensities I^i, shifts λ^i, widths w^i and two linear continuum coefficients (c_0^i, c_1^i). These (say N) elements of our starting set

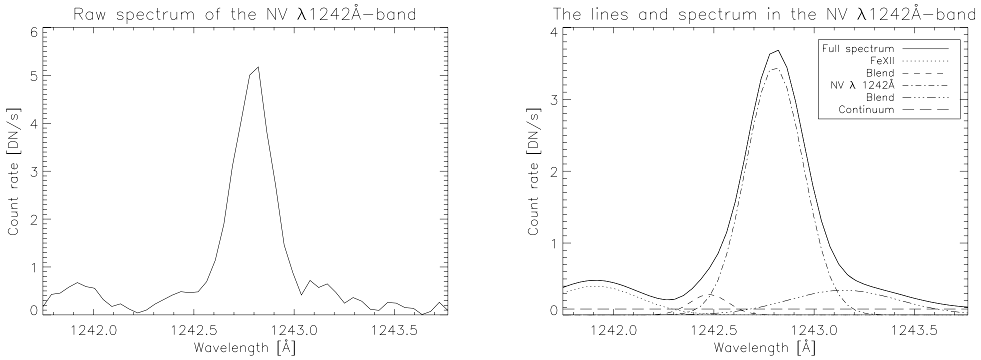

Figure 3.3.1: The raw (left) and GA–fitted spectra of N V λ1242. The reduced χ^2 statistic of the fit is 0.17.

are termed *genes*[4]:

$$\text{gene}^i \quad = \quad (I^i, \lambda^i, w^i, c_0^i, c_1^i), \tag{3.1}$$

and the name of the set itself is the *population*,

$$\text{population} \quad = \quad \{\text{gene}^i \quad | \quad 1 \leq i \leq N\}. \tag{3.2}$$

Each gene encodes for a specific *phenotype*,

$$\text{phenotype}^i \quad = \quad I^i \mathrm{e}^{-\frac{(\lambda-\lambda^i)^2}{2(w^i)^2}} + c_0^i + \lambda c_1^i, \tag{3.3}$$

which is the prediction of the total radiation in a line described by gene i. With basis in the population of initial guesses, we compare the χ^2-fit of each phenotype with the measured radiation, and award the encoding gene a number of *offspring* based on the goodness of the fit. After all phenotypes have been weighed, the offspring of each gene are added to a new population, and the process is repeated iteratively.

In this form, the algorithm is a cumbersome way of choosing between N crude prediction. It would decide on the best of our initial guesses, but only luck would make this fit actually good. The strength of the scheme is that we can introduce small changes into each offspring during reproduction. Each parameter in the gene is subject to these changes — stochastic *mutations* which cause small adjustments, and *crossing over*, which is a form of "mating" with other genes.

During the early iterations, the population will be quite diverse, and crossing over leads to rapid motion over the whole of the parameter space. In the late phases the genes will have been homogenized by the award scheme, so that the mutations can be seen as a fine–tuned search near the optimal fit.

---

[4] In the data reduction, four gaussians were used rather than the one here; in addition to the linear continuum coefficients.

The procedure terminates when we have reached a predetermined number of generations, or the maximum difference between the phenotypes is below a given treshold.

The Genetic Algorithm Parameters Used

The parameters used in this thesis was suggested by de Pontieu (personal communication), and are in the terminology of Charbonneau (1995) a population of 100 genes evolving for 300 generations with full replacement between each generation, subject to variable mutation rates. High crossover probability (85%) combined with high selection pressure forced the population rapidly toward a common solution. Elitistic reproduction (haplodiploidy) ensured that at least one copy of every fit gene was replicated unchanged into the next generation.

Resultant Profiles

In figure 3.3.1 we see the results of this fitting scheme on one sample N V λ1242 spectrum. The left panel shows how the raw spectrum looks. In addition to the main N V line there is "something" in the region around 1242.0Å, and a broadening in the wings of the central peak. Consulting a line list (eg. Ralchenko et al. 2005) we find that the 1240Å feature is probably the Fe XII $3s^2 3p^3\, {}^2P^o_{3/2} \rightarrow 3s^2 3p^3\, {}^4S^o_{3/2}$ line (a magnetic dipole transition with Einstein–coefficient $3.17 \times 10^2 s^{-1}$), while the wings are blend in the N V line. The blends will make analysis of the N V λ1242 line difficult, but fortunately both lines N V λ1238 and O V λ629 look good.

The GA breaks this down to the constituent parts shown in the right panel.

Using the doppler techniques described in section 2.3.2 we can now derive bulk plasma line-of-sight velocities and, where we are able to fit the emission spectra to Gauss curves with concrete line widths, to plasma temperatures. The latter will, because the spectra really show the integrated emission from the whole column along the line of sight, be of rather low certainty.

Radiometric Correction

Radiometric calibration — the conversion of the data numbers to physical quantities, ie. the radiated energy or photon counts — of the raw data numbers is done through a SolarSoft routine described by Wilhelm (2000). In the following sections I report the intensities in photons sr^{-1} s^{-1} cm^{-2} $Å^{-1}$, mainly because this should facilitate comparison between the columns seen by SUMER and the volumes calculated by TTRANZ.

3.4 Line Intensities

It is in the intensity of the radiation we first notice the loop event. It lights up with a flash, practically in the center of the data, both spatially and in time. The panels of figure 3.4.1 show us just how much the radiation increases during this short period of time, starting just after 10:00: The photon counts suddenly triples in all the bands over a time of no more than 15 minutes, and just as suddenly falls back to the background level.

The four X–T diagrams in figures 3.4.2 are intended to give a global view of the development in each band. The loop can be found close to the middle of the diagrams, around spatial coordinate $70''$. The event occurs around 10:10, it is most readily seen in the nitrogen and oxygen lines, where it is in fact the most strongly emitting source. On the other hand, it is very hard to see in the Fe XII line. The event is depicted in detail, as observed in the O V line, as a close–up in figure 3.4.3.

Table 3.2 is a statistical breakdown of the graphed information. It contains four sections: the top half is data from a point on the loop (spatial pixel #70 from the south), divided into the mean intensity, deviation of the mean and the peak non–flashing[5] intensity in the left columns, and the global peak for this spatial pixel in the rightmost column. The lower half of the table lists mean values for non–loop pixels. It is divided in the same way, but here a separation into event and off–event frames does not really matter. The TRACE intensities are presented in DN/s because it is difficult to discern between O and Fe emission in low temperature structures, and the results from deconvolution are wavelength–dependent.

The table quantifies what we see in the graph, that the loop is quiescent in all bands, except O V, before and after the event occurs. The large variance in the O V data is caused by the strong peak leading the event by 30 minutes. This same peak can be seen in N V λ1242 as well, but it is not as pronounced there.

TRACE statistics from the pixel on the loop centroid where it was intercepted by the SUMER slit is included in the table[6], and we see how the data from this telescope matches the SUMER data, the flash is really strong over the huge temperature range from N V to highly ionized iron.

All the lines share the same temporal behaviour, the event occurs in two stages: At 10:03:28[7] the emission in all bands grow, and after about two minutes tapers off down to a plateau. The plateau stage lasts until 10:09:04, and is followed by two peaks in rapid succession, at 10:10:28 and 10:11:52,

---

[5] The frames considered as during the event are 101–129 (10:04–10:17).

[6] The loop appears more calm in the TRACE data, with a low variance. This is partly due to smoothing introduced by the way its 40 second cadence images were synchronized with the 28 second cadence SUMER images.

[7] The times indicate the start of each exposure, as reported by SUMER. Their precision is limited to the observation cadence of 28 seconds.

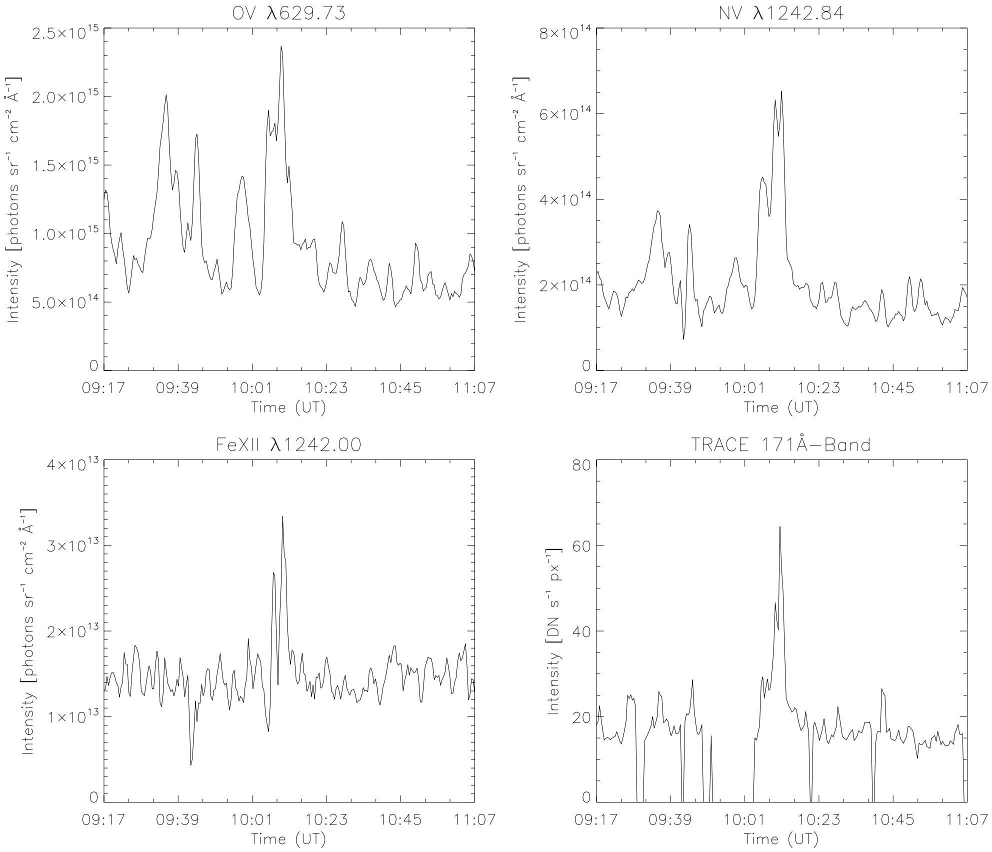

Figure 3.4.1: Loop intensities in the lines N V λ1242, Fe XII λ1242 and O V λ629. The emission in the corresponding TRACE λ171–band X–T column is included for comparison.

Line	Before and after the event Mean	SD	Maximum	The event Maximum
Measured on the loop				
N V λ1242	1.78×10^{14}	5.89×10^{13}	4.14×10^{14}	7.00×10^{14}
Fe XII λ1242	1.43×10^{13}	3.06×10^{12}	2.28×10^{13}	3.91×10^{13}
O V λ629	8.45×10^{14}	3.36×10^{14}	2.14×10^{15}	2.54×10^{15}
TRACE λ171–band	17.1	3.20	28.6	64.4
Off the loop measurements				
N V λ1242	1.19×10^{14}	3.80×10^{13}	2.71×10^{14}	2.71×10^{14}
Fe XII λ1242	1.73×10^{13}	4.13×10^{12}	2.93×10^{13}	2.93×10^{13}
O V λ629	4.72×10^{14}	1.92×10^{14}	1.20×10^{15}	1.20×10^{15}
TRACE λ171–band	14.3	2.24	20.5	20.5

Table 3.2: Intensity statistics for N V λ1242, O V λ629, Fe XII λ1242 and the TRACE λ171–band. All units are photons/sr/cm^2/s/Å except those for TRACE, which are DN/s/px.

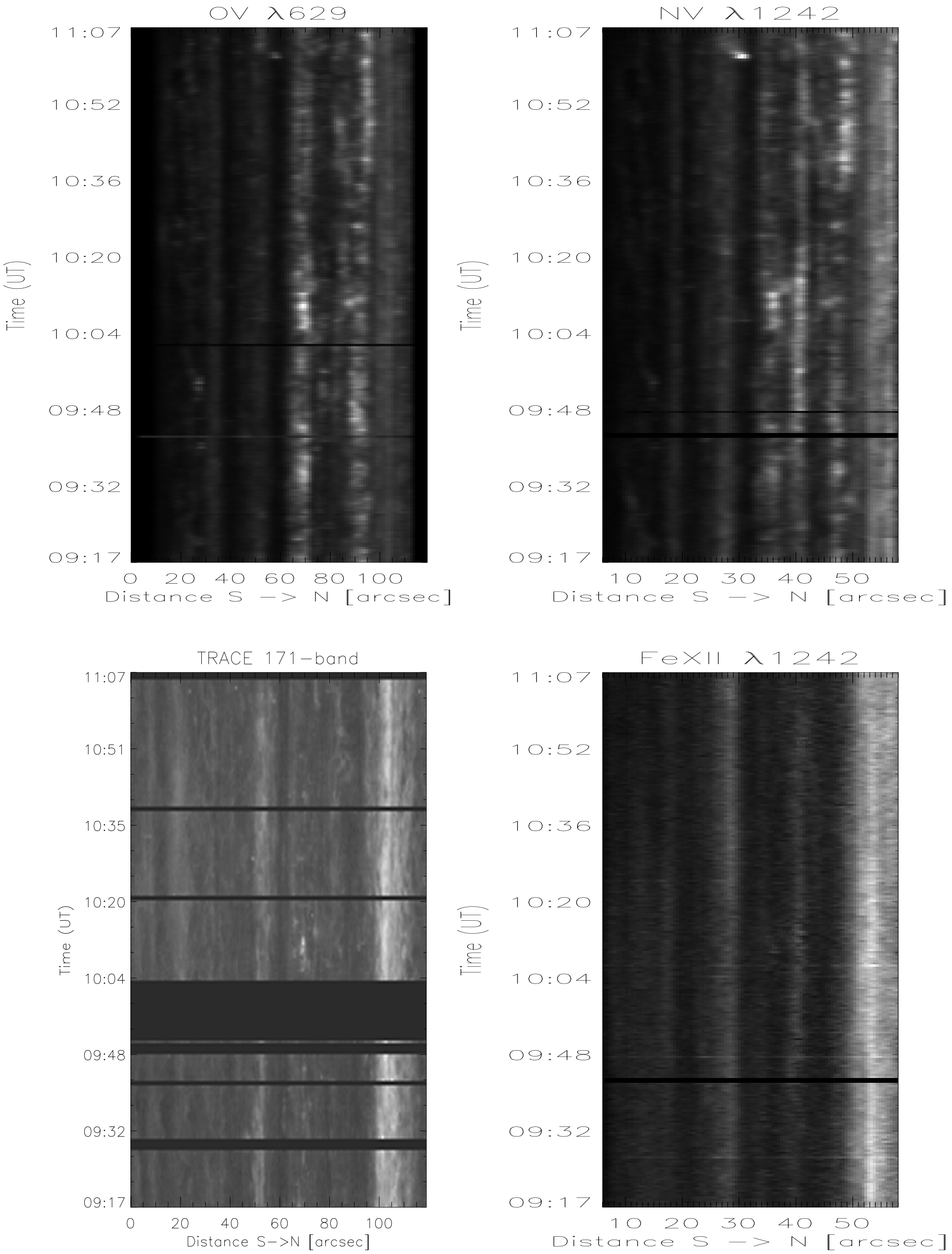

Figure 3.4.2: Development of loop emission intensity in the four bands O V λ629, N V λ1242, TRACE λ171–band and Fe XII λ1242.

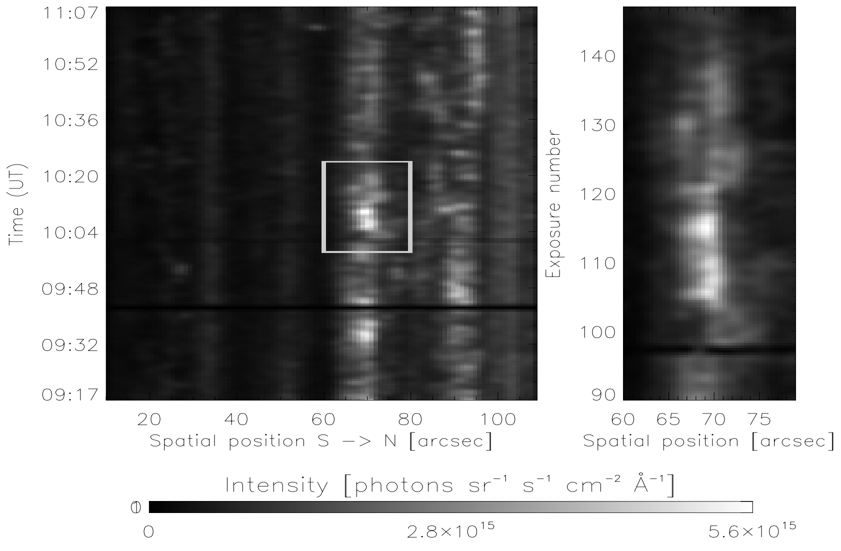

Figure 3.4.3: The X–T intensity plot in O V λ629, with a detail from the time and region around the event.

after which the intensity quickly settles back to the background level.

In a closer look it does appear as if the initial plateau from 10:05:20 to 10:09:04 is actually two peaks, but of lower amplitude than the following two, giving four peaks separated by a period of 2.0–2.5 minutes, not far from the expected loop traversal time for an acoustic wave, but the existence of the first two peaks is not statistically certain.

A Fourier transform reveals significant low frequency components[8] at 443 seconds (2.26mHz) and 18.5 minutes (900μHz). The main brightening occurs superimposed on one of the 2.26mHz oscillation, suggesting that it could be a high–amplitude part of a recurring wave motion, rather than a singular event.

In the TRACE images (see section 4.3, particularly image 4.3.4) we see evidence of two or more “loop threads” close by each other, exhibiting similar transient behaviour. This neighbouring loop is the source of the brightening seen in the close–up in figure 3.4.3, at slit coordinate $66''$. Their $4''$ (at the most) separation is more easily resolved by the $0''.5$/pixel TRACE imager.

3.5 Velocities Inferred from Line Shifts

The bulk velocities of the emitting plasmas are calculated from the moment of the line profile, as described in section 2.3.3. This method utilizes the

---

[8] A sample power spectrum is presented in section 3.6.

fact that a line profile $L(\lambda)$ is inherently a probability density function, and as such has meaningful moments. The first moment of the line (and hence intensity) profile is the expected line mean

$$\langle\lambda\rangle \;=\; \int \lambda\, L(\lambda)\, \mathrm{d}\lambda, \tag{3.4}$$

which is connected to the plasma velocity through the Doppler shift $\Delta\lambda$,

$$\langle u\rangle \;=\; \frac{c(\langle\lambda\rangle - \lambda_\mathrm{e})}{\lambda_\mathrm{e}}. \tag{3.5}$$

When we apply this to a line observed by a spectrograph, which measures intensity in finite width spectral bins rather than continously, we need use the discretized equation 2.30

$$\langle u\rangle \;=\; \frac{\sum_{i=1}^{N} u(\lambda_i)\, I(\lambda_i)}{\sum_{i=1}^{N} I(\lambda_i)}, \tag{3.6}$$

where λ_i represents the wavelength interval received in spectral bin i, $I(\lambda_i)$ the count number in that bin and $u(\lambda_i) = c(\lambda_i - \lambda_\mathrm{e})/\lambda_\mathrm{e}$.

The method provides only line–of–sight (LoS) velocities. To convert these to absolute quantities, we need to adjust them to the inclination of the flow ϕ,

$$u_\mathrm{real} \;=\; u_\mathrm{LoS}\cos(\phi), \tag{3.7}$$

but at least for reasonably small values of ϕ the velocity response will be nearly linear, allowing us to discover at least the relative changes in velocities even if we do not know the exact angle.

Results

The results are shown in figure 3.5.1; each panel represents one band. Only N V $\lambda1238$ and O V $\lambda629$ show strong positive results for times near the event. The lack of response from the N V $\lambda1242$ is most likely due the line fitting problems caused by the blend, while the Si II and Mg X lines may simply be too weak to give absolute results. The velocity average over the whole slit was subtracted from each of the graphs in the plot.

Si II ions should exist only in the chromosphere, making their radiation valuable for calibration of the lines, as SUMER lacks absolute calibration by an onboard lamp. Here the emitting plasma is, albeit with a large deviation, nearly stationary, as expected.

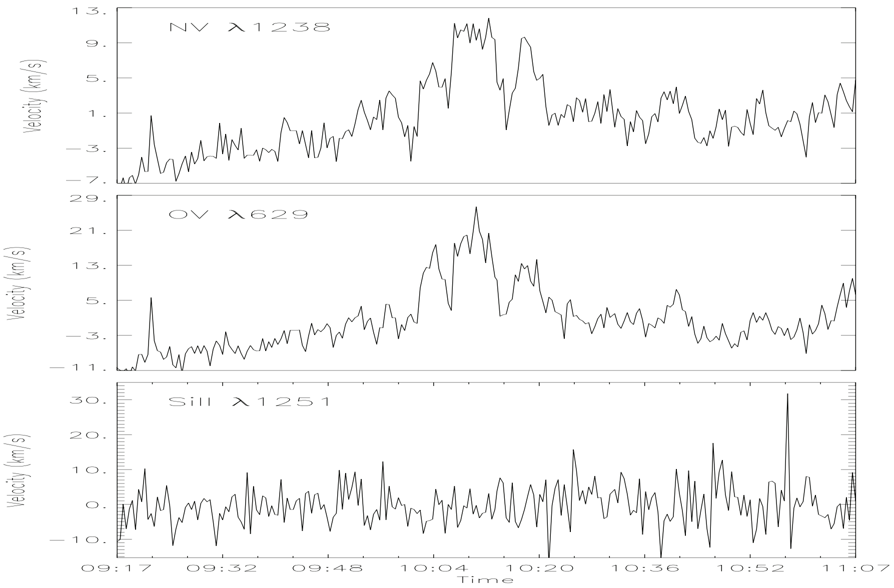

Figure 3.5.1: Time development in the velocities in the loop as determined from radiation in N V $\lambda1238$ (top), O V $\lambda629$ (middle) and Si II $\lambda1251$ (bottom). Positive values indicate redshifts.

Focusing on the two lines that do react to the event, we see that although the lines' response in intensity was very sharp and short–lived, the change in velocity seems to be gradual and go on for the better part of an hour. The amplitude of the change is also quite low, at no more than some 20km/s, which is lower than u_{sound} over most of the loop. The general profile of the velocity changes is that of a bell curve, but during the actual event, two sudden "snaps" of blue–shift occurs, at times 10:05:48 and 10:14:04, corresponding to just after the initial and final peaks in emission, respectively. In other words, the strongest emission occurs when the plasma is at its most red–shifted.

The two ions' velocities are comparable, with $u_{\max} \sim 15$km/s for N V and $u_{\max} \sim 20$km/s for O V. This follows naturally from the continuity equation when we know that O V is found in a hotter, and thus less dense, height in the loop. If we assume that the pressure is constant in the loop, we can use the familiar Bernoulli's equation to estimate the relative change in density at the two heights. This equation can be written

$$\overline{m} n_{e,1} u_1^2 + 2 n_{e,1} k_B T_{e,1} \quad = \quad \overline{m} n_{e,2} u_2^2 + 2 n_{e,2} k_B T_{e,2}, \tag{3.8}$$

where the subscripts 1 and 2 here correspond to O V and N V, respectively. I use the relation $n = \rho/\overline{m}$ (see chapter 2) and the assumption $n = 2n_{\text{e}}$.

Solved for the relative density, 3.8 becomes

$$\frac{n_1}{n_2} = \frac{\frac{1}{2}\overline{m}u_2^2 + k_B T_{e,2}}{\frac{1}{2}\overline{m}u_1^2 + k_B T_{e,1}} \tag{3.9}$$

which, when we insert the velocities quoted above and the formation temperatures listed in table 3.1 (20km/s and 2.5×10^5K for O V, 15km/s and 1×10^5K for N V), gives us a ratio of

$$\frac{n_1}{n_2} \approx 0.56. \tag{3.10}$$

This is a reasonable density drop even over a short height in the TR layer of the atmosphere.

3.6 Temperatures Derived from Line Widths

A Note on the Method and its Validity

In section 2.3.2 the connection between line width and plasma temperature in the coronal plasma regime is described. If we assume that the plasma is fully thermalized so that ion and electron temperatures are equal ($T_e = T_i$ for all i) and that we have properly corrected for instrument broadening, we can derive a crude estimate for the temperature at which each line formed by inverting equation 2.23:

$$T = \left(\frac{c\,\Delta\lambda_D}{\lambda}\right)^2 \left(\frac{M_i}{2k_B}\right), \tag{3.11}$$

where $\Delta\lambda_D$ is the line width.

This estimate is crude not only because of the intrinsic uncertainties in the data (filling factor, column variability and so forth), but also because we have no real guarantee that the plasma will actually follow a Maxwellian velocity distribution. For instance, Shoub (1983) advices against this last assumption for plasma in the lower TR, where $10^4 < T_e < 10^5$K. Thus we would, generally speaking, be better off with line ratio comparisons, but none of the available lines lend themselves to that method of analysis.

The most important effect responsible for skews in the derived temperatures is the line variation up through the emission column. Since this effect can only cause widening of the lines, which translate to higher temperature estimates, we can safely assume that our results will err on the high side. In the simplest case of two convolved gaussians with the same width and shift, the deviation is increased by a factor $\sqrt{2}$, ie. a doubled temperature estimate. The effect is observed in the synthetic spectra of chapter 7, in which the temperature estimate based on an integrated column emission spectrum from a numerically analyzed plasma exceeds even the maximum true plasma temperature in the investigated loop.

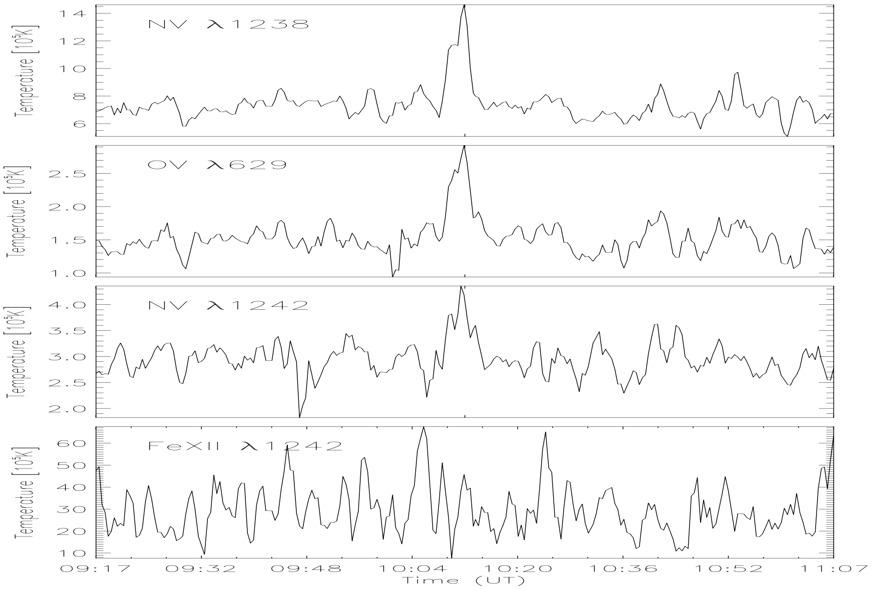

Figure 3.6.1: Temperature development in four selected SUMER bands: N V λ1238, N V λ1242, O V λ629 and Fe XII λ1242. Some periodicity is seen, particularly in N V λ1242.

As a crude check on a crude estimate, we can use our knowledge of the ionization equilibrium of the emitting ion to set upper and lower bounds on the temperature. Of course, during the brightening we should allow the ionization equilibrium more slack since the time scales of change are short, so we lose even this one check on our results. The five main lines are listed in table 3.1; in addition Fe XII peaks at 1.26×10^6K.

Results

As presaged above, we run into problems with this method; the different lines seem to have formed at widely different temperatures. This to some degree is understandable, we would not expect Fe XII to exist at the same temperatures as N V and O V in the first place. What we could hope for, however, is reasonable temperatures for the lighter elements, especially the two lines emitted by the same ion.

Of the two nitrogen estimates, only the λ1242 line is at all plausible, with some 10% of the total nitrogen in that ionization stage at the mean temperature of 2.8×10^5K. However, because of the blend found during the line reduction we should not rely too much on those results. The λ1238 line is “safer” in this respect, but its line widths are obviously far too high.

Fe XII shows low, but plausible, temperatures inferred from the widths, with a mean (with high variance) of 7×10^5K.

The O V data show rather low temperatures for this ion, but they are to some degree supported by the presence of the C IV radiation we see in TRACE images. Since I claimed above that this temperature should represent an upper bound, and that little O V can exist in a cooler plasma, this seems like the closest we can come to a true measure of the temperature, a quite cool loop.

Fortunately, this exercise is not completely pointless: despite all the cautions, there is a concrete link between temperature and line widths, and we see that all widths grow during the event. Further, they all grow by approximately the same relative amount, indicating that the temperature is actually increasing strongly at that time. Thus we have at least a qualitative view on the temperature development, even though the absolute quantification eludes us.

The Mg X and Si II Bands

These two bands have too weak emission for us to reduce the data in them by either of the two methods (Teriaca et al. 2003 or Charbonneau 1995). Their line profiles cannot be fitted to a bell curve, therefore I have not included them here.

3.7 Periodic Variations

Several periodic variations can be seen in the data, in addition to the obvious emission burst. Especially in the N V λ1242 line width graph (the third panel of figure 3.6.1) are several of these variations visible.

To investigate which modes that are real, I compute power spectra of the intensities, velocities and line widths.

A 2.26mHz–fluctuation is seen in width, shift and intensity plots, and is probably real. However, the strong 900μHz signal could very well be a component of the main peak, as the radiation peaks at the same time as the maximum of the composite of these two periodic functions.

The are a few other peaks seen above the 1σ marker, of these we can probably attribute the 5 and 6mHz oscillations to internetwork regions (cf. Wikstøl et al. 2000).

Noise Estimates

The amount of noise in the signal was estimated by calulating the power spectrum of a sequence of samples from a normal distribution with the same mean and variance as the signal. The 1σ variation in the higher frequency (ie. without the sample mean) modes of the noise spectrum is plotted in each panel.

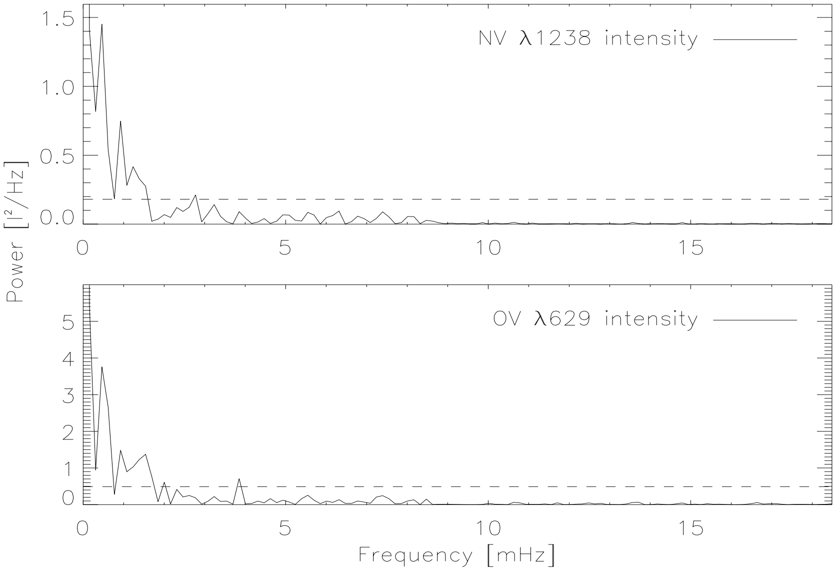

Figure 3.7.1: Power in the N V λ1238 and O V λ629 intensities observed at loop pixel #70. The dotted line shows the 1σ estimate of the noise level.

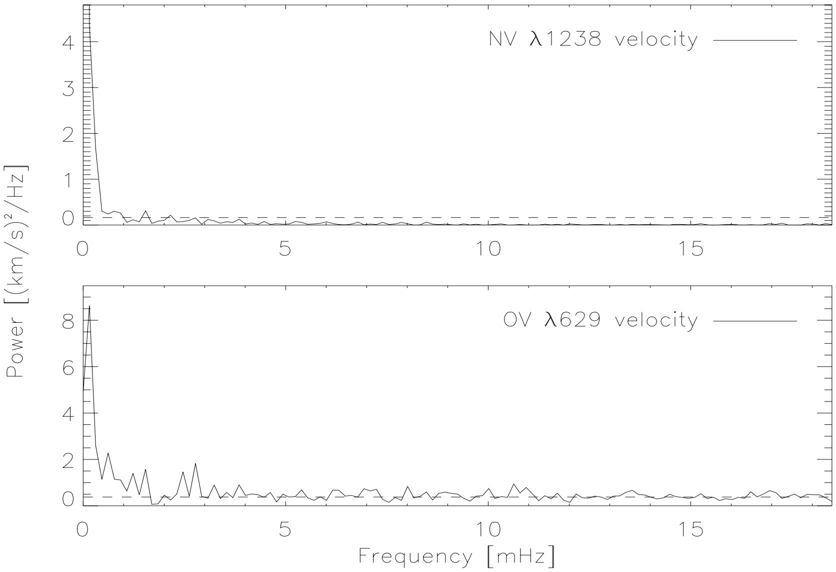

Figure 3.7.2: Power in the N V λ1238 and O V λ629 line shifts observed at loop pixel #70. The dotted line shows the 1σ estimate of the noise level.

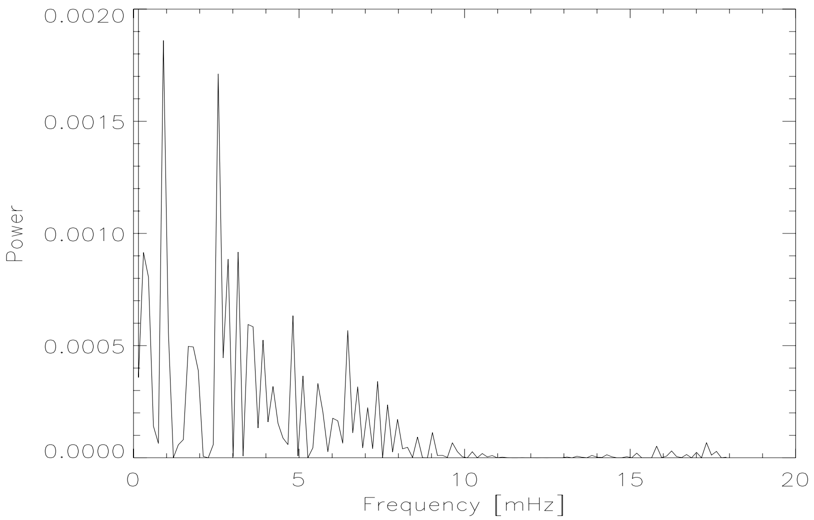

Figure 3.7.3: Power in the N V λ1242 line widths observed at loop pixel #70. See the text for a caveat about this spectrum.

3.8 Interim Summary

The goal of this chapter was to describe the overall characteristics of the event as seen by SUMER, and to quantify the physical process by the three parameters temperature T, bulk velocity u and emission I_λ. To sum up the results of this chapter:

- Over the 15 minute period of the event, emission rates grow by a factor 2–3.
- Every band is affected, even Mg X, Fe XII and Si II. Of these the two former exist at coronal temperatures, and the latter at chromospheric. The superior bands for analysis of this event seems to be N V λ1238 and O V λ629.
- The event appears to take place in two stages, a plateau stage lasting some 5–6 minutes, followed by two very strong peaks, each lasting about 2 minutes.
- All the observed bands light up in phase at this temporal resolution. The phases are treated in more detail in the next chapter, together with the data from two TRACE bands.
- We do have an increase in the temperature (or at least line widths), and

even though only two of the bands indicate plausible absolute values, all of them agree on a growth by a factor 1.5 or more.

- The plasma velocities respond earlier to the event. This response is only seen in the N V λ1238 and O V λ629 bands, in which it occurs at least 15 minutes before any visible change in emission, with a slowly increasing red–shift. The graph of the line shift versus time has the shape of a bell curve, but with two sudden blue–shifts immediately after the first and last emission peak.
- A wave motion (oscillation) can be observed in the loop both prior to and after the event, with main constituent frequencies at 2.26mHz, 1.20mHz and 900μHz. The event coincides with the peak of an oscillation.

More information is available in the complementary TRACE data set, and at the end of the next chapter I discuss what we learn from both sets combined.

Chapter 4

TRACE Observations

Active region NOAA 8558 was observed by TRACE for the full two hour duration of the SUMER observation, at comparable cadence. The wavelength bands captured were the $\lambda171$ band (O VI and Fe X /XI), the $\lambda1550$ (C IV and chromospheric iron) and the $\lambda1600$ broadband. The transient event we are studying is conspicous in the $\lambda171$ and C IV images, but practically invisible in $\lambda1600$. In this chapter I present these TRACE observations and compare them with those from SUMER.

The combined information gathered in the two observations should provide enough boundary and transient requirements for us to set up realistic simulations of such a loop. This will in turn provide more knowledge about such dynamic behaviour as we see here.

4.1 A Brief Description of TRACE

The *Transition Region and Coronal Explorer* (TRACE) is an earth-orbiting observatory equipped with both broad– and narrow band UV filters. It can monitor the Sun in three narrow EUV bands ($\lambda173$, $\lambda195$ and $\lambda284$), four broader UV bands ($\lambda1550$ (C IV), $\lambda1600$, $\lambda1700$ and Lyα) as well as white light centered on 500nm. An image is focused by a 30cm aperture Cassegrain telescope and recorded on a 1024 by 1024 pixel CCD with a plate scale of $0''.5$/pixel[1] (about 725km/px), giving an $8'.5$ by $8'.5$ view of the Sun. A 512 by 512 pixel subset of the CCD image was telemetered after the observations on 1999 June 4, from 09:17:05 to 11:07:50[2].

The telescope is divided into four quadrants sensitive to different wavelengths, and the appropriate quadrant is selected through the active secondary mirror. Any unwanted white and far UV light is shut out by filters embedded in two filter wheels placed in the light path between the secondary mirror and the detector. Each wheel has three different filters and

---

[1] The PSF was measured by Golub et al. (1999) to have a FWHM of $1''.25$.

[2] All listed times are in UTC.

an open "window", and the combination of filters to use is determined by the wavelength of interest and the amount of stray light. For EUV observations, they will be the aluminum filters, with a default configuration, used in these observations, of having the first one in Al position and the second open, the "AO" (Aluminum, Open) mode.

Detailed information about the satellite's design and capabilities can be found in Handy et al. (1999) and the references therein.

Because this telescope has about twice the angular resolution of SUMER, some of the spatial features will be seen in greater detail when observed through this telescope. AR8558 is positioned at coordinates (N16°, W22°), giving us a viewing angle of 27° ($\mu = 0.89$).

Line	Band	FWHM	Temperature
Fe IX	λ171	6.4Å	0.63 MK
O VI	λ173	"	0.32 MK
Fe X	λ174	"	**1.00 MK**
C IV	λ1550	**37Å**	**0.10 MK**
C I	λ1600	245Å	chromospheric
Fe II	"	"	chromospheric
Si II	"	"	**chromospheric**

Table 4.1: The TRACE bands recorded on 1999 June 4, with the ions emitting in each band. The primary lines are in bold face.

The wavelength bands observed in this program are listed in table 4.1, with the most important ions and lines in each band (the main line, assuming LTE, in bold face), the band center, bandwidth and the temperature of maximum formation for the listed ion. The event is most visible in the two first bands, it is very weak (although not completely invisible) in the broad λ1600 band.

4.2 Image Corrections

Image correction on the data was performed by Bart de Pontieu (pers. comm.). The images received were corrected for dark current and cosmic ray hits by a median-filter algorithm. The cleaning process is described in Bentley, R. D. (Ed.) (2001). C IV observations by TRACE require special treatment of continuum emission, as described by Handy et al. (1998). One of their results is that it is possible to extract the C IV emission from the continuum when the λ1550 intensity exceeds 10^{18} photons/s/m^2/sr.

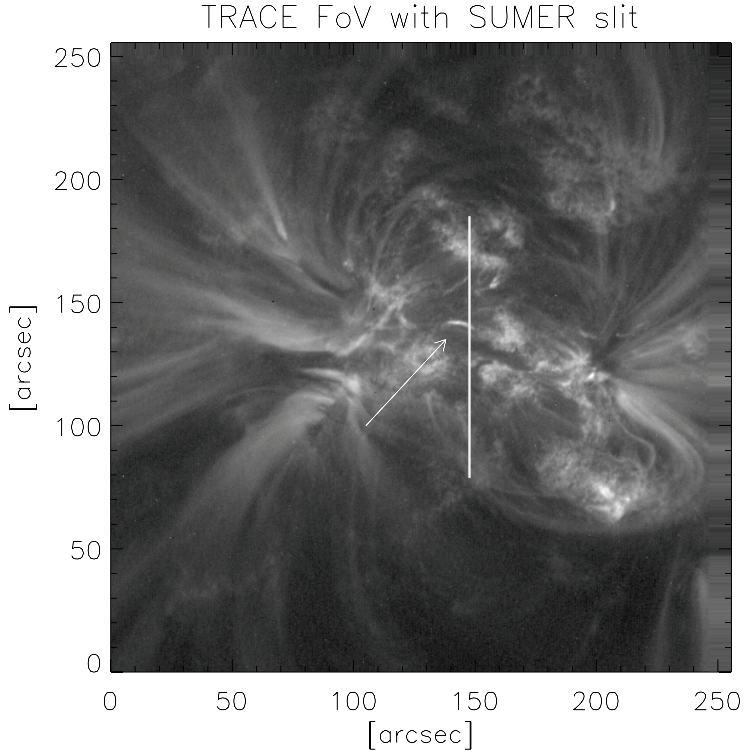

Figure 4.2.1: The full TRACE field of view with the SUMER slit interposed, showing the loop at its most intense, practically in the middle of the field. (This is the same image as in figure 3.2.1)

4.2.1 Alignment of SUMER and TRACE Images

We will first look at the time development along the same surface area as was covered by the SUMER slit. This requires a good alignment of the data sets.

Alignment was done in three steps: first the two sets were synchronized in time by mapping the ∼40 second cadence TRACE images to the 240 ∼28 second SUMER intervals using nearest neighbour sampling.

Then the TRACE images were coaligned to the SUMER view by correcting for the difference in how the two instruments tracks its objective. Each TRACE image was shifted by an appropriate number of pixels to achieve perfect coaligment, the effect of this is seen at the far right side of image 4.2.1.

With these two fundamental steps performed, the remaining step is to actually locate the features seen by SUMER in the TRACE images. The telescopes' (especially SUMER's) built–in absolute tracking is weak, so this was done mostly by hand. In this case an abundance of features common to the two data sets allowed a fine adjustment by visually comparing the two data sets (in more difficult cases image enhancing techniques such as the á trous algorithm described in De Pontieu et al. (1999) (references Starck et al. 1998) can be used to bring out edges, and make it easier to discriminate features). Regardless of the method used to align the data, we have to be aware that the same solar feature may be emitting at different altitudes in different wavelength bands, and take care to avoid parallax errors.

All the adjustments were done by Bart de Pontieu of the Lockheed Martin SAL team. Image 4.2.1 shows the position of the slit over the AR. The corresponding pixels in the processed TRACE images are: longitudinal pixel #295 and latitudinal pixels #370 to #158. The images are orientated so that north is up.

4.3 Spatial Features in the TRACE Data

With a proper alignment and synchronization between the SUMER and TRACE data sets in place, we can compare the trends observed by the two telescopes.

A zoomed–in view of the loop and the area around it is displayed at three selected times in figure 4.3.1. The first panel shows image #200, taken at 10:49:41, far away from the event in time. It shows how dark the loop is, especially after the event. It has some periods of stronger emission prior to the event, but all of these are much weaker than panel b) and c) of the same figure.

The first of these, panel c), was taken at 10:09:04 (image #112) and shows the loop after the onset of the event, but before the two bright bursts heralding its end. The first of these peaks, panel c), occured at 10:10:28 (image #115). Notice how much stronger the coronal part of the loop has become, only 1.5 minutes later.

The first thing we notice when we look at the panels of figure 4.3.2 is how fast the brightening spreads through the loop. At 10:09:04[3] the loop is all but invisible. Then, at 10:10:00, and again at 10:11:52, it suddenly lights up enough to rival even the brightest patches of moss in the AR.

The double peak marking the end of the event is the most obvious feature in those images. We can also see that the emission is stronger in the left half of the loop, the side not covered by the SUMER slit. In the same region, semi–regular brightenings can be seen for some time before the event, starting around 09:30, and ceasing together with the final bright peak. Some sporadic activity occur in the final hour of observations too, eg. the small brightening seen growing from the right foot and up at ca. 10:45.

In the X–T plots several thin (1-2 pixel wide) dips in intensity can be seen, spanning the full time interval. These are image artifacts introduced

---

[3] These are times fitted by closest neighbour–sampling to that of the closest SUMER spectrogram.

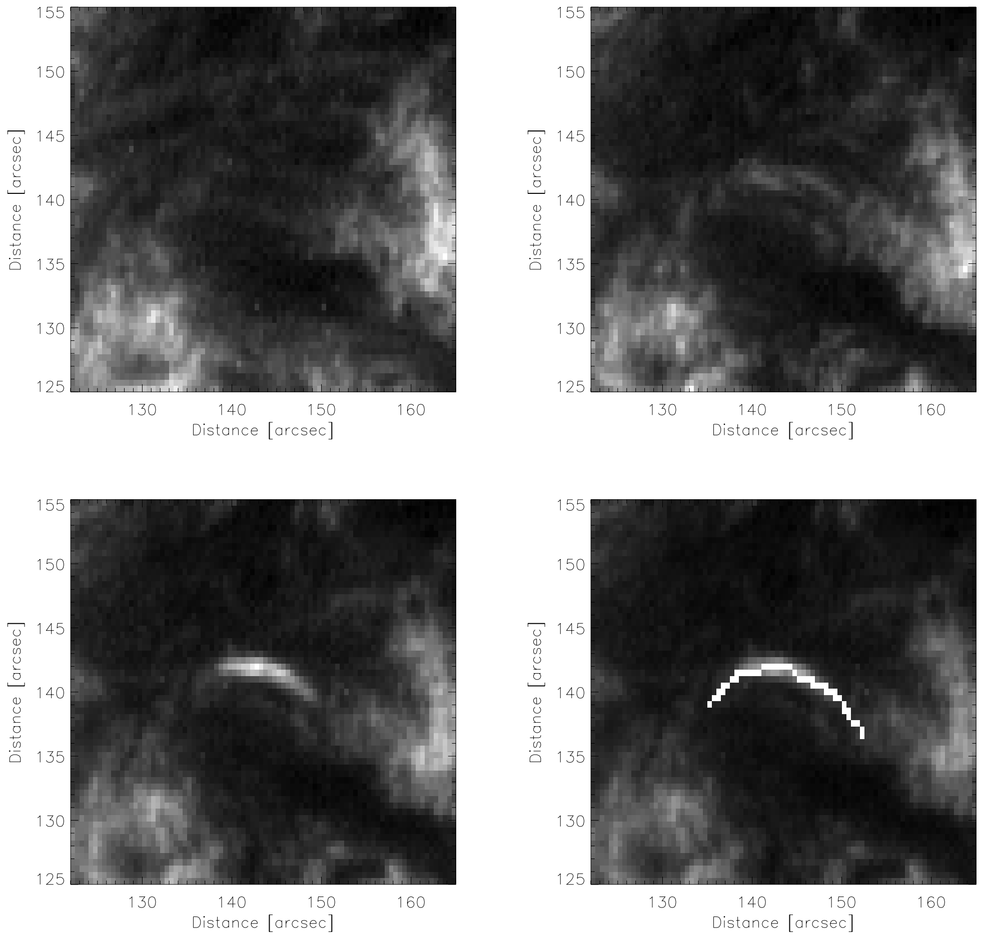

Figure 4.3.1: TRACE λ171–band images showing the loop at a quiet time (a), at the non–peaking part of the event (b), at its strongest (c). The final panel (d) shows the loop centroid used to fit the X–T diagrams presented below.

by the variation in filling factor in the pixels selected as the loop centroid, cf. image 4.3.1 d).

Just how strong the temporal connection between the emission from the left and right loop legs are is seen in figure 4.3.3 — the first peak is in fact completely synchronous in the two halves. Interestingly, at the second peak the two halves are completely out of phase, with the peaking in the left TR coinciding with the trough between the peaks in the right TR. The delay is at this point two exposures, capping the time delay at 80 seconds. With a typical coronal sound velocity u_S of 100km/s and hence total sound traversal time of 4 minutes for a 25Mm loop, a purely internal event must travel with

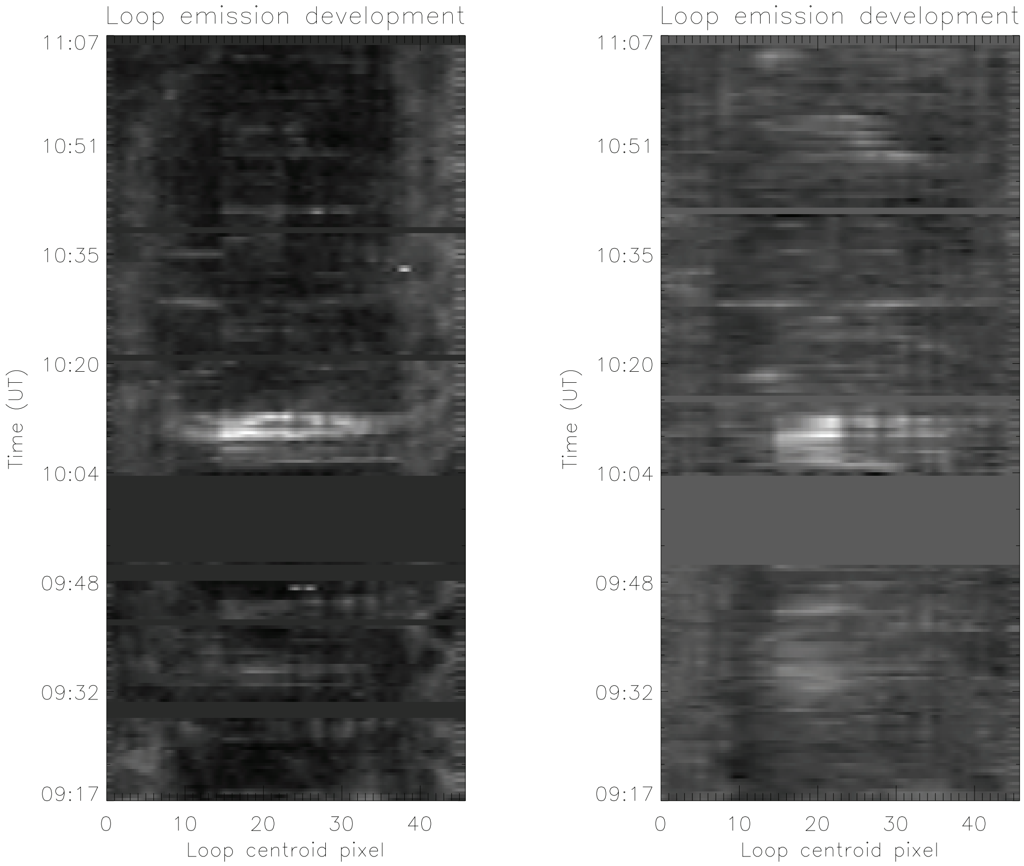

Figure 4.3.2: Intensity development in the TRACE λ171–band (left) and C IV band (right).

a speed of at least $3u_S$, a quite strong shock.

The graphs are normalized, the difference in absolute intensities in the two loop sections is somewhat larger than indicated here.

In the SUMER X-T diagrams, we notice some activity south of the loop discussed. The TRACE λ171 images reveal that it has a neighbour, seen clearly in the contrast–enhanced image 4.3.4. It is possible that more, unresolved, loops exists in the same area.

4.3.1 Loop Geometry

The footpoints of the loop cannot be clearly discerned because they do not appear as sufficiently bright features in any of our images. Under the assumption that the loop is perfectly semi–circular we can extrapolate the visible portion of it. The distance is then found to be between 35 and 40

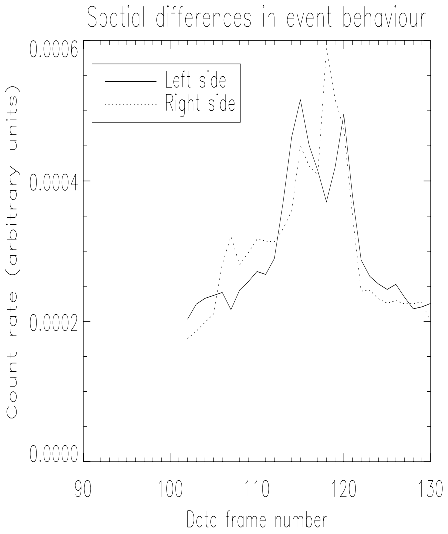

Figure 4.3.3: Intensity differences between the left and right loop halves. The graphs are not to scale.

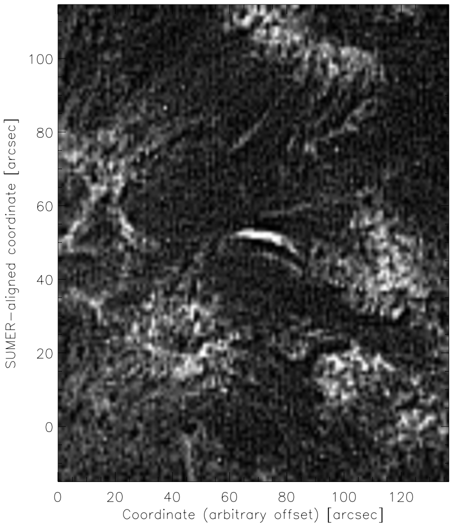

Figure 4.3.4: View of the neighbouring loop, the image is a sharpened version of TRACE λ171–band frame number 114.

pixels, corresponding to a loop length of 20–23Mm.

Using the same extrapolation we find that the loop is inclined about 20° away from the normal. This is reasonably close to the inclination between us and the AR, which means that the loop has no effectively no inclination with respect to the solar surface.

Because of the lack of visible markers, it is hard to say anything concrete about the loops morphological development too, but it is at least clear that it does not change during the event, which is the matter of most importance here. The "trenches" noted in the X–T diagrams (especially the right panel of figure 4.3.2) also point to a constant loop geometry.

The loop thickness is on the very border of the instrument's resolution. At the apex it spans a width of 5 pixels, indicating a width of about $1''$, or $\sim$1Mm. Any variations in loop cross section with distance cannot be found, both because it is so close to the resolution limit, and because it is so dark at the footpoints. In this case there are few prior results to lean on, but those few that exist point to a low expansion factor $q_w = w_{\rm top}/w_{\rm foot} \sim 1.2$ (Watko and Klimchuk 2000 for postflare loops).

4.3.2 Magnetic Field Strength and Orientation

The magnetic field variation in the area of the loop is as we would expect, with foot field strengths on the order of 1mT. For of completeness I include

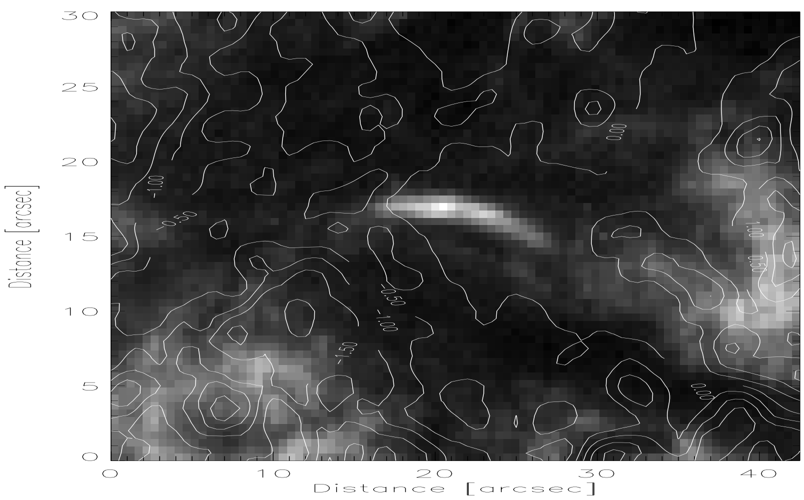

Figure 4.3.5: MDI magnetogram observation as contour lines on a TRACE $\lambda171$–band background. The contour labels are in units of kG (100mT).

a magnetogram from MDI[4] in figure 4.3.5, shown as a contour plot on top of a TRACE $\lambda171$–band image, taken near $t = 10{:}11$.

Emission bursts like this one is commonly thought to be associated with magnetic reconnection. Unfortunately, with the (for this purpose) limited resolution ($1''$) and cadence (1 minute) of MDI it is not possible to verify or rule out that such an event is the cause behind the emission in this specific case. The high–strength regions in the left and right edges of the image are sunspots, clearly seen in Hα images (not shown).

4.4 Temporal development along the SUMER slit

In the previous chapter I presented X–T diagrams of the intensity development along the slit. In figure 4.4.1–2 below I present similar diagrams, with the rows covering the same area as the SUMER slit.

The $\lambda1600$ broadband responded weakly to the transient brightening and with the same trends as C IV[5], so I left it out of the analysis.

Unfortunately there was no telemetry of the $\lambda171$ and C IV observations during the quarter of an hour preceding the event, making it difficult to determine exactly when the brightening starts in the TRACE data. The first

---

[4] The Michelson Doppler Interferometer observes the solar magnetic field through Zeeman splitting of the Ni I $\lambda6768$ line. It is flown on the SoHO instrument platform.

[5] The small correlation caused can be caused by C IV $\lambda1548$ itself, as the $\lambda1600$ band covers this wavelength.

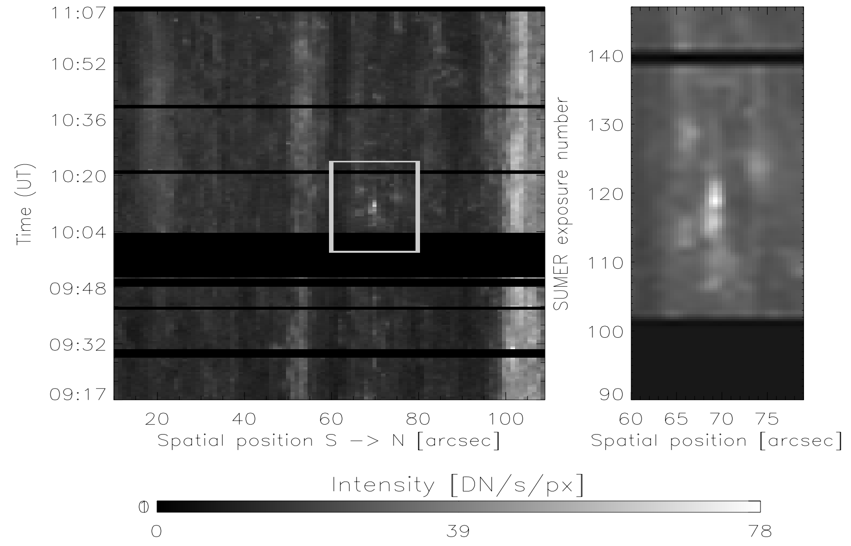

Figure 4.4.1: The intensity development under the slit pictured in figure 4.2.1, with a detailed view around the event. This is the $\lambda171$ band, with the times and exposure numbers fitted to the closes ones in the SUMER data set.

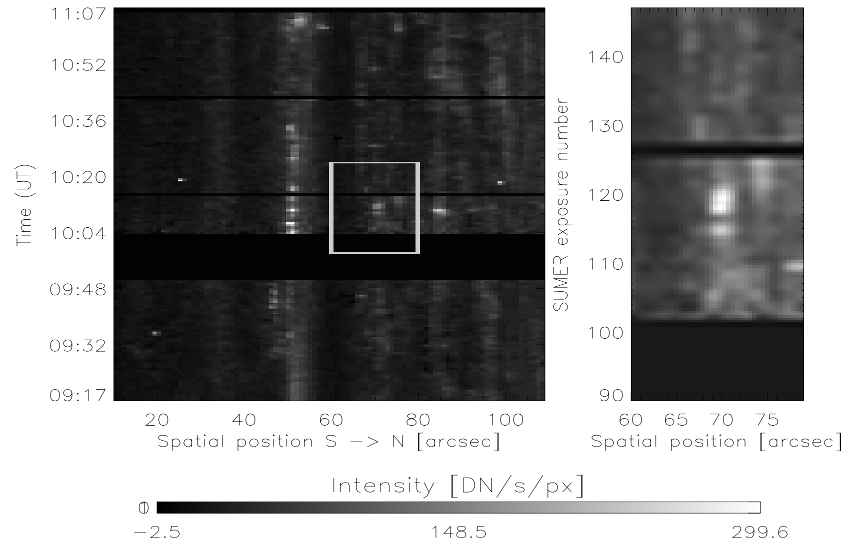

Figure 4.4.2: The intensity development under the slit pictured in figure 4.2.1, with a detailed view around the event. This is the C IV ($\lambda1550$ band), with the times and exposure numbers fitted to the closes ones in the SUMER data set.

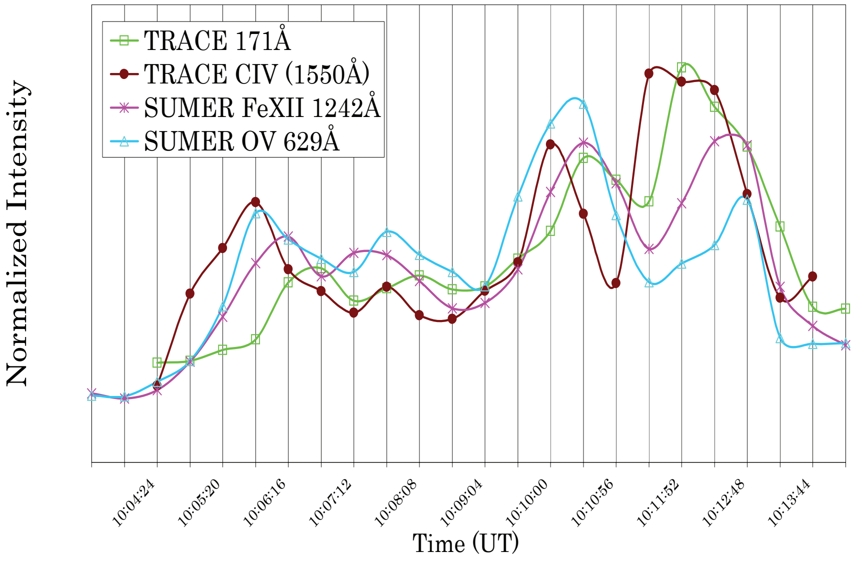

Figure 4.4.3: Intensity progress during the event in four selected bands. The lines drawn through the sets of points are splined to make each band's points easier to make out.

available TRACE frame is the one taken at the same time as the brightening begins in the SUMER data. The emission in TRACE C IV follows the same trend as all the low–temperature SUMER lines, I therefore assume that the event starts with the first available TRACE C IV frame, at 10:03:56 (frame #101). The $\lambda171$ band stays calm for at least half a minute longer, with an onset at 10:04:24 (frame #103).

Onset Times

The trends of both TRACE bands, plotted with two selected SUMER bands are drawn in figure 4.4.3. The SUMER bands Fe XII and O VI were selected on the grounds that they should provide the strongest link with the TRACE data. In particular, the TRACE $\lambda171$–band responds exclusively to ions of oxygen and iron at our temperatures.

The most distinctive feature is that they all share the general characteristics of an initial peak at 10:05:48, followed by a plateau that lasts for half the event. The event ends with two strong and sharp peaks, at 10:10:00 and 10:11:52, in every band. This is precisely the behaviour we saw in the SUMER bands. The intensity has settled down to the background level at 10:15, and remains calm up to the end of the observation.

Phase Differences

There is a phase difference between λ171 and C IV. In all three of the peaks, λ171 lags about 30 seconds. For these two lines, the phase difference is congruous with what we expect to see from rapidly heated, initially cold, plasma. At first, neither atom is ionized into the states emitting in our bands. Ionizing at a lower temperature, carbon is the first to reach a numerical density high enough to be visible to TRACE. As the temperature grows even higher, it reaches a level favourable for O VI, and later Fe IX–XI, but now all the C IV above the footpoints has ionized into C V, and the light in the TRACE C IV band fades. Because the SUMER slit is placed where it is looking down through the loop TR near a footpoint, seeing a range of depths, no band goes completely dark at any time.

This train of thought is derailed by the graph describing Fe XII though, which by the same reasoning should light up last. Obviously more than rapid heating of a stationary plasma is at work here.

Cross Correlations

A more quantitative measure of how well the curves follow each other is the cross correlation. Table 4.2 shows these for most of the observed bands. All of them are necessarily high, as the bands selected are precisely those which show the transient event. More information is thus found by looking for bands with low correlation coefficients.

One of these is between O V and TRACE λ171–band, caused by a general lag of a few frames between each feature, in particular in the final five frames. A possible explanation for the missing correlation is that the ion seen by TRACE in this band is actually O VI, not Fe IX–XI as we usually expect[6]. In this case the ionization into O VI would feed of the emitting O V ions, and vice versa.

	O V	Mg X	Si II	TR λ171	C IV	N V λ1238
Fe XII	0.85	0.86	0.88	0.84	0.65	0.96
O V		0.89	0.83	0.49	0.41	0.77
Mg X			0.90	0.69	0.60	0.86
Si II				0.76	0.77	0.88
TR λ171					0.71	0.89
C IV						0.77

Table 4.2: Correlation coefficients between the well–defined bands observed by TRACE and SUMER.

C IV is poorly correlated with every one of the other lines, especially O V. The reason for this remains to be determined, but one source of disagreement

---

[6] The properties of the TRACE λ171–band filter are discussed in chapter 8.1.

is that the TRACE data is taken with higher cadence and interpolated to the SUMER time steps, with loss of some higher frequency variations. This reasoning applies to λ171 as well as C IV.

4.5 Summary of the TRACE Data

The main findings in this chapter can be repeated in a bulleted list:

- The TRACE data follows the same time profile as the SUMER data did, possibly with a slight phase difference between the cold C IV band and the hot λ171 band. This is made less certain by the loss of telemetry during the 15 minutes prior to the event.

- The emission is simultaneously increasing throughout the whole loop, making an external energy source a likely cause of the heating.

- TRACE λ171–band emission could be caused by O VI rather than Fe IX/X, a claim elaborated on in chapter 8.

- Loop emission intensity is low throughout the observation, except during the flashes.

- Although the loop is only one of at least two in the small region, the presence of several loop strands does not seem to be related to the event.

- There are no discernible morphological development in the loop during this observation, and clearly none during the event.

- The loop is between 20Mm and 25Mm long, with a maximum width of about 1Mm.

4.6 Discussion of the Observational Data

Between the two instruments, we should be able to draw some conclusions about the loop plasma and the transient event.

All the bands (N V, O V, Mg X, Fe XII, Si II, C IV and Fe IX/X) display the same characteristic profile, with an initial brightening, followed by a plateau lasting about 6 minutes, and ended by two sharp peaks of very strong emission, each with a period of some 2 minutes. As far as it is possible to discriminate between the bands, the cold C IV data appears to be affected first, and the hotter Fe IX/X band last, with the delay between them 1.5 minutes. The hottest band of Fe XII, however, is affected only 30 seconds after C IV, confounding a simple relation between the onset time and ionization temperature.

Line width analysis of SUMER data points to widely divergent results, with the most probable temperatures at $1-2\times10^5$K. The temperature range spanned by the two TRACE bands are $\sim10^5$K (C IV) and $0.3-2.5\times10^6$K (λ171), leaving a "dead spot" in the temperature range $1-3\times10^5$K. The loop is indeed invisible to TRACE, except during the event, which supports the idea of a plasma temperature near 2×10^5K. If this reasoning is correct, the coronal part of the loop is nearly isothermal; with a slight positive gradient. All the line profiles widen sharply during the event.

The SUMER slit observes the right foot of the loop, near where we expect to find the interface between the lower corona and transition region. Line shifts in the O V λ629 and N V λ1238 show that there is a downflow of plasma (ie. red–shift) in that part of the loop. This flow starts to grow about 15 minutes before the onset of the event, reaches its highest velocity during it, and decays back to a stationary level over another 15 minutes. Two waves travelling upwards interrupt this calm picture, the first occuring just after the initial peak in emission, and the second just after the final peak.

Chapter 5

The Advection Engine

The numerical analysis tool in use, TTRANZ, is an implicit finite difference engine. The conservation equations of mass, moentum, energy and particles are solved by advecting discretized quantities on a staggered grid, with adaptive cell spacings and time steps as per Dorfi and Drury (1987), advanced implicitly in time through the second order upwind scheme of van Leer (1977). A description of the program and its use is written by the program's author, Hansteen (1991).

5.1 Discretization

The governing equations are discretized onto a staggered grid, where the velocities are defined on cell boundaries, and scalars such as the density and energy are defined in the cell centers. These variables are then decoupled, and we avoid the numerical oscillations that plague unstaggered grids. The penalty is that we have to use two distinct sets of indices to reference the variables on the mesh, ie. we must "move" the scalar quantities to the cell boundaries before we can perform calculations. Cell boundaries are indexed as natural numbers, usually symbolized with i, $1 \leq i \leq N$, with N the total number of cells, and the centers are considered half a cell away, so that $i+1/2$ is between boundaries i and $i+1$, for $1 \leq i \leq N-1$. Thus $u_i \equiv u(z_i)$, while $\rho_{j+1/2} \equiv \rho[s(z_{i+1}, z_i)]$, and the interpolation $s(z_{i+1}, z_i)$ must be designed so that the advected quantity $w = \langle u\rho \rangle$ meets the monotonicity requirement of

$$0 \leq -\frac{w_i^{\mathrm{n}} - w_i^{\mathrm{o}}}{w_i^{\mathrm{o}} - w_{i-1}^{\mathrm{o}}} \leq 1. \tag{5.1}$$

By ensuring monotonicity, we avoid spurious oscillations in regions where cell values change rapidly — something that is of particular importance in schemes dealing with sharp gradients such as shock fronts.

Time steps are labelled with superscripts, usually an "o" (old) for the current and "n" (new) for the next time steps, as in $\rho^{\mathrm{n}} \approx \rho^{\mathrm{o}} + \Delta t \, (\mathrm{d}\rho^{\mathrm{o}} / \mathrm{d}t)$.

5.2 Upwind Differencing

The advected quantities are discretized through the second order upwind scheme of van Leer (1977). The core idea in an upwind scheme is to choose which cells to involve in a calculation by looking at the direction the advected quantity is moving, and then base our calculations on the plasma state upwind from us. As an example, the continuity equation (eq. 2.33) is discretized as presented by Hansteen (2005):

$$(\rho^{\mathrm{n}}_{i+\frac{1}{2}} - \rho^{\mathrm{o}}_{i+\frac{1}{2}})\,\mathrm{d}z + (\langle u\rho\rangle_{i+1} - \langle u\rho\rangle_i)\,\mathrm{d}t \quad = \quad 0 \tag{5.2}$$

(this conservative form is quite general). The upwind approach to the problem is through the averages $\langle u\rho\rangle_{i,i+1}$. We estimate the flux at the next time step by following a characteristic

$$\rho^{\mathrm{n}}_i \quad = \quad \rho(t^{\mathrm{o}},\, z_i - s\,\mathrm{d}z), \tag{5.3}$$

where

$$s \quad = \quad u\frac{\mathrm{d}t}{\mathrm{d}z}. \tag{5.4}$$

The density, defined in the cell centers, is approximated at the cell boundary through a Taylor expansion,

$$\langle u\rho\rangle_i \quad = \quad u[\rho^{\mathrm{o}}_{i-\frac{1}{2}} + \frac{1}{2}(1-s)\,\mathrm{d}\rho_{i-\frac{1}{2}}], \tag{5.5}$$

with which the flux approximation then becomes

$$\begin{aligned}\langle u\rho\rangle_i \quad &= \quad \frac{1}{2}\,u\left[\rho_{i-\frac{1}{2}} + \left(\frac{1}{2}\,\mathrm{d}z - s\,\mathrm{d}z\right)\frac{\mathrm{d}\rho}{\mathrm{d}z} + \rho_{i-\frac{1}{2}} + \frac{1}{2}\,\mathrm{d}z\frac{\mathrm{d}\rho}{\mathrm{d}z}\right] &\quad (5.6)\\ &= \quad u\left[\rho_{i-\frac{1}{2}} + \frac{1}{2}(1-s)\,\mathrm{d}_{i-\frac{1}{2}}\rho\right]. &\quad (5.7)\end{aligned}$$

The definition of the differential $\mathrm{d}_{i-\frac{1}{2}}\rho$ is important to the final accuracy of this algorithm. A second order method is

$$\mathrm{d}_{i-\frac{1}{2}}\rho \quad = \quad \frac{(\rho_{i+1}-\rho_i)(\rho_i-\rho_{i-1})}{(\rho_{i+1}-\rho_{i-1})\Delta z}. \tag{5.8}$$

Now the elements from the array thus defined are selected literally as the wind blows, giving a second order upwind scheme. When $u_i > 0$ in the cell i we are currently advecting, we look at computed temporary values with indices relative to $i-1$, otherwise we use the current offset i also for the temporary values.

5.3 The Adaptive Grid

5.3.1 Spatial Resolution Changes

The grid subsystem uses the design of Dorfi and Drury (1987) to focus computational resources on sections with high rates of change by changing the cell spacings $z_{i+1} - z_i$ and the time steps Δt, with the intention of keeping the gradients between neightbouring cells small. It is achieved by choosing a desired resolution R_i as

$$R_i = \left[1 + \sum_{j=1}^{M} \left(n_i \frac{f_{j,i+1} - f_{j,i}}{F_j} \right)^2 \right]^{1/2}. \tag{5.9}$$

The F_j are weights for each of the M functions f_j representing variables of particular interest, like T_e and u, and decides how much a gradient in f_j will influence the desired resolution. n_i is the actual grid resolution,

$$n_i = \frac{Z_i}{z_{i+1} - z_i}. \tag{5.10}$$

Z_i determines a practical length scale for the proplem, on the order of 10^3km in the case of coronal loops. The simulation can thus be optimized for a given scenario through appropriate choices of F_j and Z_i[1].

In TTRANZ the variables f_j used for grid control are the density, electron number density, velocity and temperature.

5.3.2 Temporal Resolution Changes

Similarly, we want to ensure that the time rate of change for any quantity is bounded by a problem–dependent factor. This is done by introducing a variable τ as an analogue to Z_i, which is used, together with the courant condition at the boundaries, to calculate a new time step length before each iteration.

5.4 Implicit Solution Scheme

Steps in time are done with *implicit* code, all advances are done on an weighted average of the current (known) values and the unknown values at the next time step. This makes it necessary to solve a set of non–linear equations, which we do by iteratively solving linearized versions of them by the Newton-Raphson method presented in sect. 5.5. With θ the weight (not related to the plasma θ), the working variable is

$$D^{\mathrm{w}} = \theta D^{\mathrm{n}} + (1 - \theta) D^{\mathrm{o}}. \tag{5.11}$$

---

[1] Dorfi and Drury (1987) do note that the rate of change of the grid should not exceed 30%, this is controlled through a rigidity factor α defined through $\frac{\alpha}{\alpha+1} \leq \frac{n_{i+1}}{n_i} \leq \frac{\alpha+1}{\alpha}$.

All simulations in this thesis were carried out semi–implicit, with θ set to 0.55.

5.5 The Newton-Raphson Iteration Method

The calculation of new plasma parameter at each time step is handled by a multidimensional version of the Newton-Raphson Iteration Method. Press et al. (2002) describe this method in a clear way, I just include a paraphrase of their work here for reference.

Generally we want to find the value of N variables $(x_0, x_1, \ldots, x_{N-1}) = \mathbf{x}$, as constrained by the vector of N equations $(f_0, f_1, \ldots, f_{N-1}) = \mathbf{f}$. In our specific case, the equations in $\mathbf{f}$ are the conservation equations and so forth, while the elements of $\mathbf{x}$ are state variables like ρ and T_e.

Each function f_i in $\mathbf{f}$ can be expanded as a Taylor series around $\mathbf{x}$,

$$f_j(\mathbf{x} + \delta\mathbf{x}) \quad = \quad f_j(\mathbf{x}) + \sum_{i=0}^{N-1} J_{ij}\, \delta x_i + \mathrm{O}(\delta\mathbf{x}^2), \tag{5.12}$$

where

$$J_{ij} \quad = \quad \frac{\partial f_i}{\partial x_j} \tag{5.13}$$

is $\mathbf{f}$'s Jacobian. Denote the variables at the current and next step in time as $\mathbf{x}^\mathrm{o}$ and $\mathbf{x}^\mathrm{n}$ with the relation $\mathbf{x}^\mathrm{n} = \mathbf{x}^\mathrm{o} + \delta\mathbf{x}$, and let every function $f_j \in \mathbf{f}$ be on the form $f_j(\mathbf{x}) = \mathbf{0}$. By setting each $f_i(\mathbf{x}^\mathrm{n}) = 0$ and ignoring the higher order terms, we can write the system of equations on matrix form as

$$\mathbf{f}(\mathbf{x}^\mathrm{n}) = \mathbf{f}(\mathbf{x}^\mathrm{o}) + \mathbf{J} \cdot \delta\mathbf{x} = 0, \tag{5.14}$$

We can solve this system for $\delta\mathbf{x}$ by inverting $\mathbf{J}$,

$$\delta\mathbf{x} \quad = \quad -\mathbf{J}^{-1}\mathbf{f}(\mathbf{x}^\mathrm{o}). \tag{5.15}$$

A solution of desired accuracy is then obtained by the iterative application of this method until the difference $\delta\mathbf{x}$ reaches a predetermined level (eg. the machine precision).

The convergence of Newton's method is quadratic, which means that an error of magnitude $\epsilon < 1$ in one step is reduced to ϵ^2 in the next. This makes for very fast convergence. This is, of course, if it actually converges at all. If the initial guess is too far from the solution, it might never do, and in this case we have to restart the iterative procedure with a different (and hopefully better) guess.

5.5.1 Discretized Equations

The equations we discretize and solve at each time step are the advection equations (continuity, momentum and energy) described in section 2.4, along with the rate equation of section 2.2 applied to hydrogen and helium, the equation of charge conservation (similar to the continuity equation) and the grid equation described above.

When convergence is achieved for these equations, the rate equations for the metals of interest (ie. carbon, nitrogen, oxygen and iron) are solved. The resulting radiation loss is then applied to the equation of energy conservation at the next iteration. This decoupling of the rate equations for the metals keeps the solution matrix small without sacrificing precision in the physics.

Chapter 6

Designing the Atomic Models

Several databases detailing atomic behaviour have been assembled, and of these the CHIANTI SolarSoft package is particularly useful. It contains data and software focused on solar atmospheric plasmas, and is continually updated. Here I update the original HAO DIAPER data in TTRANZ with the newer or alternative results, and add some missing features. In cases where both data sets have holes, I supply with values from the NIST online database. I then run simulations with both data sets. The intention is to reveal any difference in end results stemming differences in atomic data.

6.1 Comparison of Available Data

As described in section 2.3, in the coronal equilibrium model we approximate the intensity I_λ of a given emission line $\lambda_{u,\ell}$ from an m times ionized atom X (denoted X^{+m}) as

$$I_\lambda \;=\; \left(\frac{hc}{4\pi\lambda_{u,\ell}}\right)\left(\frac{N(X^{+m})}{N(X)}\right)\left(\frac{N(X)}{n_{\mathrm{H}}}\right) n_{\mathrm{H}}\, C^{\mathrm{ex}}_{u,\ell}\, n_{\mathrm{e}}\, B_{u,\ell}. \qquad (6.1)$$

With the exceptions of the densities (which are determined by the temperature and boundary conditions), all terms of equation 6.1 have to be provided in an atomic model.

The fraction of the atom X ionized exactly m times relative to all the available ionization degrees,

$$\frac{N(X^{+m})}{N(X)},$$

is determined in part by the atomic data used in calculations of ionization rates. The third fraction in equation 6.1 is the abundance, the number of atoms of species X relative to the number of protons. The final two terms are the excitation rate coefficient ($C^{\mathrm{ex}}_{\ell,u}$) into the emitting ionic state, and a branching fraction ($B_{u,\ell}$) specifying the fraction of excited ions that will decay into the lower state, producing a photon with the desired wavelength.

I will here critically review the available data for each of these parameters, and design appropriate atomic models that will faithfully reproduce spectra in our desired wavelength bands, primarily the TRACE λ171–band.

6.1.1 The Data Sources

Three sources of atomic data have been chosen for review: the CHIANTI (Dere et al. 1997, Landi et al. 2006) database, which is designed precisely for the study of optically thin emission spectra; the NIST online database (Ralchenko et al. 2005); and the models included in the HAO DIAPER (Judge et al. 1998) library. These databases take their values from a list of sources too long to reproduce here, except when they are specifically mentioned.

6.1.2 The Atomic Model File Structure

The atomic models used by TTRANZ are defined by a text file structure designed by M. Carlsson for the MULTI numerical analysis engine. Each file, containing one atom, starts with a header consisting of the element name and some general information. The header is followed by four blocks, each detailing information about one aspect of the population–determining processes:

— energy levels and configurations (section 6.1.4),
— lines and continuum emission (section 6.1.5),
— exitation processes (section 6.1.6) and
— ionization processes (section 6.1.7).

Lines with a "*" character in column one are comments for readers' convenience, they are discarded by the computer.

6.1.3 Element Abundances

The emission has a direct dependence on the abundances, which are the first values listed in the MULTI files. We use the logarithmic "dex" scale where $\mathrm{Ab_H} \equiv 12$, so that element "X" has a dex value given by

$$\frac{N(X)}{n_{\mathrm{H}}} = 10^{\mathrm{Ab_X} - 12}. \tag{6.2}$$

Proper coronal values for this parameter is still an area of much research, and several relatively recent models are available for consideration. Results do however seem to converge towards the *hybrid* set described by Fludra and Schmelz (1999), who use the name to indicate that it takes into account that the corona shows a relative (to the photosphere[1]) lack of elements with

---

[1] The process that separates high and low FIP elements take place in the chromosphere, at $6 - 10 \times 10^3$K.

high first ionization potential (FIP) — it is a hybrid between photospheric and earlier reports on coronal abundances. Their results differ from the DIAPER values for all elements; and because of the focus on low FIP elements, particularly so for helium.

```
* Atom ferrum, written by atomwr on Tue, Feb. 5 2002, updated
* with CHIANTI values on Mon, Oct. 31 2005.
*
fe rrum
*            ab [dex]       mass [mu]         atom (Z)
               7.83           55.85             26
```

Listing 6.1: The header of the MULTI file for iron, detailing atomic abundance, mass in amu and atomic number (Z).

I tabulate three candidate abundances below for easy comparison — the original DIAPER data, the hybrid set and Grevesse and Sauval (1998)'s values for the photosphere. Also included in the table are the FIP of each element, as an indication of where we should expect large FIP–predicated differences. I updated the abundances for all elements to those in the "hybrid" data set.

Atom	FIP [eV]	DIAPER	Hybrid	Photospheric
He	24.6	11.0	10.8	10.93
C	11.3	8.60	8.41	8.52
O	13.6	8.82	8.74	8.83
Ne	21.6	8.08†	7.95	8.08
Mg	7.64	7.58	7.90	7.58
Si	8.15	7.55	7.87	7.55
Fe	7.90	7.60	7.83	7.50

† Neon is listed in the data file as $N_{\mathrm{Ne}}/N_{\mathrm{H}}$.

Table 6.1: Listing and comparison of element abundances from DIAPER, Fludra and Schmelz (1999) and Grevesse and Sauval (1998).

The elements oxygen and iron are important contributors to the emission in the TRACE λ171–band. The emission is linear in the abundance, so as I chose Fludra and Schmelz (1999) over DIAPER data we should anticipate a reduction of 79.8% near 3×10^5K where O VI dominates, and an increase of 141% around 10^6K from iron.

Atomic masses do influence line broadening (eq. 2.21), but too weakly to have any bearing on the present study. I therefore use the accepted terrestrial values. See eg. Yurimoto and Kuramoto (2004) for a recent discussion of oxygen isotopes.

6.1.4 Energy Levels

The intensity depends directly on the energy difference between the upper and lower levels in two ways. Firstly, in the direct relation

$$\lambda_{u,\ell} = \frac{hc}{E_u - E_\ell} \tag{6.3}$$

where inaccurate values could conceivably have an impact where energies have corresponding wavelengths in the TRACE EUV regime, as the response of its detector depends strongly on the wavelength. Secondly, $\Delta E_{u,\ell} = E_u - E_\ell$ enters the intensity through the calculation of the collisional exitation rates $C^{\mathrm{ex}}_{g,u}$, described in detail below.

In reality the alternative values here are all close enough to preclude any such effect, and I arbitrarily pick the DIAPER values.

The levels are listed in the atomic files one at a line.

```
* # levels      # Transitions      # Continuum      # Fix
      27             20                 0              0
*
*  Energy [/cm]    Weight     Ions and terms             Ion
        0.000       1.00      'fe vii 4s2 1se 0'           7
  1008184.600       2.00      'fe viii 4s 2se 1/2'         8
  2226555.500       1.00      'fe ix 3p6 1se 0'            9
  2811101.500       3.00      'fe ix 3p5 3d 1po 1'         9
  [... followed by 23 more levels.]
```

Listing 6.2: Energies of ions and levels available in the atomic model.

Level terms and statistical weights are also listed in this section, but they are not used by TTRANZ, only by the HAO DIAPER package, which uses them, among other things, to draw Grotrian diagrams.

Which lines (and thus levels) we need to synthesize spectra with TRACE is discussed in section 6.2.

6.1.5 Radiative Relaxation Rates

In most cases the only way for an electron to leave an excited state is through an allowed radiative relaxation, in which case the relaxation rate coefficient $A_{u,\ell}$ can vary a lot without influencing the number densities in the excited states — as long as the relaxation rate is much larger than the excitation rate.

Therefore this is also a part where the results will not vary depending on which database we take our values from. But there is another side to this story; the branching coefficient $B_{j,i}$ at the end of equation 6.1,

$$B_{u,\ell} = \frac{A_{u,\ell}}{\sum_{k<u} A_{u,k}}, \tag{6.4}$$

which tells us into which states the electrons actually relax. If a significant part of the electrons in state j end up in another exited state (not in the ground state g) than we assume, we will get a flawed picture of both the strength of the $\lambda_{u,l}$ line and any lines originating in the lower chains of the cascade. The bottom line of this is that we need to pay attention to the ratios of the coefficients within each ion even though their absolute values are relatively unimportant.

While there are differences in transition rates between CHIANTI and DIAPER in many cases[2], I assume that the databases are internally consistent, with differences between them rooted in experimental bias. Since TTRANZ calculates the Einstein coefficients from the oscillator strengths $f_{u,\ell}$ (they are linearly dependend, see chapter 2.2), and the CHIANTI database only contains generalized oscillator strengths ($gf_{u,\ell}$ values), I found it most convenient to keep the oscillator strenghts ($f_{u,\ell}$ values) in the DIAPER data, and supplement from Ralchenko et al. (2005) for the levels added in section 6.2.

They are entered into TTRANZ as shown here, along with a few control variables not shown.

```
 * upper    lower     osc. str.             Einstein A
     4        3       2.65e+00     [...]     2.09e+11      [...]
   [... and 19 more transitions.]
```

Listing 6.3: The emission lines available for a detailed radiation loss treatment by TTRANZ.

6.1.6 Collisional Excitation Rates

The expected number of ions in an excited state u is linear in the excitation coefficient $C^{\mathrm{ex}}_{g,u}$,

$$N_u(X^{+m}) \;\cong\; C^{\mathrm{ex}}_{g,u}\left(\frac{N(X^{+m})}{N(X)}\right)\left(\frac{N(X)}{n_\mathrm{H}}\right) n_\mathrm{H}\, n_\mathrm{e}. \tag{6.5}$$

This is thus the parameter in dispute that has the strongest effect on the final spectrum. Fortunately both CHIANTI and TTRANZ use thermally averaged collision strengths $\Upsilon_{\ell,u}$ to compute the collisional exitation rate coefficients, as detailed in equation 2.4:

$$C^{\mathrm{ex}}_{\ell,u} \;=\; 2\sqrt{\pi} a_0 \hbar m_e^{-1}\left(\frac{I_\infty}{k_B}\right)^{1/2} T_e^{-1/2}\,\frac{\Upsilon_{\ell,u}}{\omega_\ell}\,\mathrm{e}^{-\frac{E_{\ell,u}}{k_B T_e}}, \tag{6.6}$$

where ω_ℓ is the multiplicity of the lower level, and $I_\infty = 13.61\mathrm{eV}$. This makes it easy to compare their values. However, they do differ in how the values

---

[2] Eg. the O VI line $2\mathrm{p}^1\,{}^2\mathrm{P}_{3/2} \rightarrow 3\mathrm{d}^1\,{}^2\mathrm{D}_{5/2}$ for which the former database lists a rate a factor 10 higher than the latter.

are stored in the atomic models. While MULTI simply stores sufficient spline knots of $\Upsilon_{\ell,u}$ to compute the rates at all relevant temperatures, CHIANTI stores the five (in som cases nine) spline knots used in the scheme designed by Burgess and Tully (1992).

This scheme works as follows: Let

$$E_T = 6.3\times 10^{-6}\, T_e k_B/\Delta E_{\ell,u}, \tag{6.7}$$

and compute the corresponding x from

$$x = \begin{cases} \log\left[(E_T+C)/C\right]/\log\left(E_T+C\right) & \text{(allowed transitions)} \\ E_T/(E_T+C) & \text{(forbidden transitions),} \end{cases} \tag{6.8}$$

where the constant C is tabulated in CHIANTI. Interpolate this value to $y(x)$ using the 5-point spline, and scale it to get the $\Upsilon_{\ell,u}$:

$$\Upsilon_{u,\ell} = y\times \begin{cases} \log\left(E_T+e\right) & \text{(allowed transitions)} \\ 1 & \text{(forbidden transitions)} \end{cases} \tag{6.9}$$

Young's IDL function `RATE_COEFF` extracts the CHIANTI $\Upsilon_{l,u}$ values at the temperatures used of the MULTI spline knots. They are entered into MULTI–files on separate lines following the definition of the temperature spline knots like this:

```
* Temperature spline knots (5 indicates the number of knots):
temp
5   4.0e+03   7.5e+03   3.0e+04   7.5e+04   3.0e+05   7.5e+05
* Thermally averaged collision strengths.
ohm
3  4   2.86      2.85      2.87      2.91      3.14      3.50
```

Listing 6.4: Sample excitation coefficient Υ spline knots.

The original DIAPER coefficients are taken from Clark et al. (1982), while CHIANTI uses a wider range of sources, of which the most important in this case are Goett and Sampson (1983) for O VI, Storey et al. (2002) for Fe IX and Del Zanna et al. (2004) for Fe X.

The rate coefficients calculated using the first source differ in some cases considerably from those calculated using the latter three. The most conspicous case occurs with the O VI $\lambda\lambda 172.94, 173.10$ lines essential to this thesis: while the difference in Υs for the $^2\mathrm{P}_{3/2} \rightarrow {}^2\mathrm{D}_{3/2}$ transition is a mere 3.7%, those for the $^2\mathrm{P}_{3/2} \rightarrow {}^2\mathrm{D}_{5/2}$ transition differ by as much as 62%.

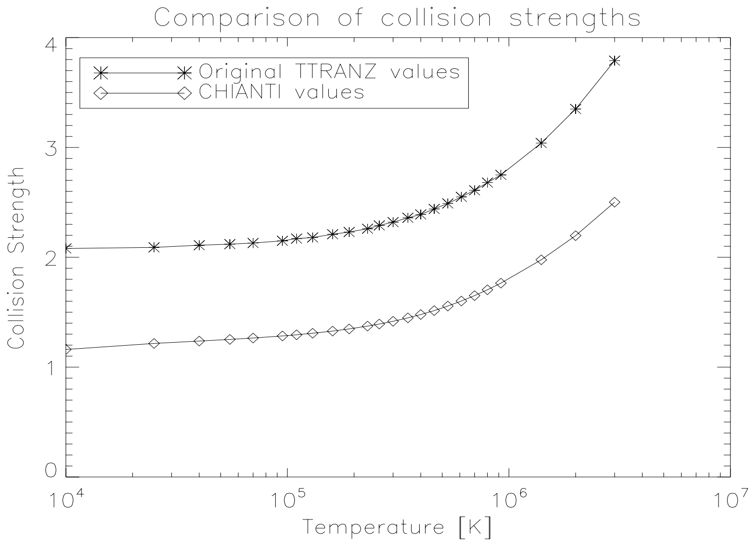

Figure 6.1.1: O VI $^2P_{3/2} \rightarrow {}^2D_{5/2}$ collision strengths. This is the (relevant) transition where the databases disagree the most.

I chose to use CHIANTI's coefficients $\Upsilon_{\ell,u}$ for all transitions. From this we should expect to see a marked change in the O VI emission of new spectra relative to those made with DIAPER data.

6.1.7 Ionization and Recombination

The fraction of the atom X that is ionized to the emitting stage X^{+m} is determined by the temperature, density and ionization scheme. Sets of parameters for each of the chosen schemes are tabulated at the bottom of the MULTI file, as per listing 6.1.5.

The three complementary ionization and recombination processes are treated separately in MULTI, and we need the best known schemes and parameters for each process. The schemes already incorporated in DIAPER, and used by default, are the ones described by Shull and van Steenberg (1982) (SS) for radiative recombinations; [3] Arnaud and Rothenflug (1985), with updated coefficients for ferrum from Arnaud and Raymond (1992) (collectively labeled AR) for collisional ionization; and Burgess (1965) for dielectronic recombination.

Mazzotta et al. (1998) surveys the field and compute their own ionization equilibria based on "the most recent data." Their paper is particularly interesting, both because it represents the most recent whole–field survey,

---

[3] Their collisional ionization parameters are ignored.

and because it comprises the newest equilibria included in the CHIANTI database.

```
* Shull & Steenberg, 1982; radiative recombination.
shull82
1 2
   0.00e+00   1.45e+06   4.12e-11   7.59e-01
   2.91e-01   2.29e-01   7.73e+05   6.54e+05
*
* Arnaud & Rothenflug 1985 scheme; rates from Arnaud
* & Raymond 1992.
* Collisional Direct Ionization
ar85-cdi
1 2
3
   124.20     14.60      -4.36     5.98     -10.50
   180.00     67.90     -20.60     9.82     -53.70
   220.90     15.60      -2.29     2.30     -10.60
*
* Collisional Excitation with Autoionization.
ar85-cea
1 2
1.000e+00
*
* Burgess 1965 rates for dielectronic recombination.
burgess
4 5 1.00e+00
```

Listing 6.5: Sample ionization process scheme entries in MULTI format.

They conclude that for the collisional processes, the AR scheme and parameters is the best choice. As for raditative recombination, SS is still the best choice for ions of Mg, Si, S, Ar, Ca, Fe I–XIV and Ni; except for the first four isosequences, they should be computed with the scheme and values from Verner and Ferland (1996). This scheme should also be applied for C, N, O and Ne, but with parameters from Pequignot et al. (1991). The highly ionized species of iron should be computed as per AR. Dielectronic recombination rates should be selected based on both atom and ionization stage, and the reader is referred to the paper for a list of parametrizations.

They also compare their equilibria with those in AR, and find very good fits (to within 10%) for all ions of H, He, N, Ne, Na, Mg and Si. Good fits are also found for O, C and Fe, with the exceptions of C II–III, O III–V and Fe XVII–XXI. From this I conclude that an update of the radiative recombination rates might be worthwhile, but that collisional rates can be left as they are. I defer the update to a later work, and base the results in the current paper on the schemes already present in DIAPER.

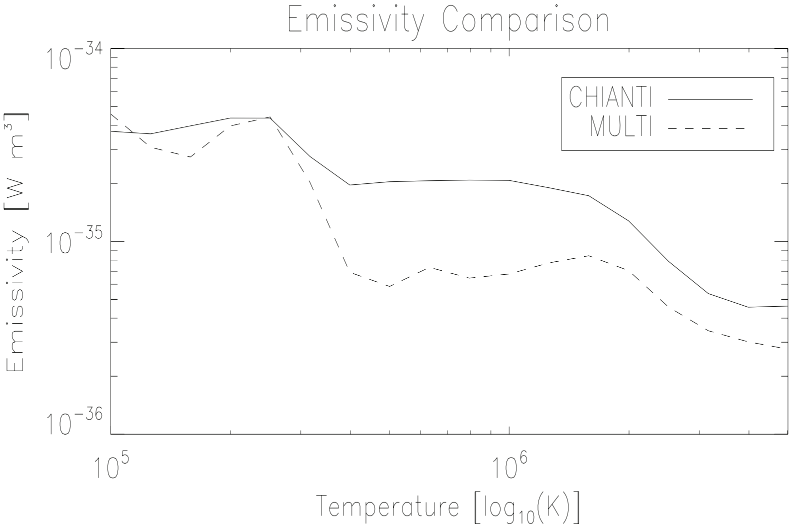

Figure 6.1.2: The total emissivity (all elements) tabulated for each database.

Of course, much time has passed since 1998, when that paper was written, and the physicists in the field have been far from idle. Newer and updated coefficients and schemes exist for all three processes, see eg. Gu (2003b) and Gu (2003a) for radiative and dielectronic recombination rates, respectively, and Voronov (1997) for collisional ionization. There is, however, a concensus in those papers, and in their citations, on the Mazzotta et al. results in the temperature and density regime relevant to us. I discuss the collisional scheme in appendix B.

6.1.8 Radiative Loss Interpolation

TTRANZ can treat radiative losses directly, or interpolate them from tabulated values corresponding to each element.

The tabulated value is the total emissivity, given as (using the notation of Landi and Landini (1999))

$$\eta(T_e, n_\mathrm{e}) \quad = \quad \int_\lambda \varepsilon(\lambda, T_e, n_\mathrm{e})\,\mathrm{d}\lambda \qquad [\mathrm{J\ m^3/s}], \tag{6.10}$$

where $\varepsilon(\lambda, T_e, n_\mathrm{e})$ is the emissivity,

$$\varepsilon(\lambda, T_e, n_\mathrm{e}) \quad = \quad G_\mathrm{line}(\lambda, T_e, n_\mathrm{e}) + G_\mathrm{cont}(\lambda, T_e, n_\mathrm{e}), \tag{6.11}$$

the sum of the line and continuum contribution functions (cf. section 2.3).

As we see, there is a marked difference in loss rate above 1.5×10^5K, pointing to coronal losses some 7–8 times higher using CHIANTI than with the TTRANZ values. Downwards of 10^5K opacity plays an increasingly important role, and must be accounted for in the loss function at $T \lesssim 10^4$K. Above $\sim 3 \times 10^6$K free–free losses are also non–negligible, but this is above the temperatures relevant to this thesis.

Based on this comparison, it seems proper to update the coronal loss rates with newer calculations.

6.2 The Selected Lines

6.2.1 Lines in the TRACE λ171 Band

In order to faithfully portray the coronal emission in the wavelength band seen by TRACE we need to include all the transitions in that band of non-negligible strength in the atomic models. Concretizing "non-negligible" here is the problem, as every added line will come with a penalty of increased computational complexity — we should make do with the smallest set possible.

I used a synthetic spectrum from CHIANTI as my guide, and chose the lines listed in table 6.2. An omission from this list (and from the simulations) is the Ni XV λ176.7 line, which becomes important at higher temperatures[4]. My set contains only iron and oxygen (O VI and Fe IX–XI).

6.2.2 Selected Energy Levels

Energy levels were selected based on three criteria. We need all those involved as upper or lower levels in the transitions we include, as well as the ground state and any higher levels that might populate the upper levels through cascades. Finally we need at least one level (the ground state) of each of the ions we included. More ions than just the ones being looked at are necessary for true ionization equilibria.

6.2.3 Complementary Lines

In addition to the lines dictated by the TRACE λ171–band, we should add some lines from the other spectral windows available to us in the TRACE and SUMER data. I chose C IV $\lambda\lambda$1548, 1551 (1.0×10^5K) which is seen by TRACE, N V $\lambda\lambda$1238, 1242 (1.5×10^5K) and O V λ629 (2.5×10^5K) from SUMER. While we certainly could have use for the Fe XII λ1242 forbidden line because then we would have both ions visible both to SUMER and TRACE, according to the CHIANTI database, its upper level population is dependent on radiative decay from too many higher levels; a realistic simulation would be too computationally demanding.

---

[4] Ni XV peaks at 2.5×10^6K under equilibrium conditions.

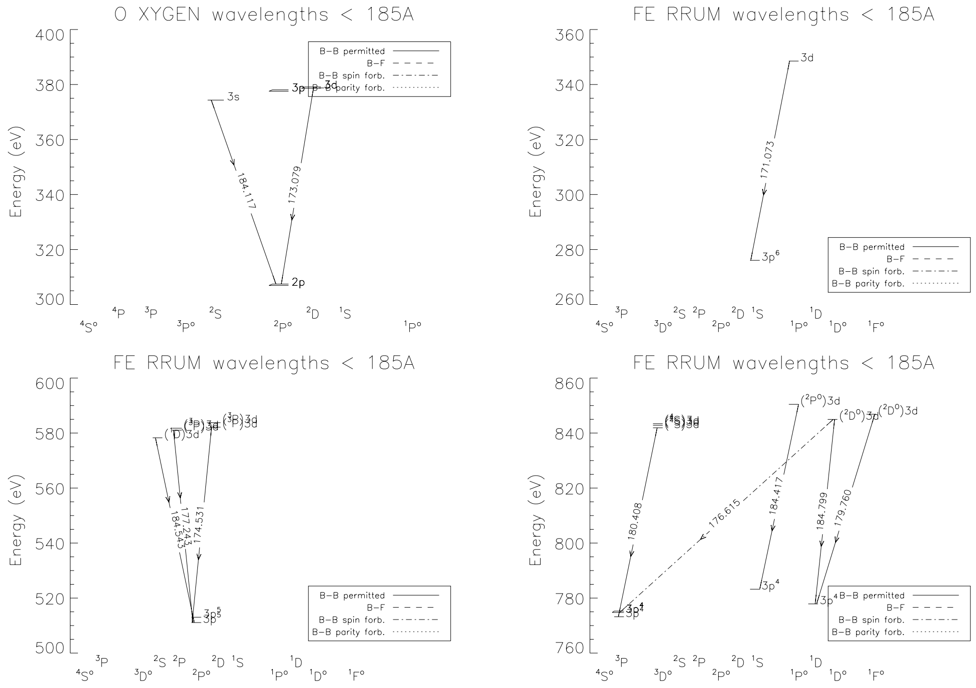

Figure 6.2.1: Grotrian diagrams showing: oxygen transitions near 70eV (173Å) (upper left), the Fe IX λ171 transition (upper right), Fe X transitions near 70eV (lower left) and Fe XI transitions near 70eV (lower right).

The information in the table can be visualized through Grotrian diagrams[5] of the ions, as per the figures in 6.2.1.

6.3 Comparison of Ionization Equilibria

We can test the chosen input parameters by computing synthetic plasmas and comparing their properties with empirical data and earlier simulations. On aspect which lends itself to easy testing in this way is the ionization equilibria, the fraction of each ion to the total density of the element,

$$\frac{N(X^{+m})}{N(X)}.$$

---

[5] The diagrams are produced by the termdiag IDL routine written by Judge and Carlsson and distributed in the HAOS DIAPER library.

Ion	Transition			Wavelength
	lower	←	upper	Å
O VI	$2p^1\,{}^2P^o_{1/2}$	←	$3d^1\,{}^2D^e_{3/2}$	172.935
O VI	$2p^1\,{}^2P^o_{3/2}$	←	$3d^1\,{}^2D^e_{5/2}$	173.079
O VI	$2p^1\,{}^2P^o_{3/2}$	←	$3d^1\,{}^2D^e_{3/2}$	173.095
O VI	$2p^1\,{}^2P^o_{1/2}$	←	$3s^1\,{}^2S^e_{1/2}$	183.937
O VI	$2p^1\,{}^2P^o_{3/2}$	←	$3s^1\,{}^2S^e_{1/2}$	184.117
Fe IX	$3p^6\,{}^1S^e_0$	←	$3p^5 3d^1\,{}^1P^o_1$	171.073
Fe X	$3p^5\,{}^2P^o_{3/2}$	←	$3p^4\,({}^3P^e)\,3d^1\,{}^2D^e_{5/2}$	174.543
Fe X	$3p^5\,{}^2P^o_{3/2}$	←	$3p^4\,({}^3P^e)\,3d^1\,{}^2P^e_{1/2}$	175.444
Fe X	$3p^5\,{}^2P^o_{1/2}$	←	$3p^4\,({}^3P^e)\,3d^1\,{}^2D^e_{3/2}$	175.266
Fe X	$3p^5\,{}^2P^o_{3/2}$	←	$3p^4\,({}^3P^e)\,3d^1\,{}^2P^e_{3/2}$	177.243
Fe X	$3p^5\,{}^2P^o_{1/2}$	←	$3p^4\,({}^3P^e)\,3d^1\,{}^2P^e_{1/2}$	180.407
Fe X	$3p^5\,{}^2P^o_{3/2}$	←	$3p^4\,({}^1D^e)\,3d^1\,{}^2S^e_{1/2}$	184.543
Fe XI	$3p^4\,{}^3P^e_1$	←	$3p^3\,({}^2D^o)\,3d^1\,{}^1D^o_2$	176.620
Fe XI	$3p^4\,{}^3P^e_2$	←	$3p^3\,({}^4S^o)\,3d^1\,{}^3D^o_2$	178.060
Fe XI	$3p^4\,{}^1D^e_2$	←	$3p^3\,({}^2D^o)\,3d^1\,{}^1F^o_3$	179.764
Fe XI	$3p^4\,{}^3P^e_2$	←	$3p^3\,({}^4S^o)\,3d^1\,{}^3D^o_3$	180.407
Fe XI	$3p^4\,{}^3P^e_1$	←	$3p^3\,({}^4S^o)\,3d^1\,{}^3D^o_1$	180.600
Fe XI	$3p^4\,{}^3P^e_0$	←	$3p^3\,({}^4S^o)\,3d^1\,{}^3D^o_1$	181.137
Fe XI	$3p^4\,{}^3P^e_1$	←	$3p^3\,({}^4S^o)\,3d^1\,{}^3D^o_2$	182.169
Fe XI	$3p^4\,{}^1S^e_0$	←	$3p^3\,({}^2P^o)\,3d^1\,{}^1P^o_1$	184.417
Fe XI	$3p^4\,{}^1D^e_2$	←	$3p^3\,({}^2D^o)\,3d^1\,{}^1D^o_2$	184.800

Table 6.2: The selected lines with wavelengths near 173Å. The selection criteria (mainly line strengths) are described in chapter 8.

This fraction varies with temperature mostly according to the ionization and recombination rates, but can be influenced by other factors. Of these the helium abundance probably is the most important one, due to its influence on the number of free electrons — an important parameter in Saha's equation[6]. The helium abundance differs by a factor 1.6 between the alternative data sets.

In this section I present equilibria produced by the TTRANZ engine with all the changes in the first section implemented, and compare the numerical results with the data presented by Mazzotta et al.. Since oxygen and ferrum are the atoms of interest in this study, I restrict the presentation to those two elements.

---

[6] In LTE the ionization balance is described by the simple expression

$$\frac{n_{i+1}}{n_i} = \frac{Z_{i+1}}{n_e Z_i} Z_e(T_e) e^{-\chi_i/\tau}.$$

Here χ_i is the energy necessary to ionize the stage i and the Zs the particles' partition functions.

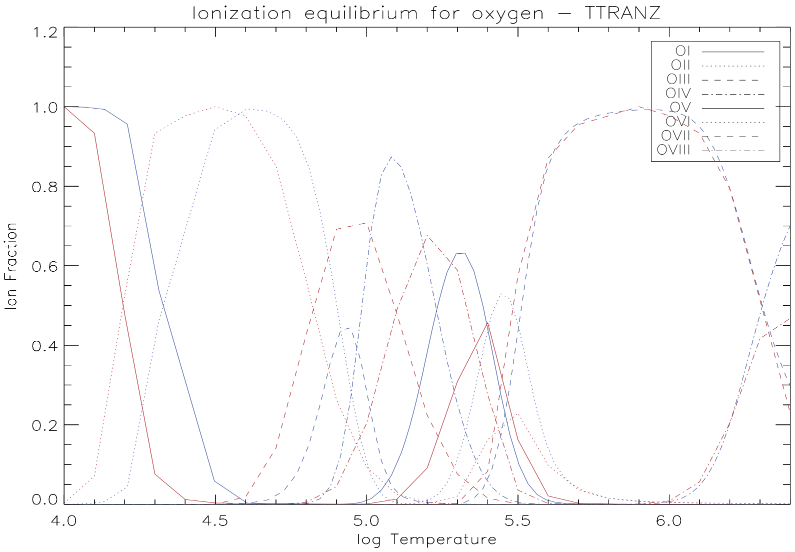

Figure 6.3.1: Composite image showing both the TTRANZ (blue) and the Mazzotta et al. (1998) (red) ionization equilibria.

The conclusion is that for both elements we have good fits with Mazzotta et al., with the notable exceptions of O VI and Fe IX which differ from their expected fractions by factors ~ 2, and that the effects of variations in helium abundance is negligible.

6.3.1 Ionization Equilibria for Oxygen

Starting with the oxygen, we find reasonably good fit between the results of our numerical analysis and the Mazzotta et al. data we use as a yardstick. The two equilibria are plotted in color in figure 6.3.1, with each ion represented by a different line style.

Even though the data match in a broad way, there are two important discrepancies, in the results for O III and O VI.

O III ionizes too easily, causing it to peak at too low a fraction, and thus increasing the fraction of the next ion in the sequence above the expected value. Quantitatively, as we see from table 6.3, the peak fraction of O III is 0.6 of the expected value, giving an O IV fraction at 1.3 times the expected.

For O V we have a different problem, as the population of this ion tapers off at too low temperatures. The consequence of this is that too much O VI is present at the latter ion's peak temperature. The peak fractions of these ions are 1.5 and 2.5 with respect to the Mazzotta et al. distribution.

These discrepancies directly affect the strengths of the lines produced by the affected ions. Particularly the high level of O VI ions should be kept in mind when the intensity of oxygen and iron is compared in synthetic TRACE λ171–band spectra.

Ion	Mazzotta et al.		TTRANZ	
	fraction	$\log_{10}(T)$	fraction	$\log_{10}(T)$
O I	1.0	< 4.0	1.0	< 4.0
O II	1.0	4.5	1.0	4.6
O III	0.7	4.9	0.4	4.9
O IV	0.7	5.2	0.9	5.1
O V	0.4	5.4	0.6	5.3
O VI	0.2	5.5	0.5	5.5
O VII	1.0	5.9	1.0	5.9
O VIII	1.0	> 6.4	1.0	> 6.4

Table 6.3: Oxygen peak ionization fractions and the temperatures at which they occur as reported by Mazzotta et al. (1998) and the synthetic data set produced by TTRANZ, respectively.

The selection of Fludra and Schmelz (1999) in place of photospheric abundances, with the corresponding change in the electron density, does not affect the equilibrium population distribution significantly[7].

6.3.2 Ionization Equilibria for Iron

These results, presented in figure 6.3.2 and table 6.4, show a good fit between the two data sets. But as in the case of oxygen, there are differences, and in this case the most important one is for Fe IX. This ion plays a key role in the TRACE λ171–band spectrum, and must behave predictably.

In Arnaud and Raymond (1992) the maximum fraction of the ion is about 75%, a peak that occurs at some 6.4×10^5K. In the simulated plasma we only reach a maximum fraction of 40%, at the high temperature of 8.0×10^5K. Since Fe IX is Argon-like, with a closed 3p-shell, the higher of the fractions is the more plausible one, and it would be interesting and useful to find out what causes the low fraction in TTRANZ. Two venues of investigation can be found in the appendices, but no definite conclusions were made.

The overabundance of Fe VII in the diagram is owed to the simple fact that no ions of lower degrees of ionization are present in the data file. This could be remedied by adding lower ionization states to the iron atomic model, if so were needed. Limitations in the LS coupling scheme does put a lower limit on how low ionizations stages we can reach, but this does not matter

---

[7] Hansteen (pers. comm.) points out that the probable reason for this that three–body recombinations are unimportant, and that the n_e factor cancels in the rate equation.

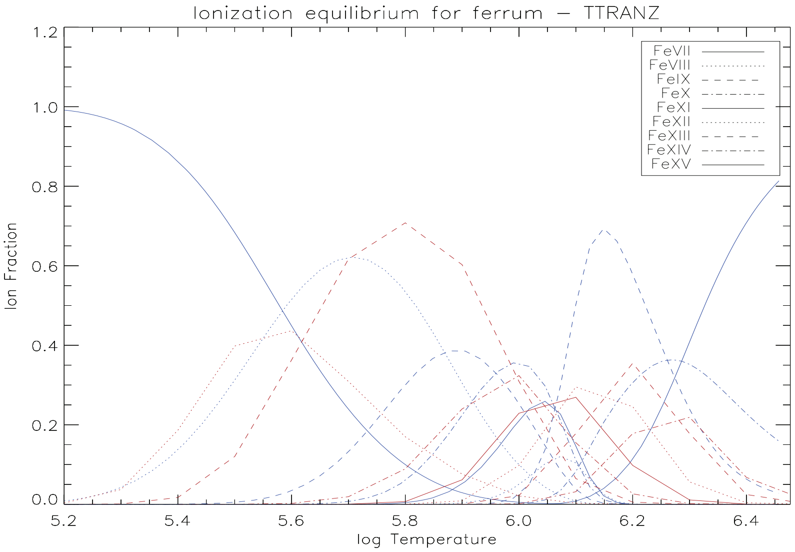

Figure 6.3.2: Joint plot of TTRANZ (blue) and the Mazzotta et al. (1998) (red) ionization equilibria for ferrum.

Ion	Mazzotta et al.		TTRANZ	
	fraction	$\log_{10}(T)$	fraction	$\log_{10}(T)$
FeVIII	0.4	5.6	0.6	5.7
FeIX	0.7	5.8	0.4	5.9
FeX	0.3	6.0	0.4	6.0
FeXI	0.3	6.1	0.3	6.1
FeXII	0.3	6.1	0.1	6.1
FeXIII	0.4	6.2	0.7	6.2
FeXIV	0.2	6.3	0.4	6.3

Table 6.4: Ferrum peak ionization fractions and the temperatures at which they occur as reported by Mazzotta et al. (1998) and the synthetic data set produced by TTRANZ, respectively.

in the temperature interval of interest to use, in which nothing less ionized than Fe VII, nor any stage above Fe XII, is really needed.

Between them, the high fraction of O VI and low fraction of Fe IX will boost the relative strength of oxygen to iron lines in the TRACE λ171–band by a factor 4 compared to the expected values.

Chapter 7

Simulated Transient Heating

With a solid set of atomic models for the metals in place, we can now shift our focus toward the practical problem of modeling atmospheric plasmas. While some authors, eg. Müller et al. (2003), showed us that transient behaviour can manifest itself in plasmas heated with constant parameters, I will use the direct method of modeling plasmas with the heat input rapidly changed from one configuration to one markedly different over a short period of time. This mirrors the approach used by Reale et al. (2000b, 2000a). Any resultant transient behaviour is then discussed and compared to the June 4 event.

7.1 Summary of the Heating Mechanism

The functional form of our heating models is described in chapter 2. To recapitulate, a background heating is impressed by a SRTV foot–focused model, as per Serio et al. (1981):

$$F_h^{\mathrm{SRTV}}(z) \quad = F_{h,0}\, m(z_H, z_0) \quad \begin{cases} 1 & \text{where} \quad z \leq z_0 \\ \mathrm{e}^{-\frac{z-z_0}{z_H}} & \text{where} \quad z > z_0, \end{cases} \tag{7.1}$$

here with a scaling function $m(z_H, z_0)$ included to ensure that the total heat input remains constant when the scale heights are changed. In addition to simple changes in the amplitude $F_{h,0}$ of this function, transient heating can also be applied through an apex–focused gaussian,

$$F_h^{\mathrm{flare}}(z,t) \quad = \quad F_{h,0}^{\mathrm{flare}}(t)\mathrm{e}^{\frac{-(z-z_0^{\mathrm{flare}}(t))^2}{z_H^{\mathrm{flare}}(t)^2}}. \tag{7.2}$$

Heating through this function is turned on for short amounts of time, emulating flare–like and fugacious heating of the corona.

Any impressed heat not countered by conduction towards the cooler chromosphere,

$$F_{\mathrm{c}} \quad \propto \quad \frac{\mathrm{d}}{\mathrm{d}z} T_e^{7/5}, \tag{7.3}$$

or through radiative losses

$$F_{\mathrm{r}} \quad \propto \quad n_{\mathrm{e}}^2, \tag{7.4}$$

where the simple density proportionality holds in the temperature regime $10^5 < T_e < 10^6$K, will change the specific heat $\rho\varepsilon$ of the local plasma. The system will be in a steady state (possibly cyclic, where it cycles through a closed set of states) when these variables balance,

$$\frac{\partial}{\partial z}(F_{\mathrm{h}} + F_{\mathrm{c}} + F_{\mathrm{r}}) \quad = \quad 0. \tag{7.5}$$

The "free variable" we can change in this energy budget is the heating, and our goal is to reproduce the June 4 event by changing the heating input for a short while, and letting conduction and radiation carry away the added energy. Because the event ended even more abruptly than it started, it is important that the method of heating sets the appropriate stage for the heat sinks. The equations above tells us when each of them will be effective: conduction works with high temperatures and gradients, and radiation with increased density.

Increased emission is the primary characteristic we want to replicate numerically — the energy loss through radiation is three times higher than the baseline at the emission peaks, corresponding to a 175% increase in density. Evaporation of chromospheric matter, caused by either more localized, or globally increased, heating, is needed to bring about this effect.

7.2 Synthetic Emission Profiles

The true state variables of the simulated plasma are immediately available to us, but we need a way to correlated these values with our observational data. I use two tools: Line analysis of column–integrated synthetic line profiles and full loop intensities calculated from synthetic spectra convolved with the TRACE response functions.

The first of these will replicate SUMER observations by first calculating the column emission from a segment of the loop, and then utilizing line moment analysis on this synthetic column spectrum. Line moment analysis is explained in section 2.3, it gives us a measure of the intensity, velocity and temperature in the specified area. The actual part of the loop integrated over is 1–5Mm, approximately the TR–corona interface seen by SUMER.

The second tool divides the loop into narrow sections, and computes the emission spectrum from each segment. This spectrum is then convolved with the TRACE response functions, producing an X–T diagram showing the DNs measured by TRACE, rather than the true emission from each loop segment. In special cases, such as low–temperature O VI emission and loss of equilibrium, the λ171 counts can be radically different from those induced by the expected ∼1MK Fe IX/X plasma. The convolution process and its effect on the TRACE λ171–band is described in chapter 8.1.

The contradictory results between the true state and moment analysis that caused trouble back in chapter 3 reveal that interpretation of results obtained through this analysis method is no simple matter. It is greatly helped by numerical simulations, which gives us a way to draw parallels between theory and observation. As an example of the difference, contrast the left panel of figure 7.5.1 with the bottom panel of figure 7.5.2. They both report temperatures, but figure 7.5.1 shows the "exact" state variable read directly from the CFD–analysed plasma while figure 7.5.2 shows results inferred by line analysis of spectra synthesized from it.

The analysis is performed on the TR, defined for this purpose as the segment of the loop with $z \geq 22.5$Mm. The cells (at a specific time) which this segment comprises are indicated in plot 7.6.1 below.

7.3 Loop Geometry and Boundary Conditions

The observations point to an initially relatively cold loop, of some $20 - 30$Mm in length. I try to fulfill these initial conditions by designing the loop with a foot–to–foot length $L = 25$Mm long and an apex temperature of $1 - 2 \times 10^5$K.

In all cases was the loop advanced to a steady state before the heating was applied, to rule out any coincidental transient effects of purely numerical nature, or due to untrackable initial disturbances.

The loop is defined geometrically as a uniform–width semi–circle, tracing the full 180° without shearing or any inclination relative to the vertical. Its shape is kept constant in time (no morphology changes). While we could not measure the variation in loop cross section with height, keeping it constant should be acceptable for a low β coronal loop (eg. Watko and Klimchuk 2000).

The plasma boundary conditions defining the chromospheric footpoints of the loop are those of stationary plasma, with the temperature and pressure are set to 7000K and 100Pa, respectively.

7.4 The Heating Experiments

The composite heating function

$$F_{\mathrm{h}}(z,t) \quad = \quad F_h^{\mathrm{SRTV}}(z) + F_h^{\mathrm{flare}}(z,t) \tag{7.6}$$

provides us with a wide range of simulation possibilities that could potentially replicate the observed transient event. I narrow these possible experiments down to five.

The first three experiments introduce a time dependence into the SRTV heating with the intent of revealing if variations in this fundamentally hydrostatic model can reproduce the event. They are divided into two types; in the first one, the scale height z_H is changed. The following two experiments test a change of the amplitude $F_{h,0}$ to a much greater value. The first of these is the simple case of symmetric increase, the same amount of energy is applied at both loop feet. In the second, because we observed some assymetry in the TRACE data, especially prior to the event, I also perform one experiment where heat is only increased in one loop leg.

The final two experiments test the flaring model, with energy applied towards the loop apex. These are in turn divided into one run where the center of the gaussian remains fixed at some point slightly offset from the apex, and one where the focus point is allowed to travel from the left part of the corona and into the right.

In summary, we have seven experimental setups:

— change from uniform (RTV) heating to foot–focused heating; and back again (section 7.5),
— symmetric increase in amplitude $F_{h,0}$ (section 7.6.1) and
— asymmetric increase in left foot amplitude $F_{h,0}^{\text{left}}$ (section 7.6.2),
— apex–focused stationary heat release (section 7.7), and
— release of energy with a locus moving through the loop (section 7.7).

While these runs are not expected to produce exact replica of the observed band emissions, they should nevertheless provide valuable insight into the processes that can cause such rapid intensity fluctuation. These experiments are as simple as possible, and it is possible that more construed cases such as a tailor made energy deposition function can yield much more precise results. Those refinements are reserved for later projects.

7.5 The Scale–Change Experiments

Experimental Setup

The first experiment is intended to reveal what effect a forced change in the energy distribution has. The heat e–folding height z_H is changed instantly from one extreme value to another, and then returned to its initial value 500 seconds later. The factor $m(z_0, z_H)$ in equation 7.1 ensures that this does not change the available energy.

An amount $F_{h,0} = 1.5\text{W/m}^2$ of energy is provided in each loop leg, enough to bring the loop into the projected temperature range near $\sim 1.5 \times 10^5\text{K}$.

Even without any net increase in energy, the experiment can create interesting dynamics due to the change in focus. When the heating is shifted downwards, the corona will cool off and a downflow develop, while at the

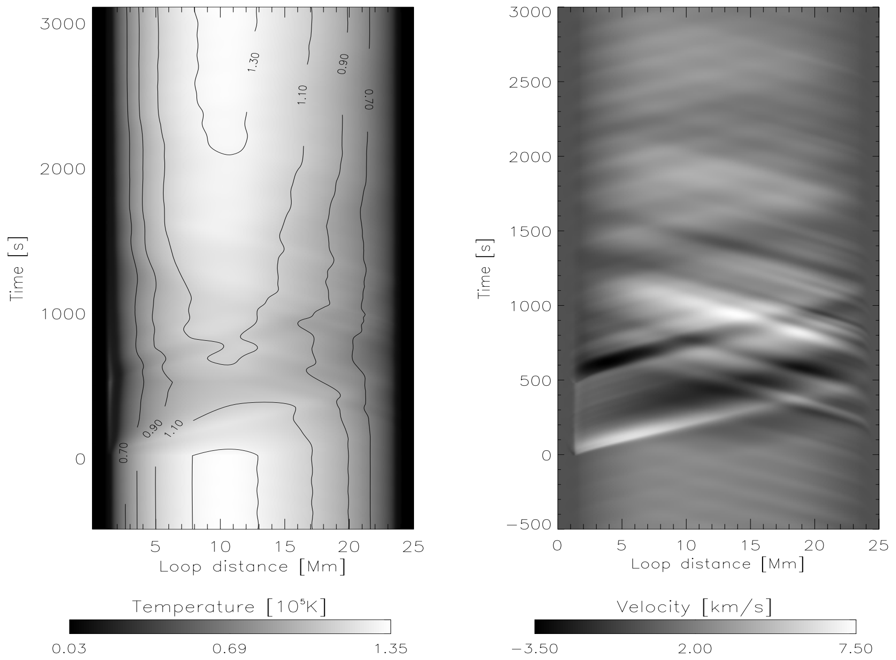

Figure 7.5.1: Temperature and velocity response to "focused" heating towards the footpoints, triggered at $t = 0$s.

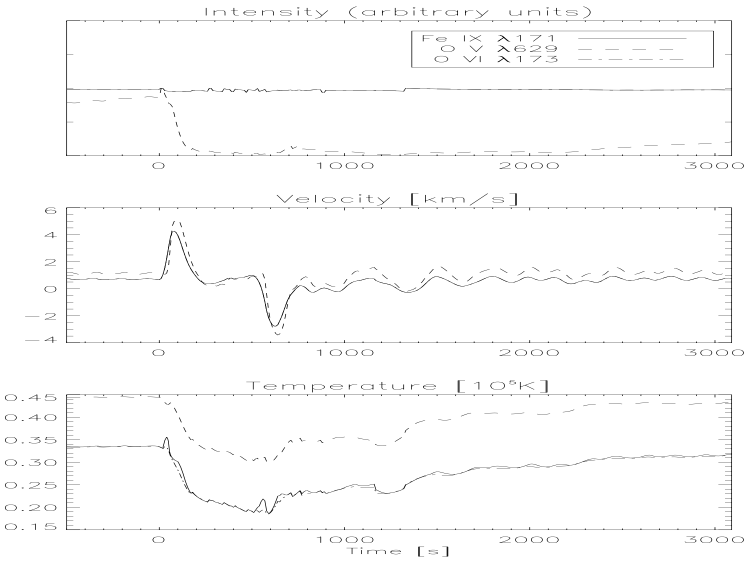

Figure 7.5.2: TR intensity, velocity and temperature development in the Fe IX λ171, O V λ629 and O VI λ173 lines caused by a rapid reduction in heating scale height.

same time the lower TR is heated and expands. The converse should hold when the shift is upwards. The strength of this energy re–shuffling is of course linked to the heating amplitude.

Development

A uniformly heated loop was allowed to reach steady–state. At $t = 0$ the heating function was abruptly changed to one with a very much shorter e–folding height of only 0.1Mm (essentially depositing all the energy into a thin segment of the TR), and left in the new state for 500s.

As expected, this both evaporates chromospheric matter and condenses coronal. The evaporation far outweights the condensation, however, which means that the loop density grows quickly behind a front travelling upwards at $u \approx 7.5$km/s. The front reaches the apex of the loop after at $t \approx 4$min, and then continues some distance into the right loop half, indicating an initial density asymmetry.

Over the four minutes this chromospheric evaporation phase lasts, the temperature falls off at a comparable rate to the density buildup, and the process can thus be considered enthalpic. The velocity of the front is so low that the plasma in practice is in steady state right behind it.

At $t = 500$s, the heating was changed back to the uniform model, with a scale height much greater than the loop length. This restored the loop very slowly to its initial steady state configuration, over about one hour.

The temperature and velocity development during the experiment is depicted in the X–T diagrams of figure 7.5.1. Below it are three panels graphing the intensity, velocity and temperature of the TR, calculated as described in section 7.2.

The graphs exhibit some unexpected features. Because of the low temperature, only the O V line responds at all, and the intensity in this line reacts immediately at $t = 0$s, with a drop to a tenth of its initial value because of the recombination towards O IV. Since the temperature only rises very slowly, the intensity in this line remains very low for the remainder of the simulation.

The velocity, howevery, responds in a predictable manner. At $t = 0$s we have a short–lived blueshift lasting two minutes and peaking after one, while at $t = 500$s, when the scale height is reset, we have a similar redshift.

Finally, the temperature reflects the intensity plot, with an sudden and rapid drop at $t = 0$s, reaching a minimum at $t = 500$s (close to, but not quite at the lowest possible level for this heating configuration), and then very slowly rising again when the heating scale height is reset. Surprisingly, the O V line indicates a higher temperature than the two λ171–ions, and all three report a much higher temperature than the real.

If the observed loop was subject to a similar configuration change as this experimental loop, the SUMER diagrams 3.4.1, 3.5.1 and 3.6.1 should be comparable to figure 7.5.2. They clearly are not, which rules out a simple scale height change as the source of the observed intensity burst.

All in all, these changes brought with them surprisingly modest loop dynamics.

7.6 The SRTV Amplitude–Change Experiments

For the four experiments in this and the next section, in which the energy input is changed, the projected temperature near $\sim 1.5 \times 10^5$K is achieved by using the heating parameters $F_{h,0} = 1.5\text{W/m}^2$, $z_0 = 1.7$Mm and $z_H = 6.0$Mm. Figure 7.6.1 shows the temperature structure prior to the effected changes.

A z_H of 6Mm is close the lower limit recognized by Serio et al. (1981), where the loop is susceptible to Rayleigh–Taylor instability. The temperature profile of the simulated loop is in other words close to an unstable equilibrium, and just a small change in z_H can move the temperature maximum from the apex towards the TR. The treshold in the cited paper is at $z_H \sim L/3$ (L is the loop length), a result consistent with the $\sim$ 5Mm threshold observed in my analysis.

7.6.1 Symmetrically Increased Heating Amplitude

The experiment starts at $t = 0$ by instantly increasing the heating amplitude $F_{h,0}$ by a factor 500 in each loop footpoint, to 750W/m^2. This greatly increased heating was applied for 500 seconds, after which the original heat input was restored. The plasma was then allowed to develop for another hour.

The development in temperature and bulk velocity is reported in the panels of figure 7.6.2. In the three panels of figure 7.6.3 beneath it the intensity, velocity and temperature are reported as they would be seen by a spectrograph (cf. section 7.2), the loop slit is placed over the TR segment of the right loop leg, from 22.5Mm to 24.8Mm (marked with $\circ$ in figure 7.6.1).

The temperature rises surprisingly fast when the heating is applied, a mere minute after $t = 0$, the loop reaches a plateau with an apex temperature of more than 7×10^5K, and it adapts an isothermal profile.

The z_0 term in the heating function prevents direct heating of the chromosphere, but it receives a lot of energy through conduction from the hot corona. As soon as the heating is applied, conduction through the TR heats the chromosphere, and ablation causes pressure fronts to travel at nearly sonic speeds up towards the corona. These reach the apex after 60 seconds, practically at the same time, and die out, a process that necessarily disperses a lot of energy.

The loop has now gone from isothermal to strongly dome–shaped (global temperature maximum at the apex). A conduction front sent downwards

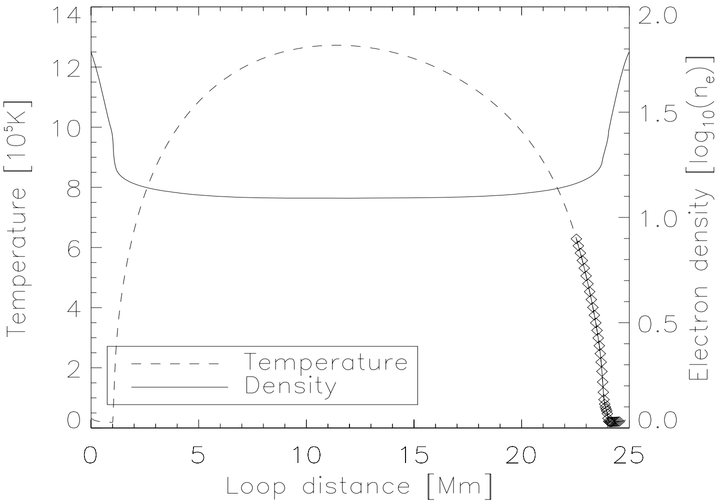

Figure 7.6.1: Temperature structure in the loop used as basis for the amplitude–change heating experiments. The segment of the loop on which the synthetic line profiles are made is indicated by circles on the temperature graph.

helps distribute the input energy very well, and together with the increased emission losses (due to the increased density behind the pressure front), radiation and conduction are strong enough to counter the input energy. A semi–stable state has now evolved, with T_e nearly constant until the heat is removed, and a slow but steady influx of matter into the corona.

The high density makes radiation a very effective energy sink, and as soon as the heat is no longer applied, the temperature starts to drop. Over the ten minutes past this point it reaches nearly the preheating level. This is too fast for the matter to react, thus the loop stays in an artificially dense state. Specifically, T_e drops with an e–folding time of 850 seconds, and ρ at the much slower 1790s.

Since the radiative losses in the artificially high–density corona are stronger than the heat input, the temperature falls to half of what it was prior to the onset. In other words, the plasma has actually been cooled off by the heating process.

7.6.2 Asymmetrically Increased Heating Amplitude

This experiment uses the same setup as the previous one, but in this case the heating is applied in only one footpoint. To offset the heating loss assiociated with heating in one instead of two footpoints, the amplitude change here is twice what we used above. Thus $F_{h,0}$ in the left foot is set to 1.5kW/m^2

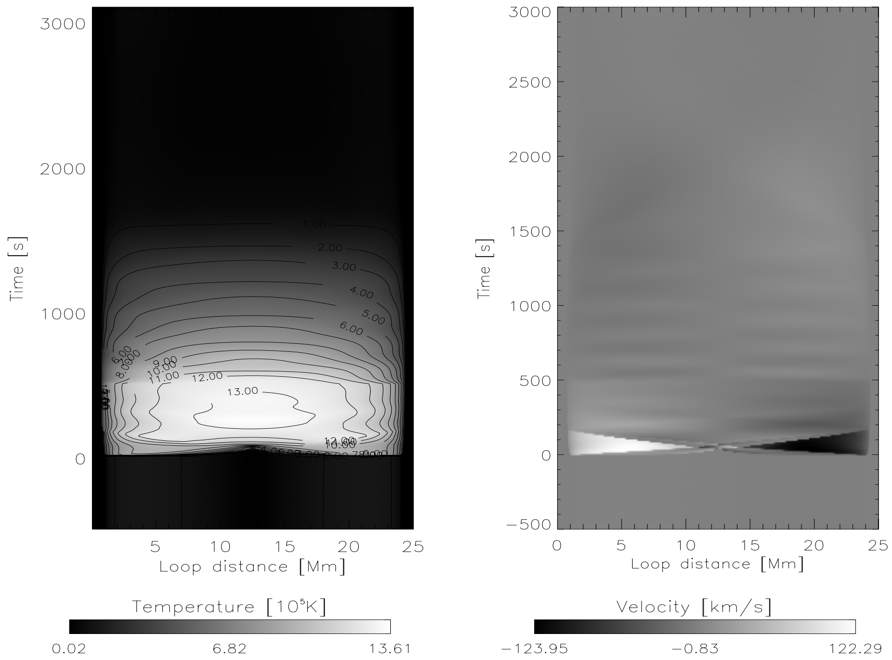

Figure 7.6.2: Temperature and velocity response to a symmetric change in heating amplitude in a cold loop, triggered at $t = 0$s.

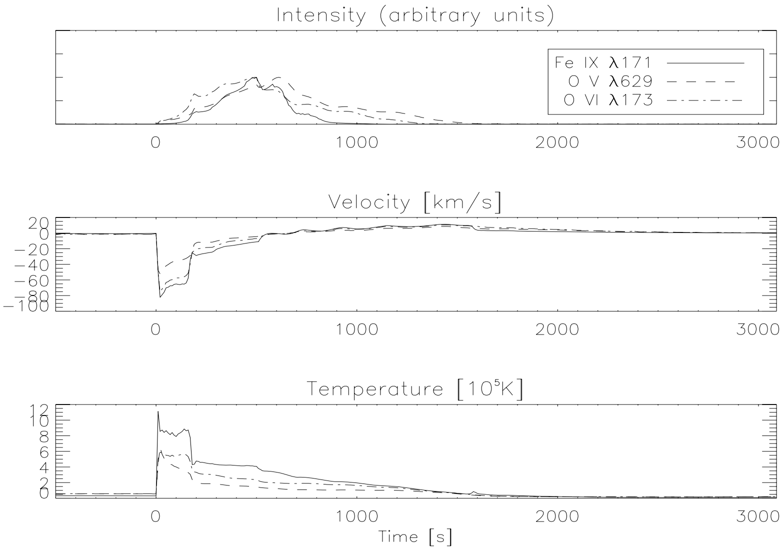

Figure 7.6.3: Integrated TR intensity, velocity and temperature development in the Fe IX λ171, O V λ629 and O VI λ173 lines caused by a symmetric increase in heating amplitude.

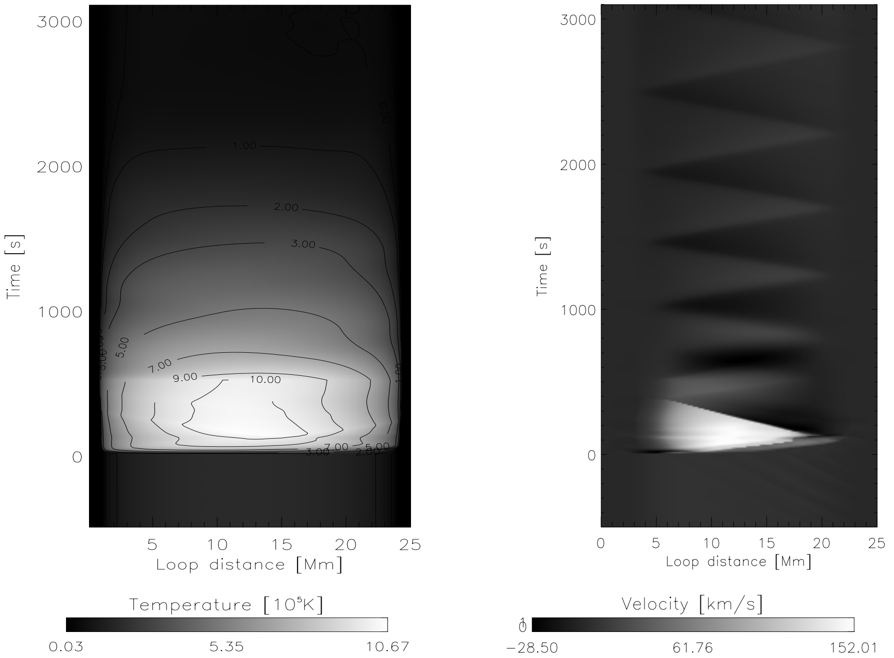

Figure 7.6.4: Temperature and velocity response to an asymmetric change in heating amplitude in a cold loop, triggered at $t = 0$s. Only the left side was changed ($z = 0$).

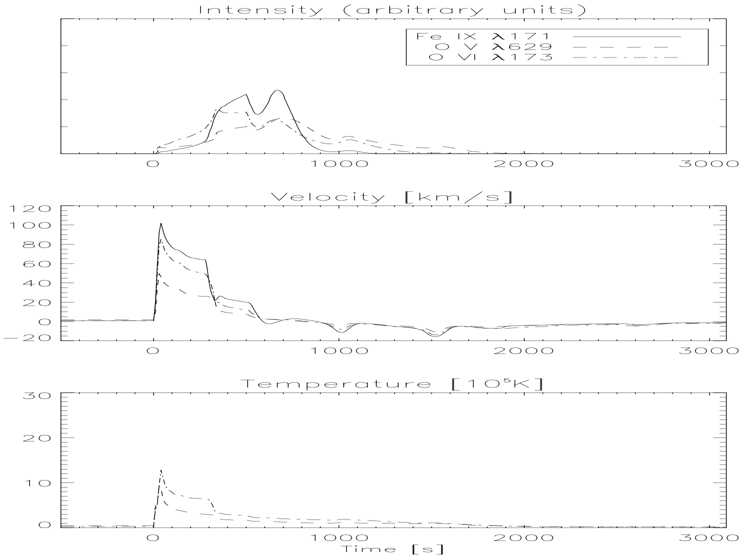

Figure 7.6.5: TR intensity, velocity and temperature development in the Fe IX λ171, O V λ629 and O VI λ173 lines caused by an asymmetric increase in heating amplitude.

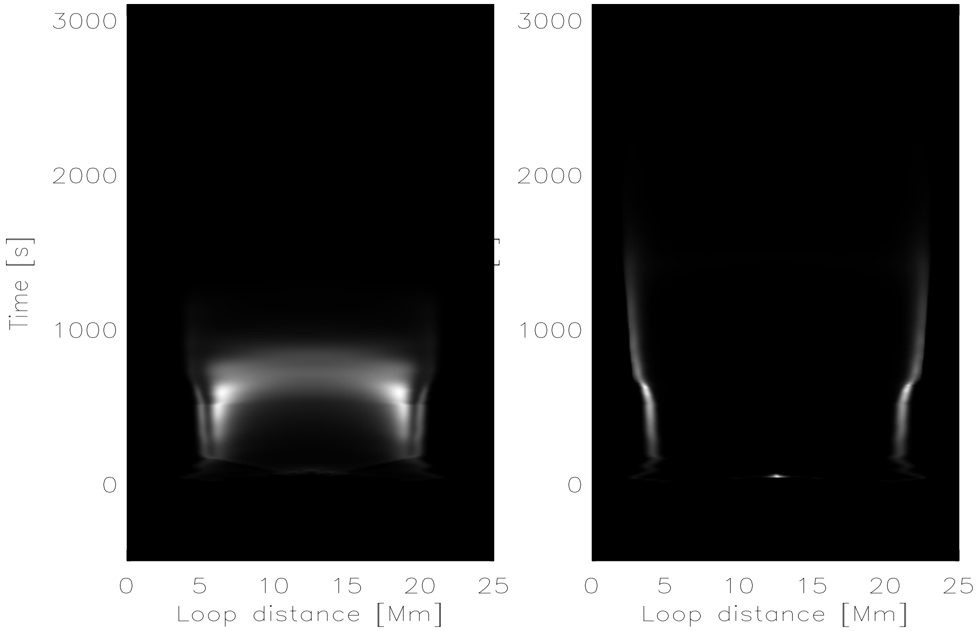

Figure 7.6.6: Loop intensity in the TRACE λ171 and λ1550 bands after convolution with the instrument's band pass function. The shading is in arbitrary units.

during the 500 seconds of heating. There is no linear relationship between the amplitude and loop temperature however, so we do not get exactly the same temperatures as we did with symmetric heating.

The effect of this experiment is strongly dependent on the deposition scale height, if z_H is high enough for the heating model to be near–uniform, this is essentially a repetition of the previous one. z_H is kept at the low 6.0Mm here to ensure that the focus really is in the left half.

The development of the true state variables are described in figure 7.6.4, and those computed from synthetic line profiles in figure 7.6.5.

The run starts off in much the same way as the previous one, with a very rapid heating phase. Chromospheric material evaporates just like it did above, but this time a greater part of the material necessarily comes from one side of the loop (the left). Less material is advected into the corona, causing a slower build–up of density — in fact, the density reaches a maximum in the corona only after the heating is reset to its initial level, at $t \approx 600$s.

This asymmetry results in a very different cooling phase. The evaporated material starts to fall back into the corona some 500 seconds earlier now than above, and in a much more steady fashion.

The more rapid fall in density is probably the agent of the slower temperature drop (e–folding time of 1300s) in this case. Nevertheless, the density stays sufficiently high to cool of the corona to beneath the pre–event level.

7.6.3 Comparison with Observational Data

Intensity

In both the symmetric and the asymmetric experiments the event unfolds over a time period comparable to the observations. The intensities grow slowly at first, but pick up their pace at 200s and 300s in the symmetric and asymmetric scenarios, respectively. All the emission lines share this general trend, but while the $\lambda 171$–lines grow from ~ 0 at $t = 0$, the O V line makes a small jump at this time.

After this initial growth, the $\lambda 171$–lines peak sharply. The peak occurs at $t = 500$s in both experiments, suggesting that the intensity would have risen even more if the heating had not been removed at this time. A second peak is seen at $t \approx 700$s, possibly because the atoms recombine into the emitting ions as the plasma cools. This peak is much more pronounced in the asymmetric case.

A density plot (not shown) supports the claim that the intensity grows as the square of the density, but the strength of the individual emission lines are also subject to the atoms' ionization temperatures. This is why the hotter Fe IX $\lambda 171$ line of figure 7.6.3 drops off so fast when the heating is removed, even though the density is still high; the Fe IX rapidly recombines, and we lose this emission line. The oxygen lines ionize at much lower temperatures, and are therefore affected more slowly by the temperature drop. We observe peaks from all bands at the same time because the intensity is integrated over a column comprising many strata of different temperature.

The corresponding asymmetric intensity plot is shaped by the same constraints, but the results plotted in figure 7.6.5 are more complicated than those of 7.6.3 because the density continues to grow even after the event, while the temperature sinks. The trough between the peaks occurs because at this time the temperature sinks faster than the growth in density.

Figure 7.6.1 shows the $\lambda 171$ and C IV emission, after convolution with the TRACE band response function, in the symmetric case. $\lambda 171$ is spread out throughout the entire loop very rapidly, as in the observational case[1]. Unfortunately, the C IV emission does not respond to any changes above the TR, probably because it ionizes before the density is high enough to cause the emission bursts.

A qualitative investigation suggests that the different emission lines react more in phase with each other when the scale height z_H is low, ie. with an isothermal corona.

---

[1] The band intensity is sampled at 10s intervals, four times the cadence of TRACE.

Velocity

The velocities derived for O V λ629 and N V λ1238 from SUMER line analysis are presented in figure 3.5.1.

Symmetric and asymmetric heating produce very different velocity measurements. Asymmetric heating causes downflow, rather than upflow, in the monitored TR — this is the half without increased heating. This was predictable, with more heating in the left half a pressure gradient is bound to point to it, pushing matter down towards the right half.

The flow in the symmetrically heated loop actually looks very much like what we see in O V. The flow looks stronger in the synthetic images than in the SUMER analysis because the SUMER data is not corrected for line of sight–errors.

We have the same characteristic initial peak, followed by a strong downflow, on which upwards travelling waves are superimposed.

Temperature

As for the temperatures, neither experiment results in matching profiles. The temperature (line width) measurement mirrors the velocity (ie. line shift) measurements.

Again the symmetric case comes closest to replicating the observations, with a temperature peak that is more short–lived than the combined emission peaks. While the low signal to noise ratio of the observed widths make this statement hard to substantiate as strongly as I would like, it does look like the synthetic temperature profile tapers off too slowly when compared to the observations, presented in figure 3.6.1. All in all, the fit is quite weak.

7.7 Flare–Like Coronal Heating

The final two experiments are the most complex ones. Here the background SRTV heating is kept constant at its low level, but a lot of energy is released into the corona through the "flare–like" model of equation 7.2: $F^{\text{flare}}(z, t)$.

The boundary constraints are the same here as they were in the previous section, ie. $F_{h,0} = 1.5\text{W/m}^2$, $z_0 = 1.7\text{Mm}$ and $z_H = 6.0\text{Mm}$. The gaussian term was kept at zero, except during the simulated event:

$$F^{\text{flare}}_{h,0} = \begin{cases} 375\text{W/m}^2 & \text{where} \quad 0\text{s} \leq t \leq 500\text{s} \\ 0\text{W/m}^2 & \text{elsewhere.} \end{cases} \tag{7.7}$$

The width of the gaussian was kept at a constant 1Mm in both of these experiments, the defining difference was the treatment of the focus point z_0.

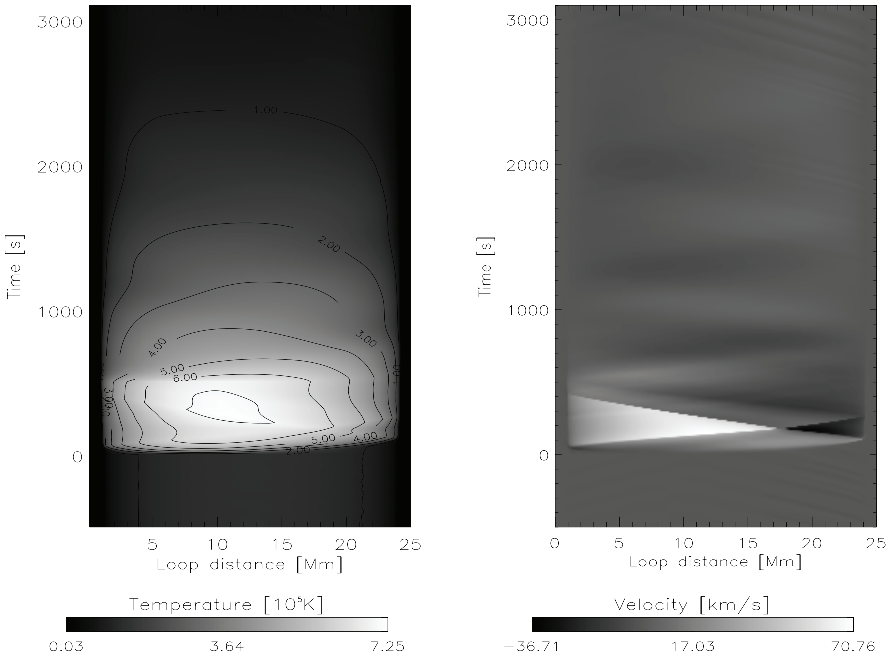

Figure 7.7.1: Temperature and velocity response to a small flare–like coronal heating centered at a constant height.

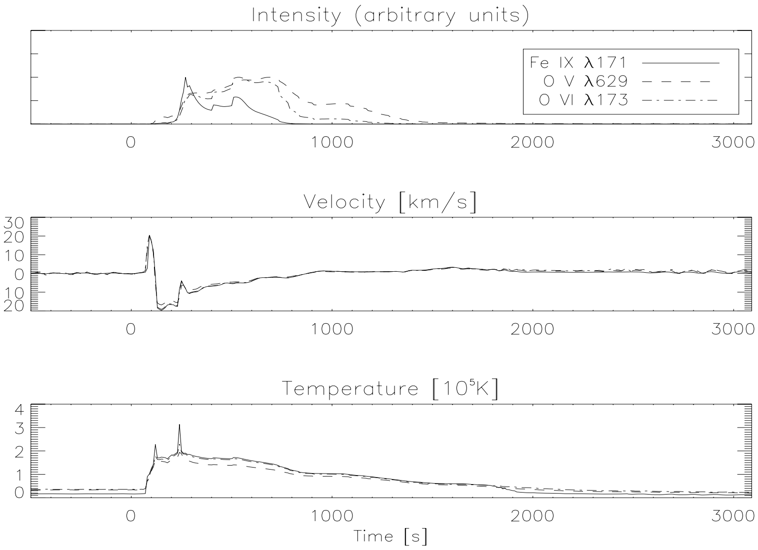

Figure 7.7.2: Integrated TR intensity, velocity and temperature development in the Fe IX λ171, O V λ629 and O VI λ173 lines caused by a small flare–like coronal heating centered at a constant height.

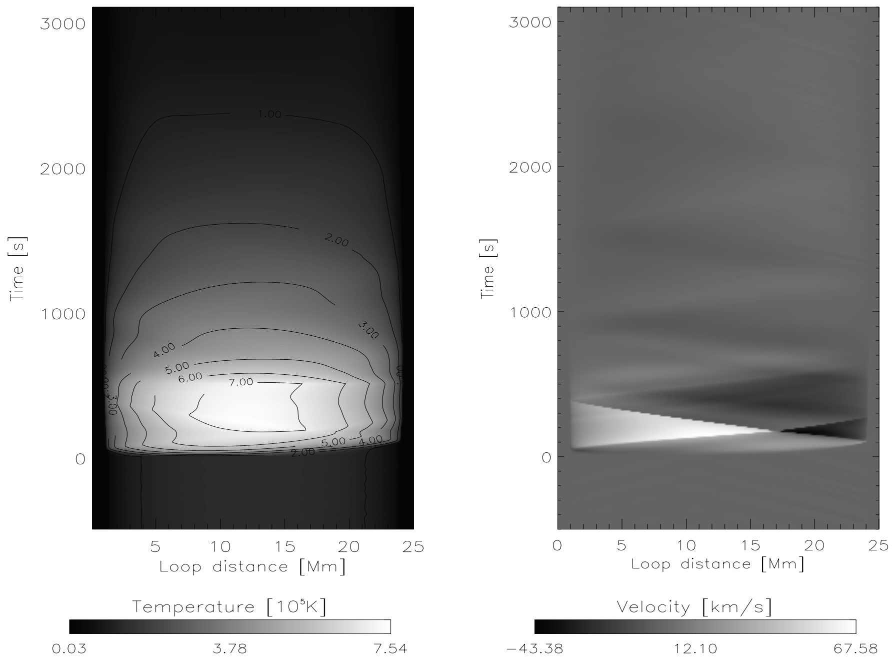

Figure 7.7.3: Temperature and velocity response to a small flare–like coronal heating centered at a constant height. Heating is centered at z =7.5Mm at t =0s, and moves steadily towards z =15Mm, reaching it at t = 500s.

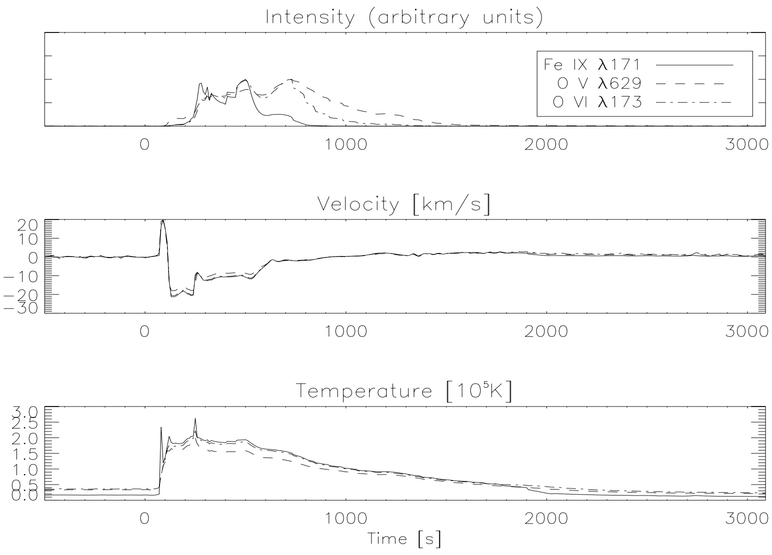

Figure 7.7.4: TR intensity, velocity and temperature development in the Fe IX λ171, O V λ629 and O VI λ173 lines caused by a small flare–like coronal heating centered at a constant height.

7.7.1 Loop Development

In the first of these experiments, the focus of heating was kept fixed at $z_0 = 7.5$Mm. In the second, z_0 was set to 7.5Mm at $t = 0$s and was then moved steadily towards $z_0 =$15Mm.

Both experiments produced similar characteristics, thus their macroscopic developments can be treated as one (these traits are also reminiscent of those produced by SRTV heating).

As soon as the heat is applied, the temperature grows strongly, reaching 10^6K in only about 60 seconds. At the same time evaporation from the chromosphere sets off strong pressure fronts towards the corona; their energy is dissipated when they meet, at $z = 17$Mm. Behind the pressure waves the density grows and the temperature profile is forced into one more "dome–shaped" (stronger gradient). Radiation and conduction is thus suddenly made very effective, and the temperature growth is halted. This is depicted in the panels of figures 7.7.1 and 7.7.3. Again, graphs depicting the intensity, velocity and temperature of the loop as they would be measured by a spectrometer are plotted in the panels of figures 7.7.2 and 7.7.4.

Both experiments behave like the symmetric SRTV–case when the heat is removed. The temperature drops with a time scale of $\sim$ 870s and the density with $\sim$ 2700s, and again we have the strong cooling–effect due to increased radiation beyond $t = 2000$s.

7.7.2 Comparison With Observational Data

Despite the apparent similarity in how the event unfolds throughout the loop, there are some marked differences in the emission lines produced; compare the X–T plots of the TRACE λ171–band loop emission (figure 7.7.5) with the results from the previous section (left panel of figure 7.6.6). In these panels, the loopwide emission starts at the very beginning, when the heat is applied, and is localized to the TR when it is removed. This behaviour is the opposite of what the experiments of section 7.6 produced, it is most likely caused by the fact that we then applied the heat to the footpoints, and in the current case apply it directly to the corona.

In both these experiments interesting emission profiles are produced. All three examined lines start off with an initial peak (top panel of figures 7.7.2 and 4), which is followed by another peak at $t = 500$s in Fe IX λ171 and another two peaks at $t = 500$s and $t = 700$s in O V λ629 and O VI λ173. Several of the characteristic traits seen in the SUMER data are reproduced here, but there are some major differences, like the decoupling of Fe IX from the other ions — is this because the TRACE λ171–band emission observed is from O VI λ173 rather than Fe IX λ171? The temperature in loop segment from which the graphs of figure 7.7.2 and 4 is produced remains below 6×10^5K during the whole experiment, in other words firmly below the

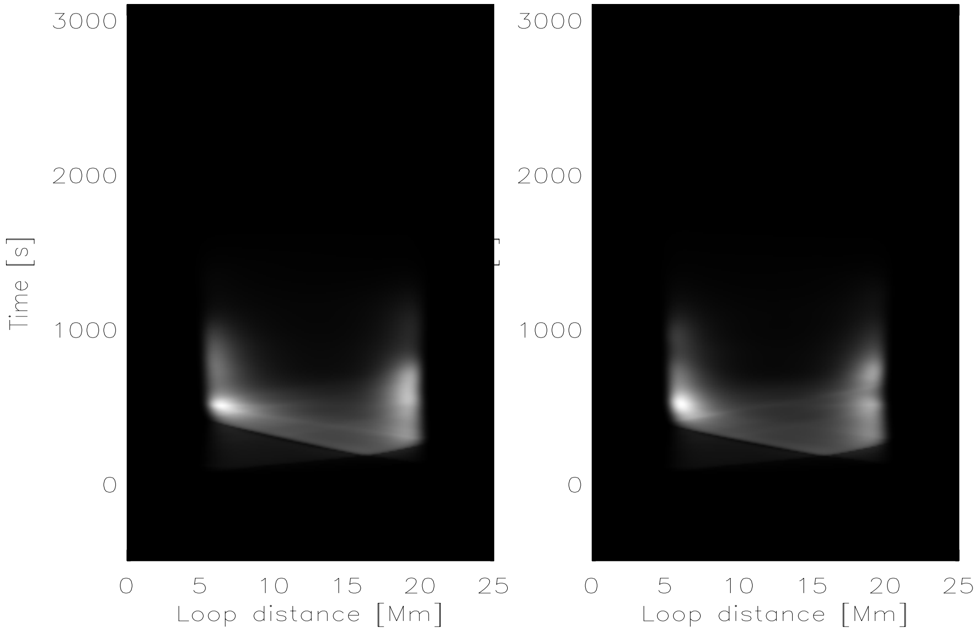

Figure 7.7.5: Loop intensity in the TRACE λ171 band after convolution with the instrument's band pass function. The fixed–position experiment is depicted on the right, and the moving–focus experiment on the right. The shading is in arbitrary units.

formation temperature of Fe IX. This certainly indicates that the photons measured by TRACE (at least at this height) were produced by oxygen, rather than iron.

The velocity plots are very similar to those seen in the SUMER data; particularly SUMER's O V–line. A strong but short downflow is followed by a strong upflow, which gradually settles back toward zero.

The calculated temperatures (line widths) however, do not fit the observations very well. The main problem here is the time necessary for it to fall back to the background level; in the real event this was nearly instantaneous, with a drop from maximum to background in about four frames (two minutes). On the other hand, these experiments managed to reproduce the two peaks at the start and end of the event. Clearly, more work needs to be done before the differences between the real and the synthetic temperature profiles are understood.

7.8 Discussion

The quiet–loop data obtained in chapters 3 and 4 was used to construct simulations for the TTRANZ advection engine, with the loop temperature defined by a foot–focused background heating model coupled with a transient heating from the apex. Transient behaviour similar to what the telescopes observed was found to occur when the energy input was suddenly increased in the loop for about 500 seconds.

The numerical analysis reveals that the loop is subject to three processes, each responsible for the three stages; ie. the initial emission plateau and subsequent peaks. All owe their effect to the strong dependence of radiation on density.

When the heating is amplified, the temperature in the low–heat capacity coronal section of the loop grows rapidly, while the density jumps and then flattens out. This causes a corresponding jump and plateau in intensity.

High temperatures and strong gradients make thermal conduction efficient, and the temperature is capped at about $\sim 10^6$K as a conduction front starts to move downwards. The strong energy transfer into the chromosphere causes evaporation, and a strong (subsonic) pressure front is sent upwards. Behind this front the density quickly grows by a factor ~ 1.5, corresponding to a doubled radiative loss rate. This strong emission is cut short when the heating is attenuated back to its background level, giving the appearance of an emission peak.

When the heating is attenuated the temperature quickly drops, but the density responds very slowly. This creates a favourable environment for recombination into the emitting ions, producing the second emission burst. Because this happens in different heights depending on the ion, the phases become incoherent at this point.

Chapter 8

The TRACE λ171 Passband

In this chapter I analyze what, if any, effects a loss of equilibrium in a monitored transition region plasma will have on the intensity seen by TRACE in the λ171 passband. The design of the filter is first described, followed by applications of it on synthetic spectra made to mimic steady state and highly dynamic coronal loop plasmas. An interesting deviation in counts is found in the dynamic plasma spectra, where the data numbers actually report O VI emission as Fe IX/X in temperatures we only would expect the latter ions to exist.

8.1 The Band Response Function

The 6.4Å FWHM TRACE λ171–band, centered on 174Å[1], is designed for observation of Fe IX/X lines formed at temperatures between 5×10^5K and 1.5×10^6K.

Under equilibrium conditions, only those two iron ions will emit strongly enough to trigger the TRACE detector at a rate above the background emission. Of course, other ions do decay with lines in this wavelength band too, particularly Fe XI, but their contribution to the spectrum is suppressed by the instrument passband.

Figure 8.1.1 demonstrates how this suppression works on a synthetic spectrum generated by CHIANTI[2]. The dotted line is the response function, and we see how it favours the four first lines, and the Fe X λ174 line in particular. The synthetic CHIANTI spectrum plotted in figure 8.1.1 was designed to emulate the emission from a coronal plasma with the same parameters as were used in chapter 6.1, which is to say the ionization equilibria of Mazzotta et al. (1998) and abundances of Fludra and Schmelz (1999). An active region differential emission measure (DEM) based on

---

[1] The "171" misnomer is rooted in a historical match with the λ171-band in SoHO's Extreme–Ultraviolet Imaging Telescope (EIT).

[2] Dere et al. (1997), Landi et al. (2006)

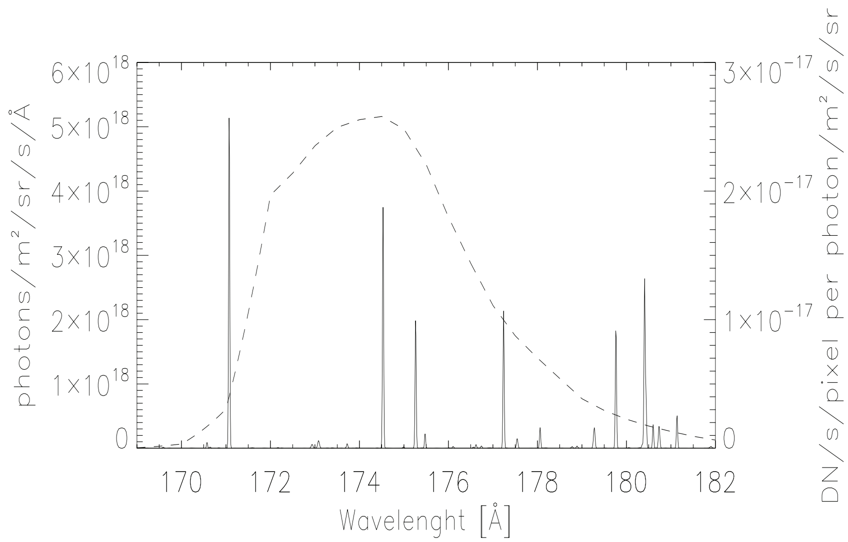

Figure 8.1.1: CHIANTI emission spectrum plotted with the TRACE λ171–band "AO"–mode filter response curve.

Ion	Transition			Wavelength	Intensity
	lower	←	upper	Å	I/I_{tot}
Fe IX	$3p^6\,{}^1S_0$	←	$3p^5 3d^1\,{}^1P_1$	171.073	0.32
Fe X	$3p^5\,{}^2P_{3/2}$	←	$3p^4\,({}^3P)\,3d^1\,{}^2D_{5/2}$	174.534	0.18
Fe X	$3p^5\,{}^2P_{1/2}$	←	$3p^4\,({}^3P)\,3d^1\,{}^2D_{3/2}$	175.266	0.03
Ni XV	$3p^2\,{}^3P_0$	←	$3p^1 3d^1\,{}^3P_1$	176.741	0.01
Fe X	$3p^5\,{}^2P_{3/2}$	←	$3p^4\,({}^3P)\,3d^1\,{}^2P_{3/2}$	177.243	0.11
Fe XI	$3p^4\,{}^1D_2$	←	$3p^3\,({}^2D)\,3d^1\,{}^1F_3$	179.764	0.01
Fe X	$3p^5\,{}^2P^o_{1/2}$	←	$3p^4\,({}^3P)\,3d^1\,{}^2P^e_{1/2}$	180.407	0.02
Fe IX	$3p^4\,{}^3P_2$	←	$3p^3\,({}^4S)\,3d^1\,{}^3D_3$	180.408	0.16
Fe XI	$3p^4\,{}^3P_1$	←	$3p^3\,({}^4S)\,3d^1\,{}^3D_1$	180.600	0.01
Fe XI	$3p^4\,{}^3P_0$	←	$3p^3\,({}^4S)\,3d^1\,{}^3D_1$	181.137	0.01
Fe XI	$3p^4\,{}^3P_1$	←	$3p^3\,({}^4S)\,3d^1\,{}^3D_2$	182.169	0.14
Fe X	$3p^5\,{}^2P_{3/2}$	←	$3p^4\,({}^1D)\,3d^1\,{}^2S_{1/2}$	184.543	0.04

Table 8.1: Lines contributing at least 1% of the total radiation in a synthetic 169–182Å CHIANTI spectrum.

Vernazza and Reeves (1978)'s report was used, and a constraint of constant density. This constrain occurs naturally in both in the solar atmosphere above the TR and in the simulated plasmas.

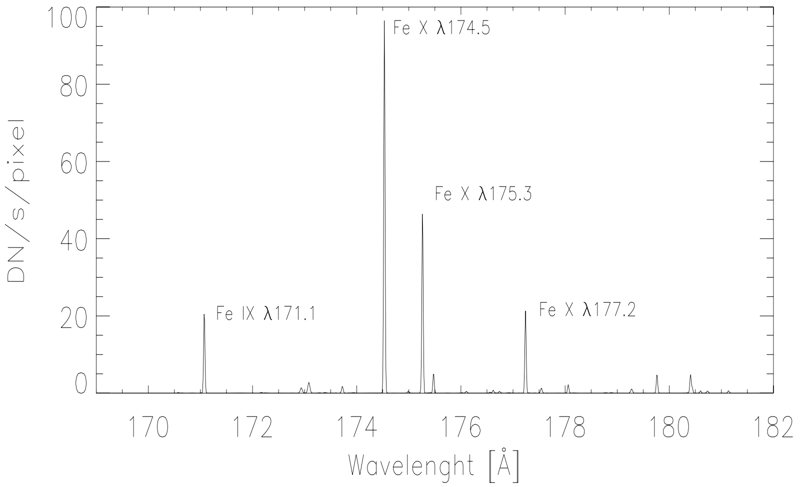

Figure 8.1.2: Product of the CHIANTI 169–182Å spectrum of figure 8.1.1 and the convolution function presented in that same figure.

The twelve strongest lines[3] of the spectrum, with "strongest" defined here as those that each contribute at least 1% of the total emitted energy, are listed in table 8.1. As we see, with the exception of the hot (2.5MK) Ni XV line, all of these are lines from Fe IX-XI, the O VI λ173 lines are not visible. Due to rounding errors and the omitted weak lines, the total intensity does not sum to 100%.

The effects of the bandpass filter transmission is now illustrated by convolving the synthetic CHIANTI spectrum of figure 8.1.1 with the co–plotted response function.

Naturally the lines closer to the band center at 173Å have gained in intensity relative to those farther away. This holds in particular for the Fe X λ174.534 line, which was weak in the original spectrum, but is now is the most prominent one, dwarfing the actual champion Fe IX λ171.079. O VI λ173.080 also grows, even enough to pass above the threshold and appear in the new line list presented as table 8.2. Several lines, like O VI λ172.935 and O VI λ173.095, lie just below the treshold and contribute another 0.5%. The Ni XV line I omitted from the TTRANZ[4] data set (cf. section 6.2) doubled in intensity, but is still weak enough to be ignored at the low temperatures of interest in my numerical analysis.

---

[3] Compare with the corresponding list of lines as they would appear in a quiet region, presented by Harrison and Fludra (1995) as table 3.3 of the CDS Scientific Report.

[4] Supra, chapter 5

As an interim summary we note that the emission in the band is primarily emitted by the iron ions Fe IX/X $\lambda\lambda 171.1, 174.5$, with a slight shift in focus towards the latter line in the data numbers; and that while the radiation from other metals emitting in the band are enhanced relative to iron by the filter, they still contribute negligibly to the total count rate under equilibrium conditions.

Ion	Transition			Wavelength	Intensity
	lower	←	upper	Å	I/I_{tot}
Fe IX	$3p^5 3d^1\ {}^1P_1$	←	$3p^6\ {}^1S_0$	171.073	0.15
O VI	$2p^1\ {}^2P_{3/2}$	←	$3d^1\ {}^2D_{5/2}$	173.080	0.01
Fe X	$3p^5\ {}^2P_{3/2}$	←	$3p^4\ ({}^3P)\ 3d^1\ {}^2D_{5/2}$	174.534	0.53
Fe X	$3p^5\ {}^2P_{1/2}$	←	$3p^4\ ({}^3P)\ 3d^1\ {}^2D_{3/2}$	175.266	0.08
Fe X	$3p^5\ {}^2P_{3/2}$	←	$3p^4\ ({}^3P)\ 3d^1\ {}^2P_{1/2}$	175.444	0.02
Ni XV	$3p^2\ {}^3P_0$	←	$3p^1 3d^1\ {}^3P_1$	176.741	0.02
Fe X	$3p^5\ {}^2P_{3/2}$	←	$3p^4\ ({}^3P)\ 3d^1\ {}^2P_{3/2}$	177.243	0.12
Fe IX	$3p^4\ {}^3P_2$	←	$3p^3\ ({}^4S)\ 3d^1\ {}^3D_3$	180.408	0.03

Table 8.2: Lines contributing at least 1% of the TRACE λ171–band data counts as predicted from a synthetic CHIANTI 169–182Å spectrum convolved by the TRACE λ171–band passband.

8.2 Filter Effects on a TTRANZ Spectrum

Spectra can also be computed based on the plasma defined by the numerical advection program TTRANZ, described in chapter 7. As a finite–difference engine, it defines the plasma at discrete height intervals, and each of these produce different spectra dependent on the temperature at that height. This allows us a tomographic view of the atmosphere, as well as the integrated column spectra of CHIANTI.

My intention in this section is to ascertain how closely the count rate on the detector can follow the emission in the band when the temperature in an isobaric plasma changes.

In figure 8.2.1 I present, for illustrative purposes, two sample spectra from a steady state plasma. They represent the plasma emission at the temperatures of maximum formation of Fe IX (6.4×10^5K) and Fe X (1.0×10^5K), respectively.

The next pair of figures, 8.2.2, contain the same spectra after convolution with the TRACE λ171–band response function. These reflect the situation of the previous section; that in both regions Fe IX is the source of most of the emission, but after the convolution focus is shifted towards Fe X.

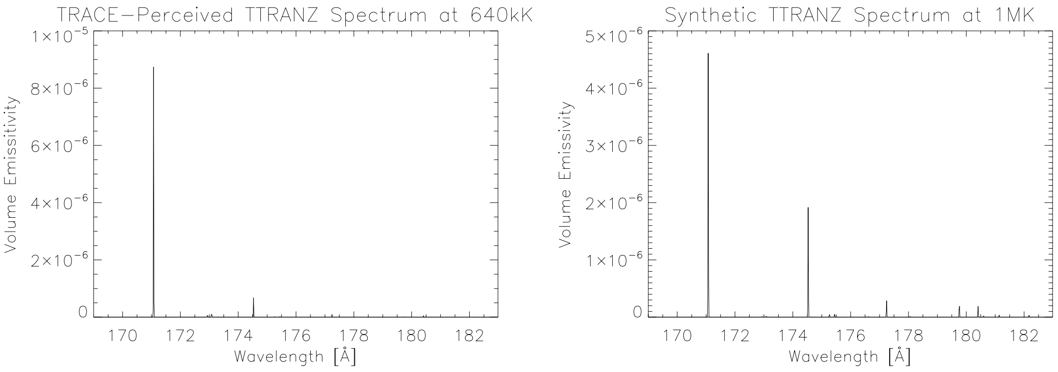

Figure 8.2.1: Synthetic TTRANZ spectra produced at $T_e = 6.4 \times 10^5$K (left) and $T_e = 1.0 \times 10^6$K (right) in a steady state plasma.

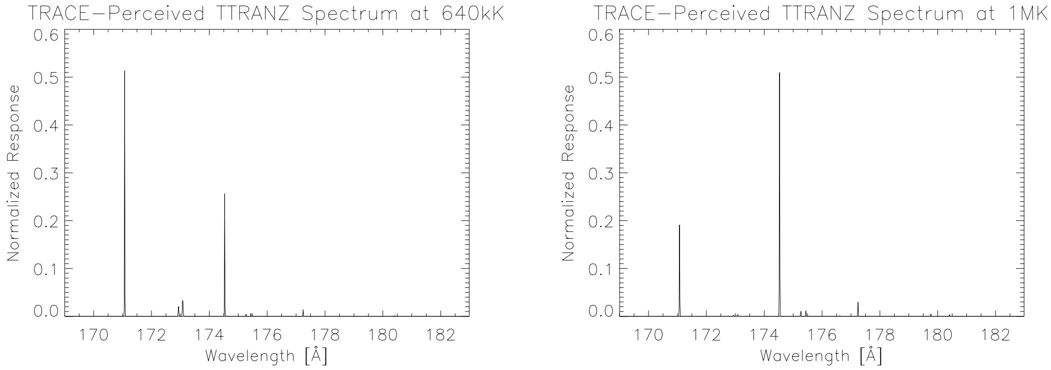

Figure 8.2.2: Synthetic TTRANZ spectra produced at $T_e = 6.4 \times 10^5$K (left) and $T_e = 1.0 \times 10^6$K (right) in a steady state plasma after convolution with the TRACE λ171–band passband.

They also indicate that the convolution preserves the original spectrum, in the sense that both the radiation intensity and the detector data numbers are due to the Fe IX/X ions. To be specific, a conjecture granted by the plot pairs is a linear relation between intensity and data numbers that holds for a wide range of temperatures:

$$I(\mathrm{Fe\,IX}, T_e) + I(\mathrm{Fe\,X}, T_e) \quad \approx \quad \alpha \times \mathrm{DN}, \tag{8.1}$$

with α a constant.

The effect of the convolution at different plasma temperatures is illustrated in figure 8.2.3. This plot shows the integrated volume intensity in the band based on the synthetic spectrum derived at the indicated temperature with "+" symbols. Coplotted with "×" marks is the totalled

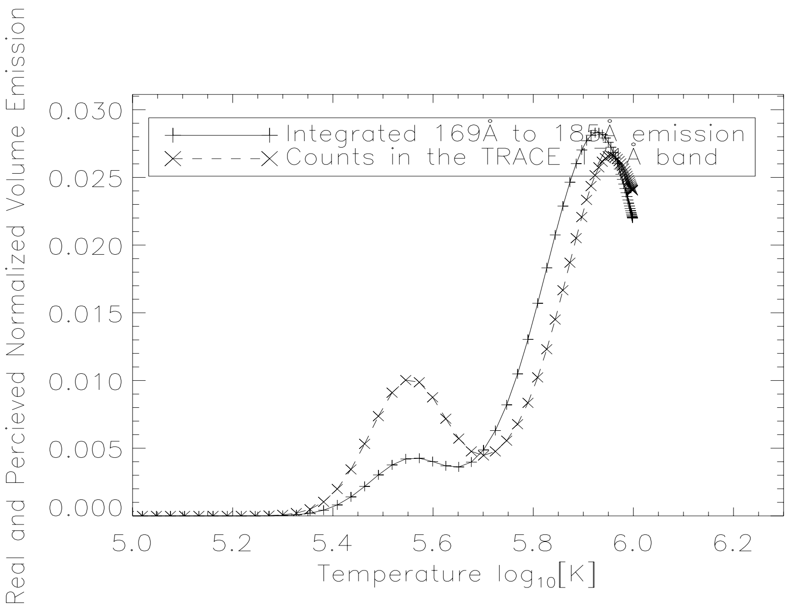

Figure 8.2.3: Integrated TRACE λ171–band intensity from an isobaric equilibrium plasma, compared with the detector response.

data numbers, ie. the integrated emission spectrum after convolution with the passband. In other words, the first graph represents the idealized volume intensity emitted by a plasma cloud at that temperature, while the second graph indicates how many counts the TRACE CCD would register from the same cloud. The graphs have been normalized so that they fit in the same window.

The plot affirms the conjecture, and indicates a validity interval of at least $5 \times 10^5\text{K} < T_e < 1 \times 10^6)$K. For coronal plasmas above 5×10^5K, the count rate from a given region will follow the photon emission in that region well over the whole design temperature range.

This essentially confirms what we expected, that the TRACE λ171–band is well designed for measurement of radiation from coronal Fe IX/X ions.

8.3 Filter Behaviour During Dynamic Conditions

The instrument is clearly presenting steady state plasma emission faithfully, but what about a scenario where the plasma is in a dynamic state — like the rapidly heated loop simulation of section 7.6.1? I now repeat the analysis done in section 8.2, but on the dynamic plasma brought about by 500 seconds of very strong heating.

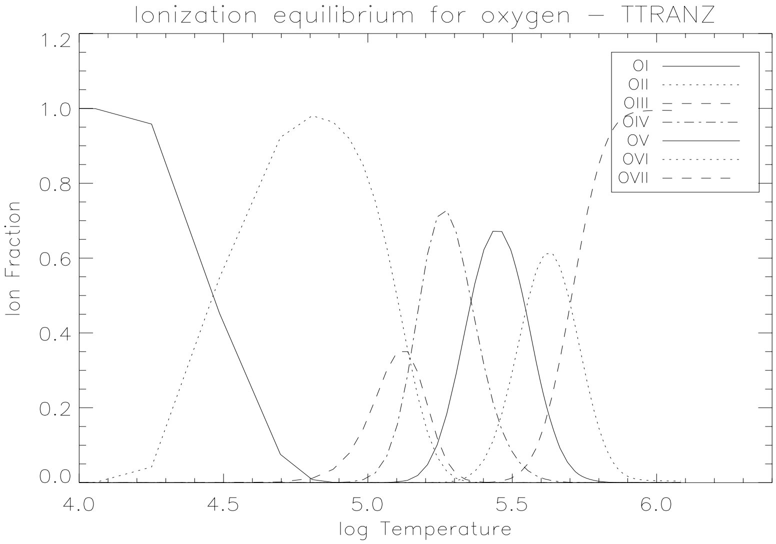

Figure 8.3.1: Oxygen population distribution in a rapidly heated plasma.

The heating process itself is described in section 2.4.4, followed by a detailed description of this dynamic plasma in section 7.6.1.

The oxygen population distribution of figure 8.3.1 illustrates how different the situation is. Not only is O VI present in three times the usual amount, 60% rather than 20% of all oxygen, its temperature of maximum formation is also shifted 1.5×10^5K towards the temperature region of Fe IX. Since the formation temperature of the latter ion is also shifted by this amount, the intensity near $T_e = 6 \times 10^5$K is now due to a blend of the O VI and Fe IX intensity, rather than the single ferrum ion (all the temperatures given are for electrons) emitting at these temperatures in the steady state plasma.

This is reflected in the left spectrum of figure 8.3.2, meant as a counterpart of 7.2.1. The electron temperatures are still at 640×10^3K and 1.0×10^6K, which under steady state conditions are the those of maximum formations for Fe IX/X. But in this instance each of the three O VI lines make strong appearances next to the one iron line. Furthermore, because they are located closer to the peak of the response function, they boosted by the filter even beyond the exceptionally high level they really are at. The combined heights of the three O VI λ173 lines in the left panel of figure 8.3.3 is larger than the combined heights of the iron lines, about two thirds of the counts are triggered by oxygen emission — the instrument is looking at *some* oxygen, but we would think it is looking at a lot of iron.

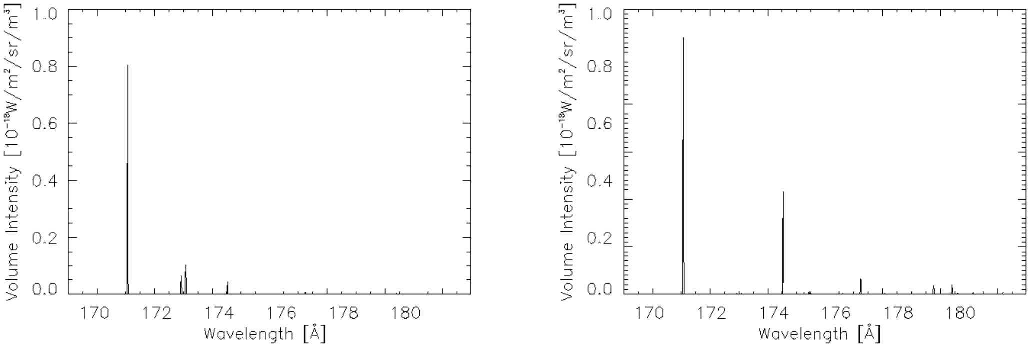

Figure 8.3.2: Synthetic TTRANZ spectra produced at $T_e = 6.4 \times 10^5$K (left) and $T_e = 1.0 \times 10^6$K (right) in a dynamic plasma.

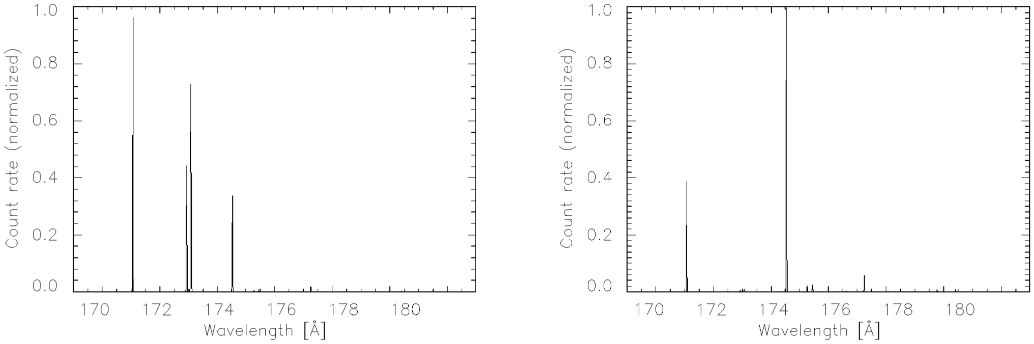

Figure 8.3.3: Synthetic TTRANZ spectra produced at $T_e = 6.4 \times 10^5$K (left) and $T_e = 1.0 \times 10^6$K (right) in a dynamic plasma after convolution with the TRACE λ171–band passband.

At the higher temperature, the right spectra displayed in figures 8.3.2 and 3 behave more like steady state plasmas, the disturbance does apparently not extend this far up in the corona of the simulated loop.

In this situation the count rate cannot be said to accurately represent the emission in the band, it overcounts the low temperature emission from the TR due to the position of the O VI lines in the passband. Compare the integrated emission and count rates for this situation (figure 8.3.4) with the steady state situation of figure 7.2.2. In the former graph the change in count rate with increasing temperature is virtually the same as the change in energy emission, at least above 5×10^5K. During the dynamic event, the detector sees twice the actual intensity at that temperature, but only 60% of it at 8×10^5K.

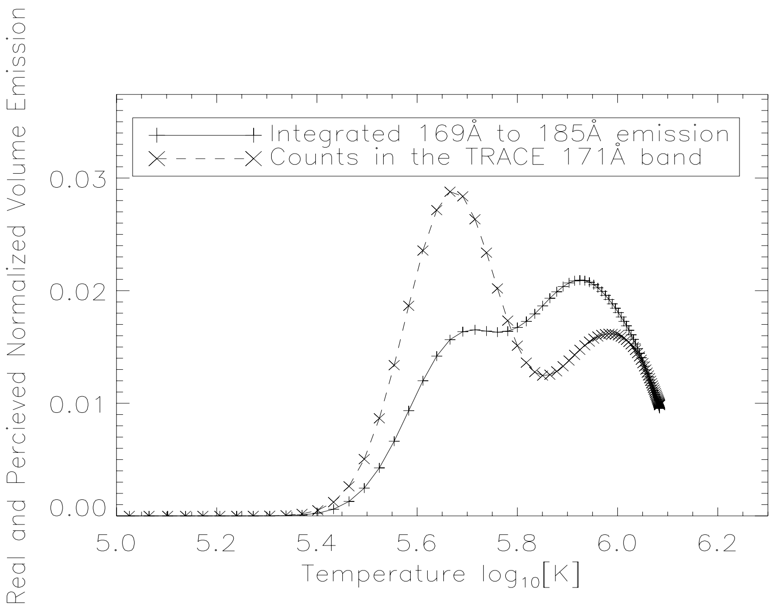

Figure 8.3.4: Integrated TRACE λ171–band intensity from an isobaric, dynamic, plasma, compared with the detector response.

8.4 Discussion

These results indicate that while the λ171 band is doing an excellent job of observing Fe IX/X emission from coronal features such as coronal loops under steady state conditions, it can misrepresent the presence of those ions by a considerable fraction when the population distributions of ferrum and oxygen ions are forced to diverge through a rapid change in the heat input, shock front or similar transient events.

This inflation in count rate lasts as long as it takes for the atoms to thermalize and settle down. This should generally take a few minutes, in the specific case discussed here the strongest effect lasted about 100 seconds.

Chapter 9

Summary and Conclusion

The objective of the present study was the analysis of a transient emission event observed in AR8558, on June 4 1999.

Five spectral windows with six emission lines (N V λ1238, N V λ1242, O V λ629, Mg X λ624, Si II λ1251 and Fe XII λ1242) was transmitted of the 28 second cadence observation, of which particularly N V λ1238 and O V λ629 yielded good results.

The spectral data was supported by EUV images captured by TRACE in the λ171 and λ1550 bands. Despite an unfortunate loss of telemetry for 30 minutes immediately prior to the event, these provided information about the spatial development of the event, at a cadence of 40 seconds.

These observations describe an initially quite cool loop ($1 - 2 \times 10^5$K), of $\lesssim$ 25Mm length. It was not found to be inclined relative to the vertical, and it showed no morphological development over the two–hour observation period. These traits makes it practically invisible to TRACE except during the event, but the intensities measured by SUMER are above the background during the two hours.

The event itself had a very abrupt onset, with the emission in all bands growing to at least twice their background level over a mere two minutes. The TRACE images further reveal that this sudden brightening is global, the whole loop is affected at the same time.

This initial brightening tapers off into a plateau phase lasting some five minutes, and this first stage is followed by two strong bursts of radiation, each lasting about two minutes. All the bands develop in phase except for the final burst, for which a maximum phase delay (C IV to O V) of two minutes is seen. Notwithstanding this late decoherence, all the lines return to their background levels simulatenously; ending the event just as abruptly as it started.

The quiet–loop data was used to construct simulations for the TTRANZ advection engine, with the loop temperature defined by a foot–focused heating model. Transient behaviour similar to that described above was found to occur when the energy input was suddenly and symmetrically increased in the loop for about 500 seconds.

The numerical analysis reveals that the loop is subject to three processes, each responsible for the three stages; ie. the initial emission plateau and subsequent peaks. All owe their effect to the strong dependence of radiation on density.

When the heating is amplified, the temperature in the low–heat capacity coronal section of the loop grows rapidly, while the density jumps and then flattens out. This causes a corresponding jump and plateau in intensity.

High temperatures and strong gradients make thermal conduction efficient, and the temperature is capped at about $\sim 10^6$K as a conduction front starts to move downwards. The strong energy transfer into the chromosphere causes evaporation, and a strong (subsonic) pressure front is sent upwards. Behind this front the density quickly grows by a factor ~ 1.5, corresponding to a doubled radiative loss rate. This strong emission is cut short when the heating is attenuated back to its background level, giving rise to an emission peak.

When the heating is attenuated the temperature quickly drops, but the density responds very slowly. This creates a favourable environment for recombination into the emitting ions, producing the second emission burst. Because this happens in different heights depending on the ion, the phases become incoherent at this point.

An important tangent to the study of the loop was a review of the available schemes and coefficients defining atomic excitation and ionization rates, as well as the element abundances found in the corona and the radiative energy loss as a function of temperature and density. In the plasma regime relevant to the present work, the literature seems to be in agreement, and a "best known" data set was relatively easy to single out.

Finally a short exploration of the behaviour of the TRACE $\lambda 171$–band response function on synthetic spectra produced from dynamic (non–equilibrium) TTRANZ plasmas was made. This revealed two caveats in the use of this band — the well–known impact of the O VI $\lambda 173$ line at TR temperatures, and a strong bias caused by overpopulation of this ion at coronal temperatures.

Appendix A

The Electron Velocity Distribution

Equilibrium Conditions

We assume, more or less by default, that the electrons in a gas follow the Maxwell-Boltzmann velocity distribution,

$$f(v) \quad = \quad \left(\frac{m_e}{2k_BT_e}\right)^{3/2} \exp\left(-\frac{m_ev^2}{2k_BT_e}\right) \tag{A.1}$$

which is a gaussian function with the width determined by the temperature, because when they do we can apply a host of simplifying approximations. The solar atmosphere can often be a quite dynamic environment, however, and it is thus important to have a handle on just when this assumption actually is correct.

Three conditions have to be met: The velocities must be non-relativistic, the plasma must be of sufficiently low density and also change at low enough rate for it to *thermalize*.

A particle has a most probable velocity v_{mp} given by the equation

$$v_{\mathrm{mp}} = \sqrt{(2k_BT_e)/m}; \tag{A.2}$$

about $0.13c$ for an electron at $T_e = 10^6$, a high temperature for the plasmas discussed in this thesis. This is comfortably below relativistic velocity.

The plasma densities are in the range of $10^{15} - 10^{18}$ m^{-3}, which is more than low enough to meet this requirement.

Thermalization is the process where the particles collide with each other so frequently that the velocities get normally distributed about a mean. The time this takes is called the “electron self collision time”, and is discussed by Spitzer (1962) which gives the value

$$t_c = 0.266\frac{T_e^{3/2}}{n_e \log\Lambda} \qquad \text{[s]} \tag{A.3}$$

with

$$\Lambda = \frac{3}{2\overline{Z}^2}\left(\frac{(k_B T_e)^3}{\pi e^6 n_e}\right)^{1/2}. \tag{A.4}$$

He tabulates values for $\log\Lambda$, for a $n_e = 10^{16}\mathrm{m}^{-3}, k_B T_e = 86\mathrm{eV}$ plasma it is about 18.2, which gives the time $t_c = 1.47\mu\mathrm{s}$. That compares very well with the change rate in our plasma, $\Delta T/\Delta t < 100\mathrm{K/s}$ in most cases; and velocities that rarely exceed 100km/s. It certainly looks like we are justified in using this distribution exclusively in our work. There is at least one exception, however, that is important in the TR.

Special Considerations in the TR

Using numerical analysis of the velocity distribution in the transition region, Shoub (1983) concluded that under certain conditions "the distribution function forms an anisotropic, high–velocity tail in the lower temperature regions due to the diffusion of fast electrons antiparallel to the temperature gradient."

This effect should be observable for plasma regions with

$$\lambda \left.\frac{\mathrm{d}\ln(T)}{\mathrm{d}z}\right|_{\max} \gtrsim 10^{-3}, \tag{A.5}$$

where

$$\lambda = \frac{(k_B T_e)^2}{\pi e^4 n_\mathrm{e} \ln(\Lambda)} \tag{A.6}$$

is the mean free path of an electron in a fully ionized hydrogen plasma. Qualitatively this means that we have be careful about situations where the mean free path of the electrons is large compared to the temperature gradient scale lengths.

Appendix B

The Voronov Ionization Scheme

A more simple formalism for computing collisional ionization rates than the one we use in TTRANZ, devised by Arnaud and Rothenflug (1985), is discussed by Mazzotta et al. (1998): the scheme of Voronov (1997). This scheme is simpler in the sense that it uses only one set of coefficients for each ion:

$$\langle \sigma v \rangle \quad = \quad A \frac{1 + P\sqrt{U}}{X + U} U^K \mathrm{e}^{-U} \qquad [\mathrm{cm}^3/\mathrm{s}], \tag{B.1}$$

where $U = dE/k_B T_e$. $\mathrm{d}E$ is the ionization energy in eV, T_e the electron temperature, A, X and K are experimentally fitted parameters, and $P \in \{0, 1\}$ is used to improve the fit of “certain ions near treshold”.

I implemented the scheme in TTRANZ in an attempt to reconcile the simulated iron ionization equilibria with the empirical ones. The results from a run with a steady state plasma are illustrated in figure B.1, and the results do indeed fit Mazzotta et al.'s distribution better than the results based on Arnaud and Rothenflug formalism, with Fe IX constituting a significant fraction of the species at its peak temperature.

While at first glance this might look like a positive result, the real story is a lot more complicated. The ionization equilibria tabulated by Arnaud and Rothenflug and by Voronov are essentially the same, and computer code implementing either scheme should in principle produce the same results. The code has of course been examined for programming glitches, but there are none, so the source of this discrepancy remains a mystery.

Mazzotta et al. points out that “[The Dublin group] formula is valid as long as we consider the case of ionization equilibrium plasmas.” This, as well as the fact that the two schemes should give the same results, makes a replacement of the ionization scheme a non sequiteur. I therefore kept the original code in TTRANZ.

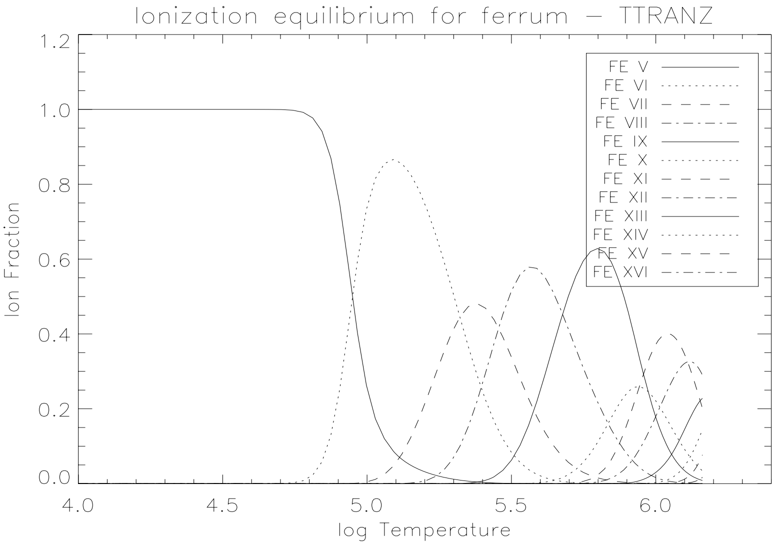

Figure B.1.1: Iron ionization equilibrium calculated using the collisional ionization formalism of Voronov (1997).

Bibliography

Arnaud, M. and Raymond, J. (1992). Iron ionization and recombination rates and ionization equilibrium. *ApJ*, 398:394–406.

Arnaud, M. and Rothenflug, R. (1985). An updated evaluation of recombination and ionization rates. *A&A Supplemental*, 60:425–457.

Aschwanden, M. J. (2004). *Physics of the solar corona: an introduction.* Springer/Praxis, Berlin.

Bentley, R. D. (Ed.) (2001). Solarsoft trace analysis guide. Technical report, Mullard Space Science Lab, University College London.

Burgess, A. (1965). A General Formula for the Estimation of Dielectronic Recombination Co-Efficients in Low-Density Plasmas. *ApJ*, 141:1588–1590.

Burgess, A. and Tully, J. A. (1992). On the Analysis of Collision Strengths and Rate Coefficients. *A&A*, 254:436–453.

Carlsson, M. (1996). IDL routine for SUMER geometric corrections (`sumer_geo.pro`). *Published online (accessed January 2007):* `http://www.astro.uio.no/~matsc/sumer/sumer_help.html#SUMER_GEO`.

Charbonneau, P. (1995). Genetic Algorithms in Astronomy and Astrophysics. *ApJ Supplemental*, 101:309–+.

Clark, R. E. H., Magee, Jr., N. H., Mann, J. B., and Merts, A. L. (1982). Collisional excitation rates of complex atomic ions by electron impact. *ApJ*, 254:412–418.

De Pontieu, B., Berger, T. E., Schrijver, C. J., and Title, A. M. (1999). Dynamics of Transition Region 'Moss' at high time resolution. *Solar Physics*, 190:419–435.

De Pontieu, B., Tarbell, T., and Erdélyi, R. (2003). Correlations on Arcsecond Scales between Chromospheric and Transition Region Emission in Active Regions. *ApJ*, 590:502–518.

Del Zanna, G., Berrington, K. A., and Mason, H. E. (2004). Benchmarking atomic data for astrophysics: Fe X. *A&A*, 422:731–749.

Dere, K. P., Landi, E., Mason, H. E., Monsignori Fossi, B. C., and Young, P. R. (1997). CHIANTI - an atomic database for emission lines. *A&A Supplemental*, 125:149–173.

Dorfi, E. A. and Drury, L. O. (1987). Simple adaptive grids for 1-D initial value problems. *Journal of Computational Physics*, 69:175–195.

Edlén, B. (1943). Die Deutung der Emissionslinien im Spektrum der Sonnenkorona. Mit 6 Abbildungen. *Zeitschrift fur Astrophysik*, 22:30–+.

Fludra, A. and Schmelz, J. T. (1999). The absolute coronal abundances of sulfur, calcium, and iron from Yohkoh-BCS flare spectra. *A&A*, 348:286–294.

Goett, S. J. and Sampson, D. H. (1983). Collision Strengths for Inner-Shell Excitation of Li-like Ions from Levels of the $1s^22s$ and $1s^22p$ Configurations to Levels of the $1s2l2l$' Configurations. *Atomic Data and Nuclear Data Tables*, 29:535–+.

Golub, L., Bookbinder, J., Deluca, E., Karovska, M., Warren, H., Schrijver, C. J., Shine, R., Tarbell, T., Title, A., Wolfson, J., Handy, B., and Kankelborg, C. (1999). A new view of the solar corona from the transition region and coronal explorer (TRACE). *Physics of Plasmas*, 6:2205–2216.

Grevesse, N. and Sauval, A. J. (1998). Standard Solar Composition. *Space Science Reviews*, 85:161–174.

Gu, M. F. (2003a). Dielectronic Recombination Rate Coefficients for H-like through Ne-like Isosequences of Mg, Si, S, Ar, Ca, Fe, and Ni. *ApJ*, 590:1131–1140.

Gu, M. F. (2003b). Radiative Recombination Rate Coefficients for Bare through F-like Isosequences of Mg, Si, S, Ar, Ca, Fe, and Ni. *ApJ*, 589:1085–1088.

Handy, B. N., Acton, L. W., Kankelborg, C. C., Wolfson, C. J., Akin, D. J., Bruner, M. E., Caravalho, R., Catura, R. C., Chevalier, R., Duncan, D. W., Edwards, C. G., Feinstein, C. N., Freeland, S. L., Friedlaender, F. M., Hoffmann, C. H., Hurlburt, N. E., Jurcevich, B. K., Katz, N. L., Kelly, G. A., Lemen, J. R., Levay, M., Lindgren, R. W., Mathur, D. P., Meyer, S. B., Morrison, S. J., Morrison, M. D., Nightingale, R. W., Pope, T. P., Rehse, R. A., Schrijver, C. J., Shine, R. A., Shing, L., Strong, K. T., Tarbell, T. D., Title, A. M., Torgerson, D. D., Golub, L., Bookbinder, J. A., Caldwell, D., Cheimets, P. N., Davis, W. N., Deluca, E. E., McMullen, R. A., Warren, H. P., Amato, D., Fisher, R., Maldonado, H., and Parkinson, C. (1999). The transition region and coronal explorer. *Solar Physics*, 187:229–260.

Handy, B. N., Bruner, M. E., Tarbell, T. D., Title, A. M., Wolfson, C. J., Laforge, M. J., and Oliver, J. J. (1998). UV Observations with the Transition Region and Coronal Explorer. *Solar Physics*, 183:29–43.

Hansteen, V. (1991). *Non-Equilibrium Effects in Solar Transition Region Physics.* PhD thesis, University of Oslo.

Hansteen, V. H. (2005). Lecture notes in space plasma (ast5130). Technical report, University of Oslo.

Harrison, R. A. and Fludra, A. (1995). The CDS for the SOHO Scientific Report. Technical report, Astrophysics Division, Rutherford Appleton Laboratory.

Judge, P. et al. (1998). Hao spectral diagnostic package for emitted radiation. Technical report, HAO.

Landi, E., Del Zanna, G., Young, P. R., Dere, K. P., Mason, H. E., and Landini, M. (2006). CHIANTI-An Atomic Database for Emission Lines. VII. New Data for X-Rays and Other Improvements. *ApJ Supplemental*, 162:261–280.

Landi, E. and Landini, M. (1999). Radiative losses of optically thin coronal plasmas. *A&A*, 347:401–408.

Müller, D. A. N., Hansteen, V. H., and Peter, H. (2003). Dynamics of solar coronal loops. I. Condensation in cool loops and its effect on transition region lines. *A&A*, 411:605–613.

Mazzotta, P., Mazzitelli, G., Colafrancesco, S., and Vittorio, N. (1998). Ionization balance for optically thin plasmas: Rate coefficients for all atoms and ions of the elements H to NI. *A&A Supplemental*, 133:403–409.

Mihalas, D. (1978). *Stellar Atmospheres, 2nd ed.* W. H. Freeman.

Parker, E. N. (1983). Magnetic neutral sheets in evolving fields. I - General theory. II - Formation of the solar corona. *ApJ*, 264:635–647.

Pequignot, D., Petitjean, P., and Boisson, C. (1991). Total and effective radiative recombination coefficients. *A&A*, 251:680–688.

Press, W. H., Teukolsky, S. A., Vetterling, W. T., and Flannery, B. P. (2002). *Numerical Recipes in C++, 2nd ed.* Cambridge University Press.

Priest, E. R., Foley, C. R., Heyvaerts, J., Arber, T. D., Mackay, D., Culhane, J. L., and Acton, L. W. (2000). A Method to Determine the Heating Mechanisms of the Solar Corona. *ApJ*, 539:1002–1022.

Ralchenko, Y., Kramida, A., and Reader, J. (2005). Nist atomic spectra database. Online, http://physics.nist.gov/PhysRefData/ASD/index.html. Standard Reference Database #78.

Reale, F., Peres, G., Serio, S., Betta, R. M., DeLuca, E. E., and Golub, L. (2000a). A Brightening Coronal Loop Observed by TRACE. II. Loop Modeling and Constraints on Heating. *ApJ*, 535:423–437.

Reale, F., Peres, G., Serio, S., DeLuca, E. E., and Golub, L. (2000b). A Brightening Coronal Loop Observed by TRACE. I. Morphology and Evolution. *ApJ*, 535:412–422.

Reisenfeld, D. B., Raymond, J. C., Young, A. R., and Kohl, J. L. (1992). On the density and field sensitivities of dielectronic recombination. *ApJ Letters*, 389:L37–L40.

Rosner, R., Tucker, W. H., and Vaiana, G. S. (1978). Dynamics of the quiescent solar corona. *ApJ*, 220:643–645.

Rybak, J., Curdt, W., Kučera, A., Schüehle, U., and Wöehl, H. (1999). Chromospheric And Transition Region Dynamics - Reasons and Consequences of the Short Period Instrumental Periodicities of SOHO/SUMER. In Vial, J.-C. and Kaldeich-Schü, B., editors, *ESA SP-446: 8th SOHO Workshop: Plasma Dynamics and Diagnostics in the Solar Transition Region and Corona*, pages 579–+.

Salzman, D. (1998). *Atomic Physics in Hot Plasmas.* Oxford University Press.

Serio, S., Peres, G., Vaiana, G. S., Golub, L., and Rosner, R. (1981). Closed coronal structures. II - Generalized hydrostatic model. *ApJ*, 243:288–300.

Shoub, E. C. (1983). Invalidity of local thermodynamic equilibrium for electrons in the solar transition region. I - Fokker-Planck results. *ApJ*, 266:339–369.

Shull, J. M. and van Steenberg, M. (1982). The ionization equilibrium of astrophysically abundant elements. *ApJ Supplemental*, 48:95–107.

Spadaro, D. and Lanza, A. F. (2003). Simulations of transiently heated solar coronal loops. *Memorie della Societa Astronomica Italiana*, 74:687–+.

Spitzer, L. (1962). *Physics of Fully Ionized Gases, 2nd ed.* John Wiley & Sons.

Starck, J.-L., Murtagh, F., and Bijaoui, A. (1998). *Image Processing and Data Analysis.* Cambridge University Press.

Storey, P. J., Zeippen, C. J., and Le Dourneuf, M. (2002). Atomic data from the IRON Project. LI. Electron impact excitation of Fe IX. *A&A*, 394:753–762.

Teriaca, L., Wilhelm, K., and Schüle, U. (2003). Reduction and analysis of sumer data. Technical report, Max-Planck-Institut für Aeronomie (MPAe).

van Leer, B. (1977). Towards the ultimate conservative difference scheme. 4. a new approach to numerical convection. *Journal of Computational Physics*, 23:276–299.

Vernazza, J. E. and Reeves, E. M. (1978). Extreme ultraviolet composite spectra of representative solar features. *ApJ Supplemental*, 37:485–513.

Verner, D. A. and Ferland, G. J. (1996). Atomic Data for Astrophysics. I. Radiative Recombination Rates for H-like, He-like, Li-like, and Na-like Ions over a Broad Range of Temperature. *ApJ Supplemental*, 103:467–+.

Voronov, G. S. (1997). A Practical Fit Formula for Ionization Rate Coefficients of Atoms and Ions by Electron Impact: Z = 1-28. *Atomic Data and Nuclear Data Tables*, 65:1–+.

Warren, H. P., Winebarger, A. R., and Mariska, J. T. (2003). Evolving Active Region Loops Observed with the Transition Region and Coronal explorer. II. Time-dependent Hydrodynamic Simulations. *ApJ*, 593:1174–1186.

Watko, J. A. and Klimchuk, J. A. (2000). Width Variations along Coronal Loops Observed by TRACE. *Solar Physics*, 193:77–92.

Wikstøl, Ø., Hansteen, V. H., Carlsson, M., and Judge, P. G. (2000). Chromospheric and Transition Region Internetwork Oscillations: A Signature of Upward-propagating Waves. *ApJ*, 531:1150–1160.

Wilhelm, K. (2000). Absolute Radiometric Calibration and Corrections. Technical report, Max-Planck-Institut für Aeronomie (MPAe).

Wilhelm, K., Curdt, W., Marsch, E., Schuhle, U., Lemaire, P., Gabriel, A., Vial, J.-C., Grewing, M., Huber, M. C. E., Jordan, S. D., Poland, A. I., Thomas, R. J., Kuhne, M., Timothy, J. G., Hassler, D. M., and Siegmund, O. H. W. (1995). SUMER - Solar Ultraviolet Measurements of Emitted Radiation. *Solar Physics*, 162:189–231.

Yurimoto, H. and Kuramoto, K. (2004). Molecular cloud origin for the oxygen isotope heterogeneity in the solar system. *Science*, 305:1763–1766.